NUMERICAL STUDY OF THE LATERAL RESPONSE OF PRECAST COMPOSITE WALL SYSTEMS

AMIR HOSSEIN HAJI MIRARAB

A THESIS SUBMITTED TO THE FACULTY OF GRADUATE STUDIES
IN PARTIAL FULFILLMENT OF THE REQUIREMENTS FOR THE DEGREE OF
MASTER OF APPLIED SCIENCE

GRADUATE PROGRAM IN CIVIL ENGINEERING
YORK UNIVERSITY
TORONTO, ONTARIO

APRIL 2019

ABSTRACT

A novel, light gauge steel stud-thin shell precast concrete panel system was developed to serve as a vertical wall panel element to resist vertical and out-of-plane horizontal loads. The behavior and capacity of this system to sustain in-plane lateral loads arising from wind and earthquake actions are currently not understood. The focus of this research is to assess the performance of such a system when subjected to lateral loading. Two-dimensional monotonic and reverse cyclic nonlinear finite element analyses of the Thin Shell Precast (TSP) panel was conducted using Program VecTor2. The analyses evaluated the effect of various components of the system including the type and size of the internal reinforcing bars and the influence of the exterior light-gauge steel framing. The modelling also shed light on the effect of reinforcement bonding and the difference in response between squat and slender wall systems. Through the nonlinear modelling, lateral load-displacement (drift) responses were generated for monotonic and reverse cyclic motions, in addition to quantifying the yield and ultimate loads and corresponding displacements (drifts). Preliminary analyses were used to modify the design of the Thin Shell Panel to achieve an improved lateral response.

ACKNOWLEDGEMENTS

I would like to acknowledge and thank the following who have supported me, not only during this thesis project but also through my Master's degree. First, I would like to express my gratitude to my supervisor Dr. Dan Palermo for his unwavering support, guidance and insight throughout this research project. I would like to thank the committee members, especially for their comments and suggestions to improve my thesis. I would like to thank Burnco Manufacturing for sharing this project with us and collaborating on the research. I also wish to thank my friends and colleagues, namely Adrien Sparling, Negar Daemi, Parin Izadi and Parnian Izadi. Last but not least, an extraordinary thanks to my spouse Dr. Mehrsa Dibadin for her support, encouragement and belief in my abilities.

TABLE OF CONTENTS

LIST OF TABLES

LIST OF FIGURES

NOMENCLATURE

Symbols

c_t	Compression softening coefficient
$[B]$	Element strain-displacement matrix
d_b	Diameter of reinforcing bar
$[D]$	Composite material stiffness matrix
$[D_c]$	Concrete material stiffness matrix relative to x, y-axes
$[D_s]$	Reinforcement material stiffness matrix relative to x, y-axes
D_b	Reinforcement diameter (mm)
C_d	Compression softening, strain softening factor
C_s	Compression softening, shear slip factor
c_t	Tension stiffening coefficient
E_c	Initial tangent stiffness of concrete
$\bar{E}_{c1}$	Secant modulus of concrete in the principal tensile direction
$\bar{E}_{c2}$	Secant modulus of concrete in the principal compressive direction
E_s	Initial tangent stiffness of reinforcement
$\bar{E}_s$	Secant modulus of reinforcement
E_{st}	Unloading and reloading stiffness due to the frictional bond behavior of fibres
f_c'	Concrete cylinder uniaxial compressive strength
f_{c1}	Average net concrete tensile stress
f_{c1}^a	Post-cracking tension stiffening

f_{c2}	Average net concrete compressive stress
f_{cx}	Average concrete axial stress in the x-direction
f_{cy}	Average concrete axial stress in the y-direction
f_p	Peak concrete compressive stress
f_{sx}	Average stress of reinforcement parallel to the x-direction
f_{sy}	Average stress of reinforcement parallel to the y-direction
f_{scrx}	Local stress at a crack of reinforcement parallel to the x-direction
f_{scry}	Local stress at a crack of reinforcement parallel to the y-direction
f_t'	Concrete cracking strength
F_u	Ultimate strength (MPa)
F_y	Yield strength (MPa)
$\bar{G}_c$	Secant shear modulus of concrete
G_f	Fracture energy parameter
$[k]$	Element stiffness matrix
$[K_c]$	Element stiffness matrix contribution from concrete
$[K_s]$	Element stiffness matrix contribution from reinforcement
$[K]$	Structure stiffness matrix
β_d	Compression softening reduction factor
γ_{cxy}	Average net concrete shear strain
γ_{cx}^p	Plastic shear strain
γ_{xy}	Shear strain
γ_{xy}^s	Average shear strain due to shear slip

γ_{cmx}	Maximum shear strain parallel to the x-direction
ε_{c2}	Compression strain in concrete
ε_{ch}	Characteristic strain for concrete in tension
ε_{cr}	Concrete cracking strain
ε_{cx}	Average net concrete axial strain, in the x-direction
ε_{cy}	Average net concrete axial strain, in the y-direction
ε_c^0	Elastic strain offsets in concrete
ε_s^0	Elastic strain offsets in reinforcements
ε_c^p	Plastic strain offsets in concrete
ε_{cx}^p	Plastic strain for given load step on x-direction
ε_{cy}^p	Plastic strain for a given load step on y-direction
ε_s^p	Plastic strain offsets in reinforcements
ε_{cmx}	Maximum concrete compressive strain
ε_0	Concrete compressive strain corresponding to f_c'
ε_p	Concrete compressive strain corresponding to f_p
ε_{sh}	Reinforcement strain at onset of strain hardening
ε_x	Compatible strain in the x-direction
ε_x^s	Average axial strain in the x-direction, due to shear slip
ε_y	Compatible strain in the y-direction
ε_y^s	Average axial strain in the y-direction, due to shear slip
ε_u	Ultimate strain (me)
θ	Orientation of principal net concrete strain field

θ_{nx}	Angle between the normal of a crack and x-direction
θ_{ny}	Angle between the normal of a crack and y-direction
θ_{ε}	Average principal tensile strain
θ_{σ}	Average principal tensile stress
ϑ_{cxy}	Average concrete shear stress
ρ_x	Reinforcement ratio in the x-direction
ρ_{sx}	Reinforcement ratio in the x-direction
ρ_{sy}	Reinforcement ratio in the y-direction
ρ_y	Reinforcement ratio in the y-direction
$[\sigma]$	Applied axial stress matrix
σ_x	Applied axial stress in the x-direction
σ_y	Applied axial stress in the y-direction
τ_{xy}	Applied shear stress

Chapter 1 Introduction

Concrete walls are vertical structural members that are used to resist in-plane and out-of-plane lateral loading, in addition to gravity loading. Based on their function, reinforced concrete walls can be classified as retaining walls, bearing walls, or shear walls. In this thesis, the focus is on shear wall panels. The main function of shear walls is to resist in-plane lateral loads due to wind and earthquake. Shear walls typically have high in-plane lateral strength and stiffness (along the length plane) and weak lateral strength and low stiffness in their out-of-plane (loaded perpendicular to the long plane). Shear walls, based on their height-to-length ratio (aspect ratio) are divided into two classes: flexural or slender, and squat or short. For the height-to-length ratio of greater than 2, the shear wall is considered flexural (slender), resisting in-plane lateral loads by flexural action. For height-to-length ratio not exceeding 2, the wall is deemed to be squat (short). The loading transfer mechanism and failure mode are different for these two types of walls. Slender walls are commonly incorporated in medium-to high-rise buildings, whereas squat walls find applications in low- to medium-rise structures.

A novel lightweight precast wall system known as the Thin Shell Panel (TSP) was developed by Nexcon Inc, a subsidiary of Burnco Manufacturing Inc. This new wall system combines external light gauge steel framing partially embedded into a thin concrete shell. The system can be built as either a slender or squat wall system. The focus of this study is

to inform on the in-plane lateral performance of the wall system using nonlinear numerical modelling.

1.1 Background

The precast shear wall panel system is intended to provide design flexibility and versatility for architects and engineers. It can accommodate a variety of external light gauge steel sizes, gauges and spacing with or without insulation. Architectural finishes can also be incorporated with ease (www.nexcon.ca). Figure 1-1 illustrates the various applications of the TSP wall system.

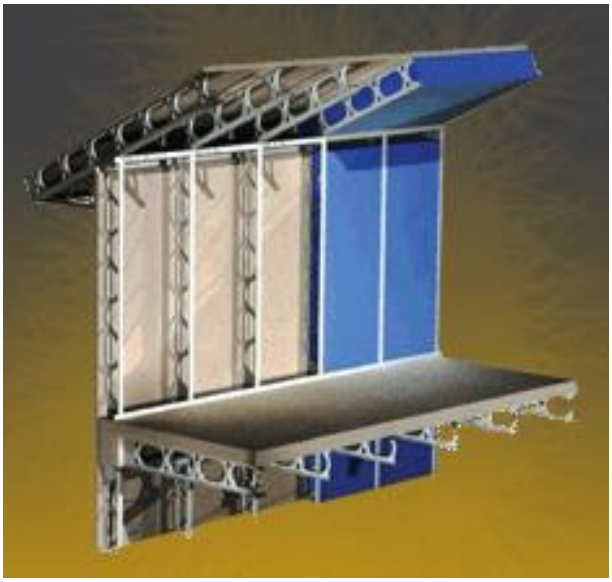

Figure 1-1 Drawing of various implementations of the TSP system ("Products@www.nexcon.ca" 2011)

The Thin Shell Panel (TSP) systems are quick to install and reduces labour time relative to other forms of construction. There is no need for scaffolding given that the panels are

precast and can be tilted up. The panels can be installed as they arrive on site in any weather conditions allowing builders to continue construction without delays.

Furthermore, the TSP panels are ideally suited for exterior cladding and serve as structural load-bearing exterior and interior walls, floors, roofs and foundation walls. The open web configuration of the external light gauge steel provides free passage for electrical and mechanical systems. Thus, the system eliminates the need for most bulkheads. The open web also helps to improve thermal efficiency and acoustic attenuation.

The TSP composite system combines galvanized light-gauge steel with approximately 2" (50 mm) to 3" (75 mm) of concrete. The TSP is lightweight, weighing roughly 35 to 45 pounds per square foot (1.5-1.9 kg/m^2), which is one-third of a conventional precast concrete panel that is currently used for load-bearing and floor system applications.

The TSP contains a substantial amount of recycled steel, and the concrete shell can be constructed with recycled concrete materials. The relatively thin concrete shell results in a reduction in Carbon Dioxide ($CO2$) emissions. Moreover, due to the lightweight of the TSP, transportation, handling and labor costs are limited. The TSP is available in precast or cast-in-place forms and can be cut to any desirable length. The tilt-up technique is the most typical method to install the panels on site.

Although this system meets building code requirements for certain applications, such as the tilt-up walls, and flooring systems, the in-panel lateral load capacity has yet to be quantified. Currently, in the wall configuration, the panels are relied upon to resist out-of-plane lateral loads. A secondary structural system (bracing) is required along the wall

panels to withstand in-plane lateral loads. Thus, the system has not been used to act as a shear wall system to date.

1.2 Research Objectives

The focus of this research is to investigate the in-plane lateral performance of the TSP wall system. The primary technical challenge is to determine the contribution of the partially embedded external light gauge steel framing. In addition, the bond characteristics between the internal smooth wire-mesh reinforcement placed within the concrete panel plays a vital role in the lateral strength capacity. These two issues cannot be routinely evaluated using current design standards. To address this, the objective of this research is to establish the lateral performance of the precast composite wall panels as a shear wall system, including lateral strength and displacement capacities. This will be achieved through numerical modelling using advanced two-dimensional nonlinear finite element models.

1.3 Thesis Layout

Chapter 2 contains a literature review of the factors that affect the lateral performance of reinforced concrete shear walls, including the importance of bond strength. Chapter 3 provides detailed and background information on the Thin Shell Panel wall system, including current and future applications. Chapter 4 describes the analytical tool used in this investigation to evaluate the lateral performance of the TSP wall systems. This includes the equilibrium, constitutive and compatibility relationships forming the basis of the finite element routine. Chapter 5 details a number of preliminary analyses of the wall systems to

quantify the influencing parameters on the lateral response. Chapter 6 provides suggestions for the final design of the TSP and detailed numerical analysis considering both monotonic and reverse cyclic loading. Lastly, Chapter 7 contains a number of conclusions based on the results of the analyses.

Chapter 2 Literature Review

The research presented in this thesis focuses on the Nexcon Innovative Lightweight Precast Thin Shell Panel (TSP) System. The system combines patented light gauge steel framing with approximately 50 mm to 75 mm of the concrete overlay to form a composite structural panel. The concrete is reinforced with smooth wire-mesh reinforcement. Given that this study investigates a proprietary system with no existing literature, the literature presented in this chapter presents background information on related design issues to the TSP including smooth and deformed reinforcing bars, size effect, and bond strength. Each of these plays a role in the performance of the wall panel as a lateral force-resisting structural component.

2.1 Smooth and Deformed Reinforcing Bars

The current design of the TSP incorporates smooth internal wire-mesh reinforcement within the thin concrete overlay. Smooth bars were traditionally used as reinforcement to strengthen and reinforce concrete structures (Fabbrocino, Verderame, & Manfredi, 2005). Since the early 1970s, however, the use of deformed bars for reinforcement in concrete structures has become the standard (Fabbrocino et al., 2005). The use of deformed bars in reinforced concrete structures became common due to the poor bonding characteristics of smooth bars relative to deformed bars (Bamonte and Gambarova 2007; Fabbrocino et al. 2004). While smooth bars have found applications in research, they are not typically used

for purposes of reinforcement (Fabbrocino, Verderame, Manfredi, & Cosenza, 2004). In Europe, a significant stock of the existing concrete structures was reinforced with smooth bars (Fabbrocino et al., 2004). As knowledge around seismic activity has increased, and building codes and material standards have been updated, there has been growing concern about how best to upgrade concrete structures reinforced with smooth reinforcing bars (Verderame, Fabbrocino, & Manfredi, 2008b).

A variety of factors influences the strength and the reinforcing potential of different types of bars. Research has highlighted that the strength of deformed bars is greatly affected by the surfaces of these bars (Tilly, 1979). The early research illustrated that deformed bars with ribbings that are 16 mm in diameter provided enhanced strength during axial testing in comparison to smooth bar (Tilly, 1979). In addition, research on 25 mm-diameter bars has shown that the strength of these bars can be greatly improved when they are machined with smooth ribbings that are 6 mm in diameter (Tilly, 1979). It has been suggested that both ribbing and diameter can have an impact on the strength of deformed bars (Tilly, 1979). A reduction in diameter translates to a reduction in surface inclusions and other potential sites for bonding to occur (Tilly, 1979).

Research has further demonstrated that smooth bars in reinforced concrete are more sensitive to high temperatures than deformed bars (International Federation for Structural Concrete, 2000), while the diameter of these two types of bars appears to have no impact on their overall bond strength (H. Park & Kim, 2005). However, in tests to determine the failure loads in beams and one-way slabs, smooth bars appeared to perform better than

deformed bars (Muttoni, A., and Ruiz, 2008) In one of the tests with deformed bars, the beam reached 50 percent of its strength (Muttoni, A., and Ruiz, 2008). Conversely, in another test with smooth reinforcing bars, the beam attained 86 percent of its strength (Muttoni, A., and Ruiz, 2008). It was concluded that as a result of the reduced bond strength with smooth bars, concrete cracking through the inclined strut was reduced (Muttoni, A., and Ruiz, 2008). This increased the strength of the beam (Muttoni, A., and Ruiz, 2008).

Reinforced concrete structures reinforced with either smooth or deformed bars tend to fail in different ways and create different consequences as a result of their failure (Bažant, Li, & Thoma, 1995). Failure as a result of interface slip alone is related to the use of smooth bars in concrete structures (Bažant et al., 1995). Conversely, failures in structures using deformed bars tend to involve cracking in the surrounding concrete (Bažant et al., 1995). Given that the use of smooth bars leads to failures where there is no cracking in the surrounding concrete, they are helpful for understanding interfacial shear behaviour.

2.2 Size Effect

The current design of the TSP incorporates 6 mm-diameter smooth wire-mesh reinforcement. Consideration is being given to increasing the diameter.

When examining the use of smooth and deformed bars in reinforced concrete structures, the size effect is essential to note. Size effect has been shown to have a critical impact on the mechanical behaviour of structures, particularly when their materials have quasi-brittle responses to increasing strain or displacement (P. F. Bamonte & Gambarova, 2007). Figure 2-1 shows the local bond stress-slip law for deformed bars (I), and smooth bars (II) with

respect to improvements suggested by Huang et al. (1996). These improvements contributed to the reformulation of the local bond stress-slip law, taking into to account the size effect (P. F. Bamonte & Gambarova, 2007).

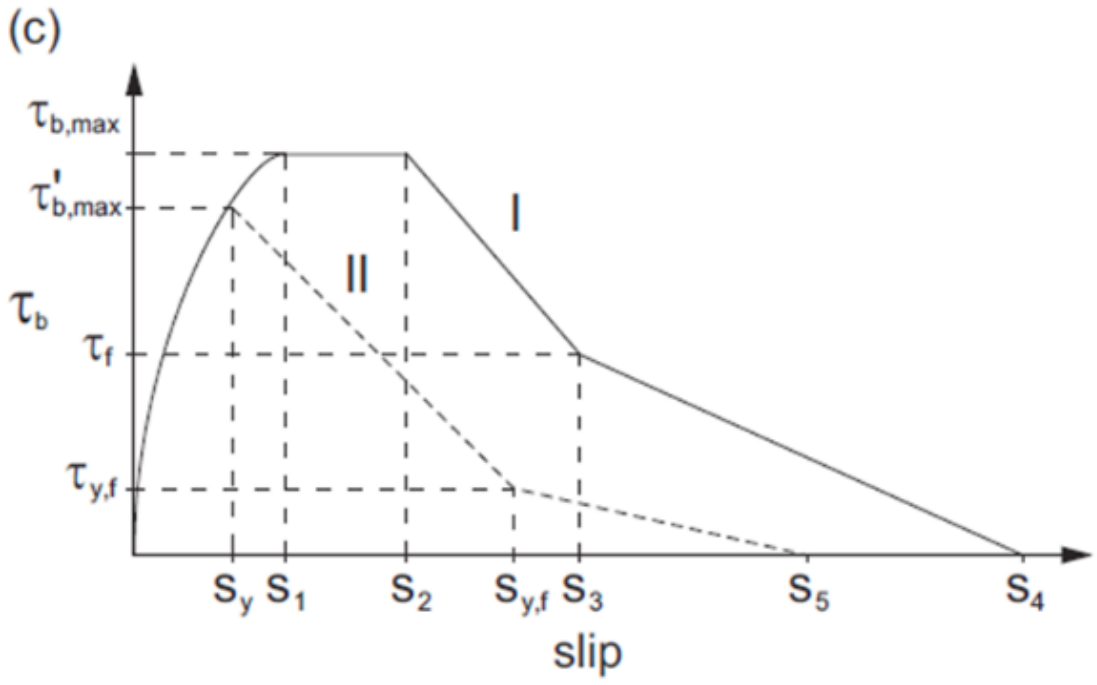

Figure 2-1 Local bond stress-slip law for deformed bars (I + II) (P. F. Bamonte & Gambarova, 2007)

Research on reinforced concrete using both smooth and deformed bars has shown that size effect is an important concept. (P. F. Bamonte & Gambarova, 2007). Generally, for deformed reinforcing bars, size effects are more pronounced (Tilly, 1979). However, other research shows that the type of concrete used can have a meaningful impact on how size effect is produced (P. F. Bamonte & Gambarova, 2007). For both smooth and deformed

bars, size dependency is more pronounced in concrete that is of normal strength (P. F. Bamonte & Gambarova, 2007).

The use of high-performance concrete and aggregates designed to increase strength has a lessening effect on size dependency (P. F. Bamonte & Gambarova, 2007). While the reasons behind this difference are not entirely known, this illustrates that in addition to the type of reinforcing bar used, the type of concrete used in the structure has a vital role on the performance of reinforcing bars (P. F. Bamonte & Gambarova, 2007). Bond behaviour in small-diameter smooth or deformed bars are generally better than larger diameters for a given embedment length due to the ratio between surface and cross-section. Although smooth bars are seldom used in practice today, the size effect when using these bars has been investigated given the debonding along the bar-concrete interface. Also, modelling of structures reinforced with smooth bars provides a pivotal study to other bond problems. Bamonte and Gambarova (2007) investigated the following:

1- The overall behaviour of the anchored bar; and

2- Evaluation of the ultimate capacity under pull-out tests for a smooth bar with no confinement (l/db=10) and deformed bar with confinement (l/db=3 to 5). Where l is the length of the bar and db is the bar diameter.

Confinement has been used for the deformed bars to control cracking, concrete crushing in front of the bar ribs and cover splitting along the bar, aside from the size effect. The research clearly illustrates that size dependency is greater in Normal Strength Concrete (NSC) than High-Performance Concrete (HPC). Figure 2-2 provides typical bond stress-

slip curves for the pullout test. HD refers too high-performance concrete (77MPa) with deformed bars. The 1, 2, 3 and 4 applies to 5 mm, 12 mm, 18 mm, and 26 mm bar diameters. The peak bond stress is markedly affected by the bar diameter, with the highest stress values for the smallest bar diameter (P. F. Bamonte & Gambarova, 2007).

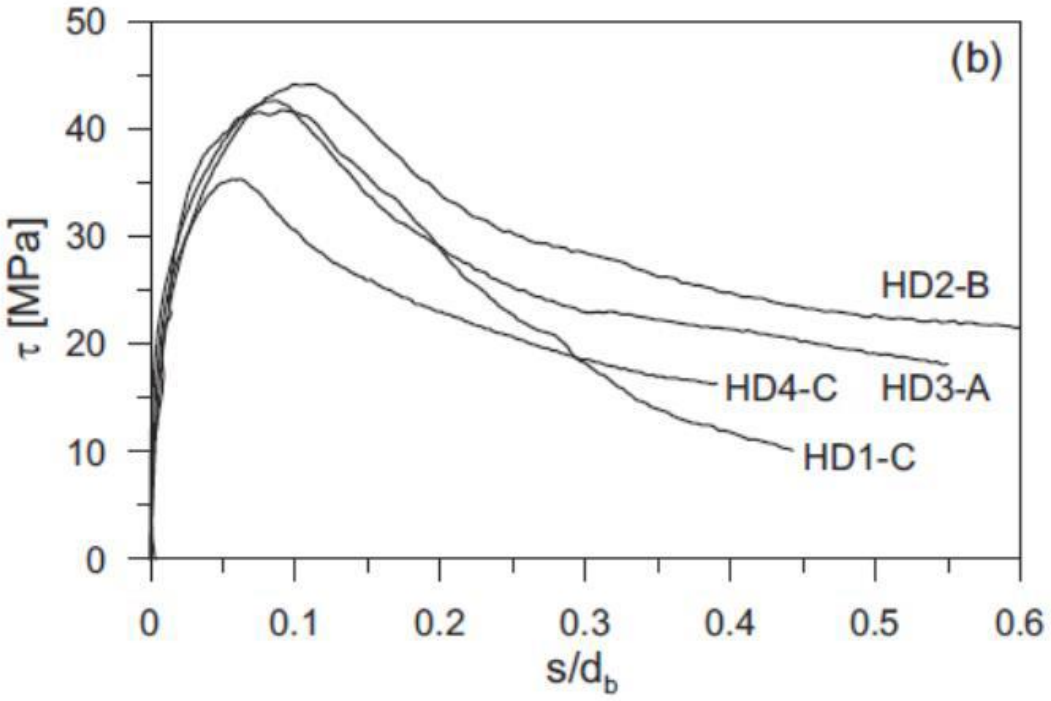

Figure 2-2 Typical bond stress/slip curves for deformed bars with HPC (P. F. Bamonte & Gambarova, 2007)

With reference to pull-out tests, a sketch of the bond-stress distribution along a smooth anchorage is presented in Figure 2-3.

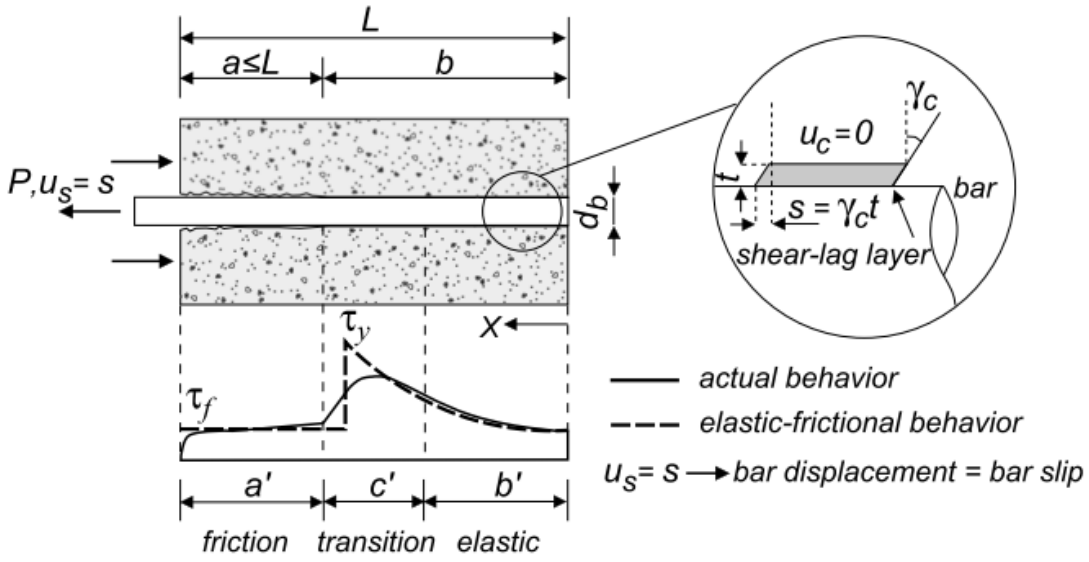

Figure 2-3 Qualitative distribution of the bond stress along a smooth, anchored bar, and elastic-fracturing-frictional model (Stang, Li, & Shah, 1990)

The bonding of moderately long anchorage in high-performance concrete is shown in Figure 2-4. For the given anchorage and load level, the local bar slip corresponds to the slip along the entire face. The local bond stress is τ_y, τ_f is the frictional strength, which is the residual bond strength, and k is the bond stiffness. The local bond stress/slip is $\tau = ks$, where bond action is fully effective due to contact at the interface. With localized shear strains in the concrete layers around the bar, these strains are equal to the slip for small strain values.

As shown in Figure 2-4, after exceeding the maximum local bond stress (τ_y), the bond stress decreases to the interfacial friction (τ_f).

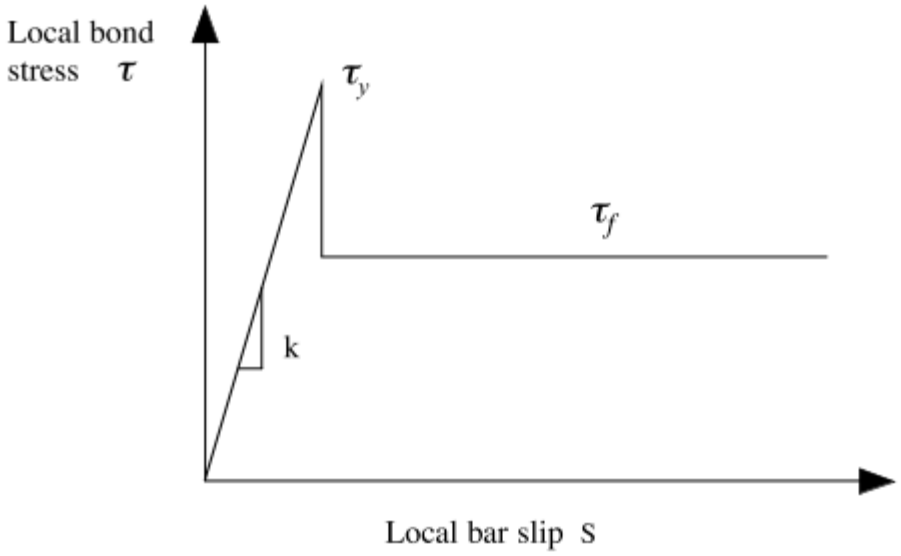

Figure 2-4 Simplified bond stress/slip law adopted in the modelling of smooth anchored bars (P. Bamonte, Coronelli, & Gambarova, 2003)

Figure 2-5 and Figure 2-6 illustrate the average bond stress responses for HPC and NSC reinforced with smooth bars. It was shown that there exists a substantial size effect in long anchored smooth bars for high performance and moderate strength concretes (P. Bamonte et al., 2003). [Note: the solid line in the graphs represents the stress criterion and the dashed line the energy criterion.]

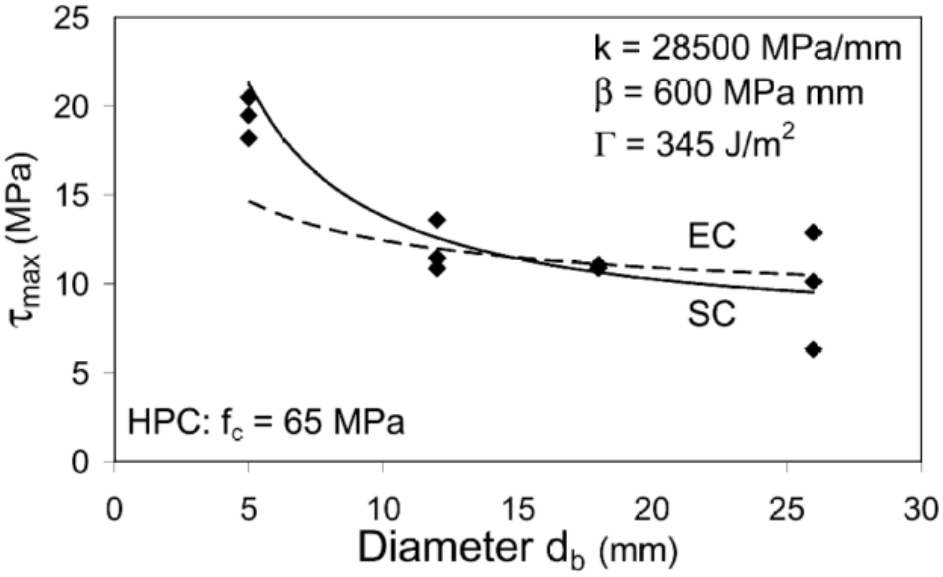

Figure 2-5 Typical bond stress/slip curves from pull-out tests on HPC specimens with smooth bars (P. Bamonte et al., 2003)

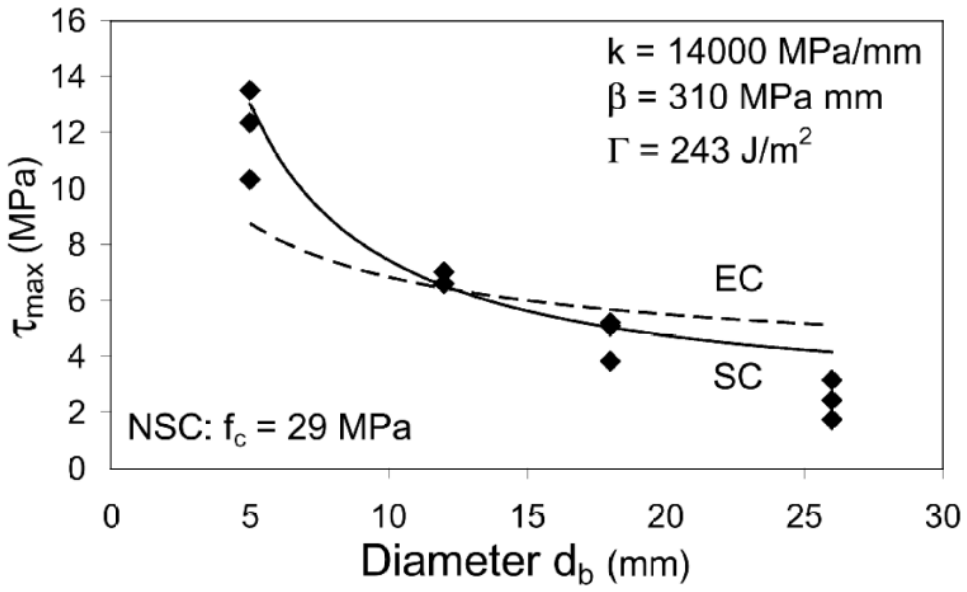

Figure 2-6 Typical bond stress/slip curves from pull-out tests on NSC specimens with smooth bars (P. Bamonte et al., 2003)

The bond in HPC is less size-dependant due to the greater tensile strength, homogeneity of the concrete, and chemical adhesion (silica fume aids in adhesion) that HPC exhibits at the bar-concrete interface.

2.3 Bond Strength

Given that the TSP uses smooth wire-mesh as internal reinforcement in the concrete overlay understanding the bond between this reinforcement and the concrete is critical to determine the extent to which the smooth reinforcement contributes to the strength capacity in addition to crack control.

The bond strength between smooth and deformed bars and the surrounding concrete is a critical factor to consider in design. Any issues in the bond can potentially make these types of bars problematic for reinforcing structures, particularly in areas of high seismic activity. Reinforcing steel provides strength through the bond with the concrete, thus degrading the bond can compromise the ability of the reinforced concrete to maintain load-carrying capacity (Fang, Lundgren, Chen, & Zhu, 2004). Smooth and deformed bars that are small in diameter have been found to have superior bond behaviours when compared with smooth and deformed bars that are large in diameter for a specific embedment length (P. Bamonte, Coronelli, & Gambarova, 2006). First, bond behaviour in small diameter bars is superior due to the beneficial ratio of the surface of the bar (where the bond stress develop) and the cross-section (where the tensile or compressive strengths develop) (P. Bamonte et al., 2006). Second, bond behaviour in small diameter bars is superior given the significant size effect that is related to both smooth and deformed bars (P. Bamonte et al., 2006). While smooth and deformed bars that are small in diameter have been found to outperform larger diameter bars in terms of bond strength, research has demonstrated differences in the use of smooth and deformed bars. Smooth bars have much poorer bond characteristics when compared with different types of deformed bars (Bamonte et al. 2006, and Fabbrocino et al. 2004). Structures reinforced with deformed bars are superior to similar structures with smooth bars as a result of the greatly improved bond strength with deformed bars (Fabbrocino et al., 2004). To improve on the poor bond strength, smooth bars have to be implemented with hooks at the end (Fabbrocino, Verderame, & Polese, 2007). Since the

introduction of deformed bars in the early 1970s, they have largely supplanted the use of smooth bars in reinforced concrete (Fabbrocino et al., 2005). Moreover, to address deficiencies associated with the use of smooth bars as reinforcement in concrete, restoration and retrofitting projects have been undertaken to ensure the safety of existing buildings, particularly those located in Europe (Fabbrocino et al., 2004). Fabrocino (2005) investigated the behaviour of anchored smooth rebar as a solution for bond deficiencies associated with these bars (Fabbrocino et al., 2005). Beam and pull-out tests have been conducted on several specimens. Figure 2-7 illustrates the different phases of the slip phenomenon in comparison with theoretical bond stress-slip models (MC 90). The peak value is higher in the experimental tests in comparison to the model; however, there is a better match with the residual bond stress. The experimental results are provided for two different beam test setups (Fabbrocino et al., 2005).

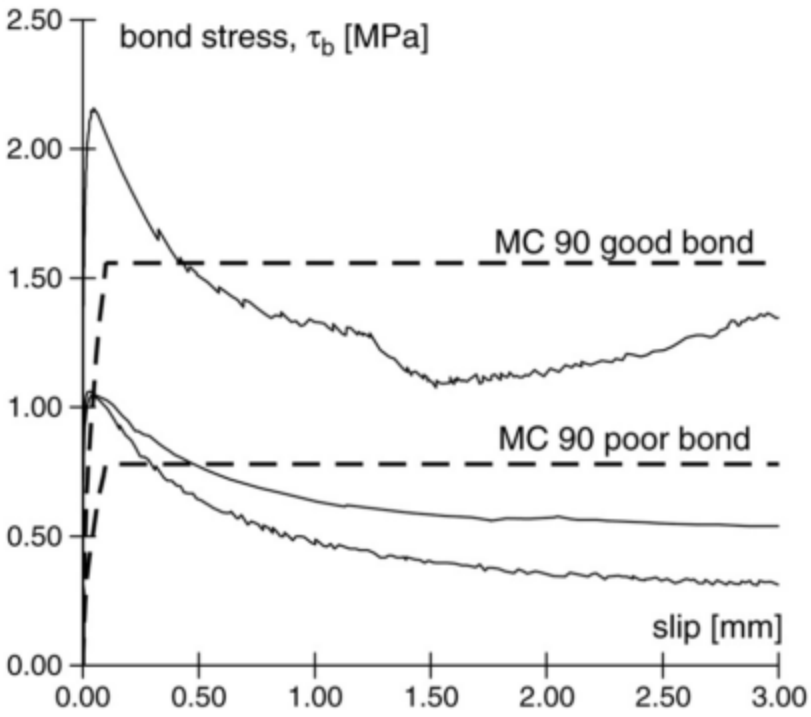

Figure 2-7 Beam test results: bond stress-slip (Fabbrocino et al., 2005)

Figure 2-8 shows the adhesion with negligible slips, interlocking with increasing slip up to the peak point on two different test setups for the pull-out tests. The arrangement for pull-out tests were for hooked smooth bars and straight smooth bars (Fabbrocino et al., 2005).

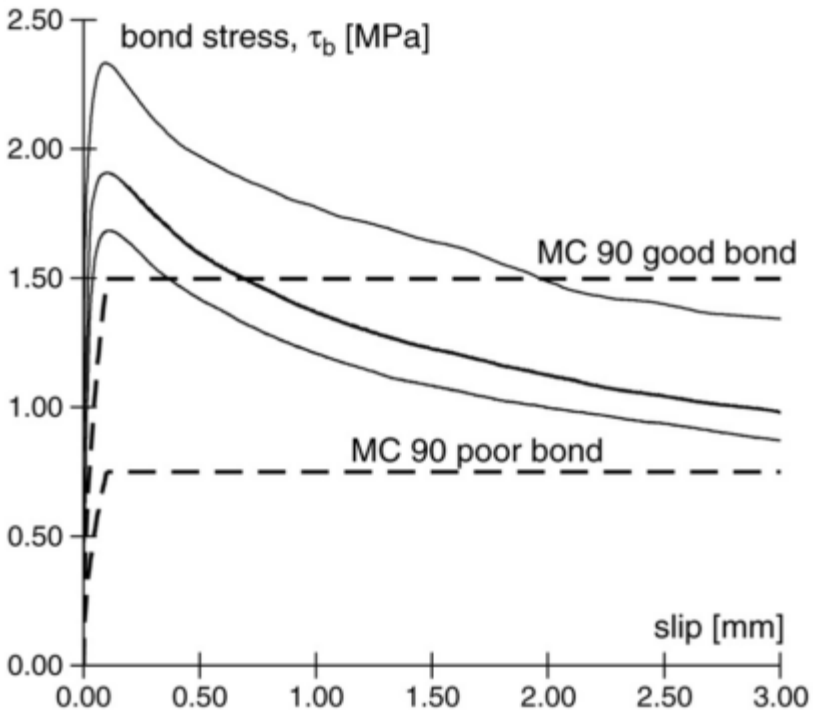

Figure 2-8 Pull-out test results: bond stress-slip (Fabbrocino et al., 2005)

2.4 Seismic Events and Deformed Reinforcement

While the TSP makes use of internal smooth wire-mesh, care must be taken in relying on such bars to provide reliable lateral strength, specifically under seismic loading.

The use of smooth or deformed bars plays a critical role in the performance of concrete structures in high seismically active zones. To ensure an acceptable response to seismic events, concrete structures require adequate reinforcement to protect them from becoming brittle and failing (Priestley, Verma, & Xiao, 1994). The reduced bond strength associated with smooth bars has led to a number of concerns regarding their ability to withstand seismic actions, particularly in those areas where seismic events are most common

(Verderame et al. 2008). Retrofitting has targeted structures reinforced with smooth bars by implementing different types of reinforcement to improve bond and ensure adequate tensile strength and bond required to sustain seismic activity (Bousias, Spathis, & Fardis, 2007). Among the different types of retrofitting options available, reinforced concrete jackets (RC jackets) and fibre-reinforced polymer (FRP) sheets have been most commonly used to strengthen structures containing smooth bars (Bousias et al., 2007).

Retrofitting structures containing smooth bars with reinforced concrete jackets is still the most commonly utilized method for shear walls and other types of reinforced concrete structures, specifically in Europe where vulnerability to seismic excitations is high (Bousias et al., 2007). Reinforcement through the use of RC jackets is the most commonly used reinforcement technique given its cost-effectiveness (Bousias et al., 2007). This is due to the familiarity with the method for engineers and the construction industry (Bousias et al., 2007). Also, RC jackets are particularly suitable for repairing severe damage to reinforced concrete structures, including shear walls and other types of reinforced concrete components (Bousias et al., 2007).

Bousias and Spathis (2007) tested two types of column sections with RC jackets: Type Q with 250 mm x 250 mm sectional dimensions; and type R with 400 mm x 400 mm sectional dimensions. The original columns were labelled Q-0L1 (Shape A) and Q-0L2 (Shape 2). These columns were internally reinforced with 4-14 mm-diameter smooth (plain) corner bars having yield stress 313 MPa. The transverse reinforcement of the original columns consisted of smooth 8 mm-diameter stirrups spaced at 200 mm on centers, anchored by a

135° hook at one end and a 90° hook at the other. The retrofitted columns were labelled Q-RCL1 (Shape C) and Q-RCL2 (Shape D) and were reinforced with 4-20 mm-diameter ribbed (deformed) bars with a yield stress of 487 MPa (Bousias et al., 2007) and a concrete jackets consisting of shotcrete (Gunite) with 75 mm thickness. The 4-20 mm bars were embedded into the foundation during the original column casting. Also, the jackets incorporated transverse reinforcing consisting of 10 mm perimeter ties at 100 mm spacing. Figure 2-9 showed the cross-section of the original and retrofitted columns.

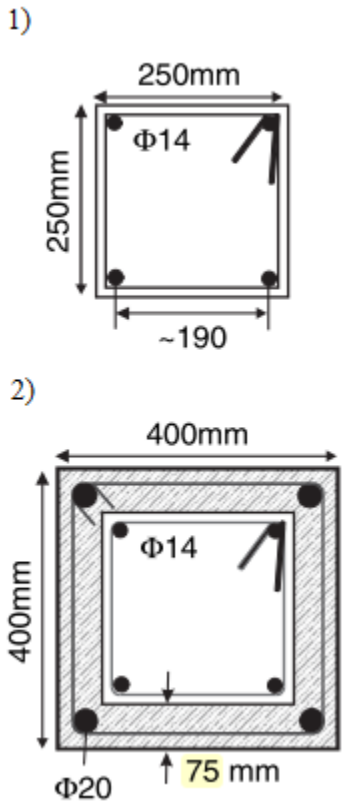

Figure 2-9 Cross section of the original column (1) and the retrofitted with the RC jacket (2) (Bousias et al., 2007)

Figure 2-10 provides the force-displacement responses for the columns before and after retrofitting.

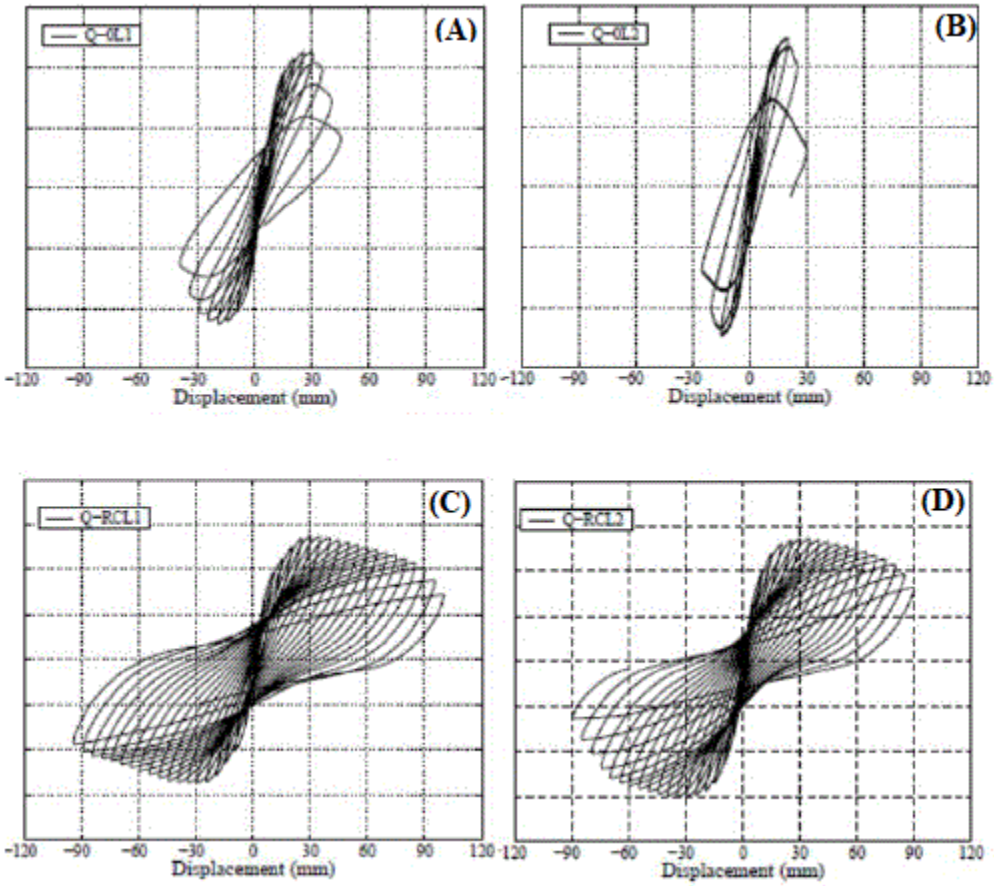

Figure 2-10 Q-type columns before and after retrofit (Bousias et al., 2007)

It should be noted that when concrete jackets have the right type of reinforcement, they can have a variety of positive effects on the structure (Bousias et al., 2007). RC jackets can improve the stiffness of the structure, as well as its flexural resistance (Bousias et al., 2007). These methods of reinforcement are also highly useful for addressing some of the most common structural problems related to the use of smooth bars in reinforced concrete

structures. RC jackets are effective at improving the deformation capacity of columns reinforced with smooth steel bars, potentially upgrading them to current standards for seismic resistance (Bousias et al., 2007).

2.5 Smooth Bars in Shear Walls

In modelling the TSP systems, care must be taken to account for the bond properties of the smooth wire-mesh reinforcement in the analyses.

Smooth bars and deformed bars have different interaction mechanisms at the interface of concrete and steel (Fernandes, Varum, & Costa, 2013). Due to the poor concrete-steel bond properties that exist for smooth bars, the problem of bar slippage is particularly important to note when using smooth rebar for reinforcing concrete structures (Fernandes et al., 2013). Research has documented the importance of considering the impact of bar slippage on reinforced concrete elements using smooth bars for reinforcement (Fernandes et al., 2013). Moreover, the current modelling strategies used by engineers to investigate and simulate these structures are lacking (Fernandes et al., 2013).

Given that the majority of these models have been designed for use with deformed bars, they are inadequate for the response typically observed with smooth bars (Fernandes et al., 2013). In response, models have been developed to specifically deal with smooth bars (Fernandes et al., 2013). These models are more effective in accounting for the bar slippage commonly observed with smooth bars when compared to deformed bars (Fernandes et al. 2013 and Braga et al. 2012).

2.6 Summary

The literature review provided background information on critical factors that would influence the lateral performance of the TSP systems investigated in this research. These factors included the bar size and the bond of smooth and deformed reinforcing bars. The influence of bar size, smooth and deformed bars and bond properties will be investigated as part of the comprehensive analyses of the TSP system. Given the lack of information on the TSP system, this study aims to quantify the in-plane lateral load performance when the system is used as a shear wall.

Chapter 3 Thin Shell Precast Wall

3.1 Background

Nexcon Inc., a subsidiary of Burnco Manufacturing, manufactures the "Thin Shell Precast (TSP)" panel system that is the subject of this research. The thin shell precast wall is an innovative, lightweight precast panel system. The patented system combines external light-gauge steel framing partially embedded into 2 to 3 inches (50 – 75 mm) of concrete. The lightweight panels were originally designed to act as load bearing vertical elements, foundation walls, floor slabs, and cladding to enclose pre-engineered structures. The panel system can be adjusted to accommodate different framing sizes, gauges, and spacing arrangements with or without insulation. Architectural finishes such as stone veneer and bricks can be easily accommodated.

The main advantages of this system come from the composite design, which results in shallow external steel joists, reducing the weight of the steel by approximately 30% and increasing the span length in comparison to standard non-composite design. In addition, the system provides comparably increased stiffness to improve deflection control and increased load capacity. Other benefits include considerable less on-site labour and quick installation, and the need for scaffolding for the building exterior during panel installation is eliminated. Applications for the panel system include low-rise housing, mid- and high-rise buildings, and commercial, industrial and retail buildings. However, the main drawback of the system is the lack of understanding of its in-plane lateral load capacity.

Currently, structures making use of the panels as wall elements rely on external bracing elements to sustain lateral loads. This research aims to understand better and to quantify the lateral load capacity of the Thin Shell Precast Wall.

The thin shell precast panels, when used as foundation walls, can be erected directly onto poured, on-site footings with minimal time and without the need for forming. The foundation walls are erected and backfilling can take place immediately following the poring of the slab on grade and installation of the first floor bracing. Figure 3-1 provides a structural drawing for the foundation wall while Figure 3-2 is a photo of the panel in the foundation wall configuration.

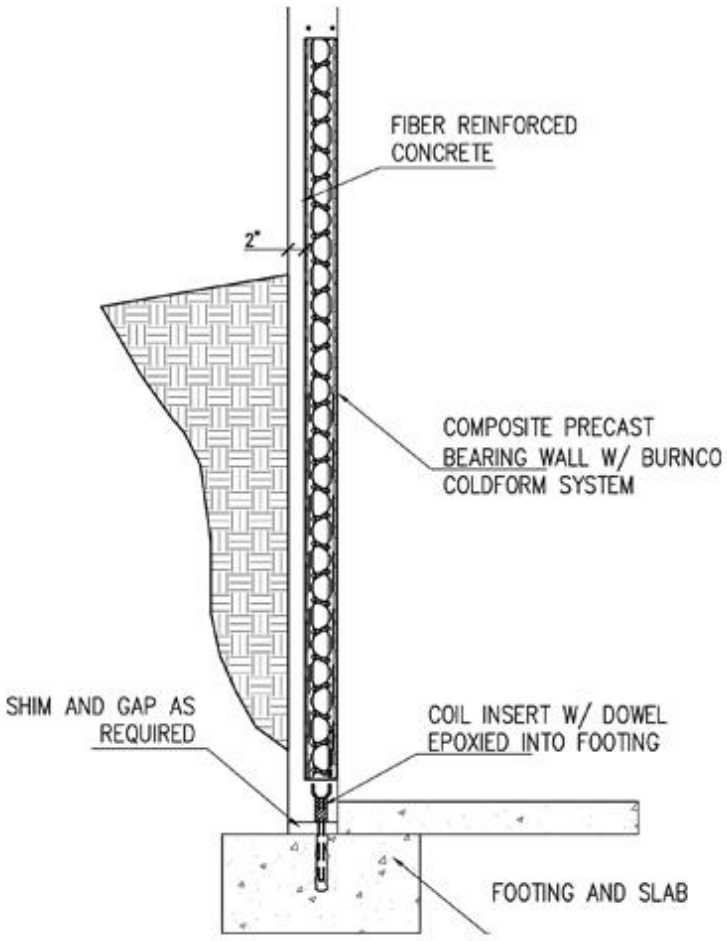

Figure 3-1 Thin shell panel as a foundation wall ("Products@www.nexcon.ca" 2011)

Figure 3-2 TSP panels erected on-site ("Products@www.nexcon.ca" 2011)

The Thin Shell Precast (TSP) panel as a floor slab is available in long clear spans and does not require surface preparation for floor coverings. The open web configuration of the external light gauge steel provides additional vertical and horizontal space for greater flexibility and ease of installation of electrical and mechanical systems. The system also eliminates the needs for most bulkheads. Figure 3-3 is a photo of the TSP in the floor slab configuration.

Figure 3-3 TSP panel as a floor slab ("Products @www.nexcon.ca," 2011)

3.2 Design of the Wall

Design of the composite TSP panel is achieved by utilizing light gauge steel joists in combination with a thin cover of concrete, connected by mechanical means and deflecting as a single unit when subjected to load. Composite action between the light gauge steel and the cover concrete cover is achieved by embedding the flange of the external joist into the concrete cover. The flange contains special embossing to trap the concrete and prevent it from shearing or delaminating from the steel surface. Previous laboratory tests confirmed that the steel embedded into the concrete provides full shear bonding.

To compute the section properties of the composite section of the TSP panel to determine the allowable strength under service loads and deflections, the "Transformed Area

Method" is used. The ultimate strength calculations of the TSP panel follow the Canadian Standard Association (CSA) A23.3 Design of Concrete Structures Clause 14. To comply with the strength and serviceability requirements, the wall must be reinforced with an adequate amount of horizontal and vertical reinforcement.

The TSP is being considered for two different shear wall configurations to resist in-plane lateral loads. The slender wall panel has a height of 3000 mm and width of 1800 mm; while the squat wall panel has an elevation of 3000 mm and the width of 5000 mm. The slender wall configuration is intended for applications in high-rise buildings; whereas the squat walls are considered for low to medium rise buildings. Figure 3-4 illustrates the squat TSP wall for a specific project.

Figure 3-4 Elevation view of squat precast panel

The material specifications and depth of the panels are the same for both the slender and squat wall panels. Figure 3-4 illustrates that the wall contains a concrete panel that is connected to exterior light gauge steel joists that are embedded in the concrete panel. Figure 3-5 provides a side view of the squat wall panel.

Figure 3-5 Side view of squat wall panel

Figure 3-6 is a rendering of the different applications of the composite panels including a floor slab, bearing wall, and inclined roof.

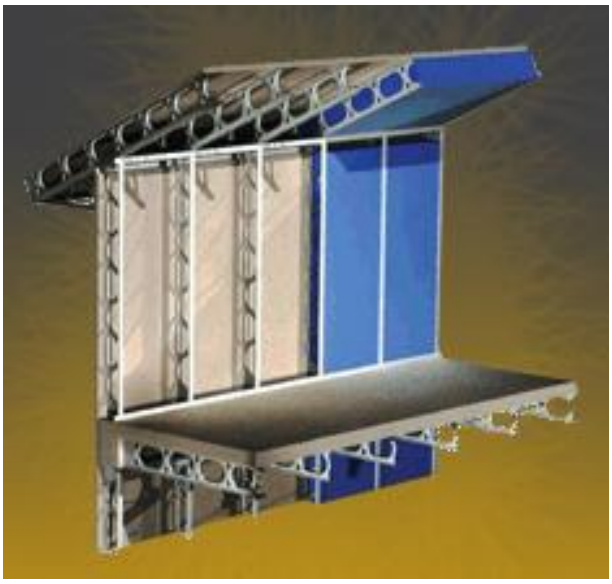

Figure 3-6 Thin shell precast panel applications ("About @ www.nexcon.ca," 2011)

As is evident in Figure 3-3 and Figure 3-6, the exterior steel are located on one side of the concrete panel; the side that is subjected to tensile stresses. The original design suggested a spacing of 600 mm between exterior steel. The flanges of the light-gauge steel are embedded into the thin concrete panel to promote composite action. The steel joists are Grade 50 (50 ksi minimum yield strength), approximately 345 MPa. Approximately 133 mm^2 of the cross-sectional area of the steel is embedded in the concrete panel. Figure 3-7 illustrates the cross-section of a typical external steel joist. The total cross-sectional area of the weak section is 385 mm^2. [Note that the figure provides a section at the location of perforation in the steel (see Figure 3-5).]

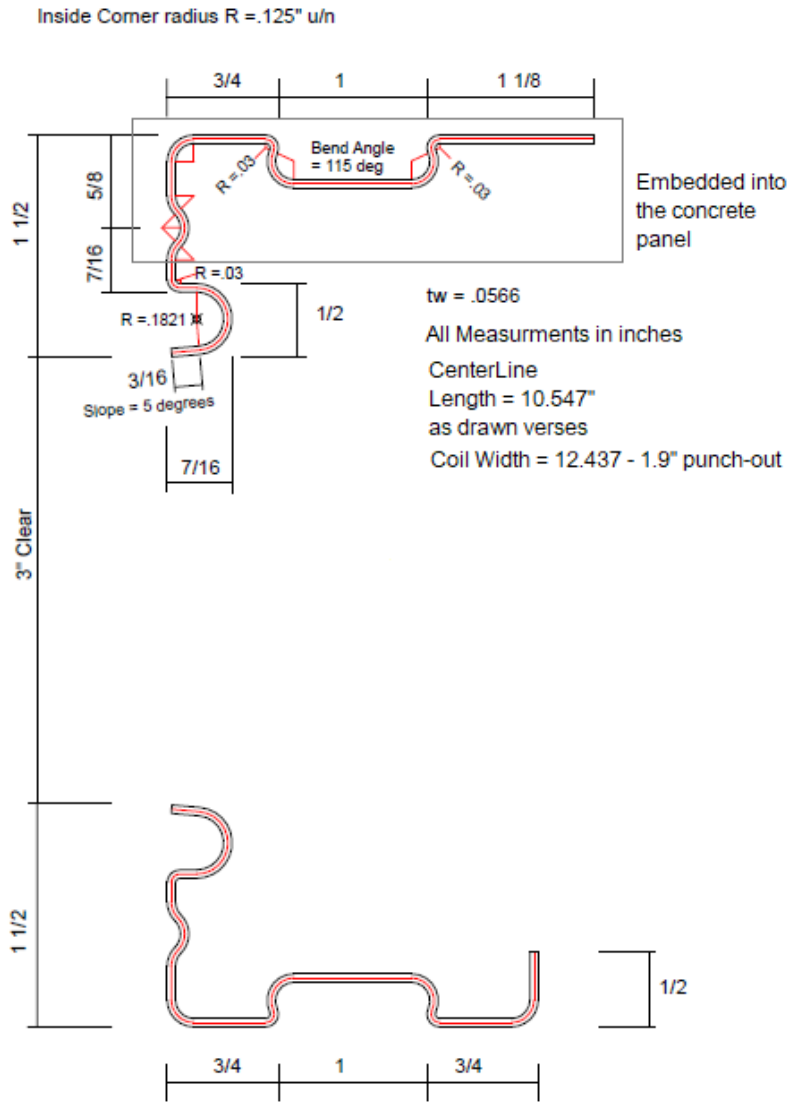

Figure 3-7 Weak cross-section of the exterior steel (Angle, 2015)

Figure 3-7 provides the weak section of the steel which includes the perforation. This section is important in the lateral performance of the wall as it is the critical section of the external steel.

The thin concrete panel is internally reinforced with 6 mm-diameter smooth wire-mesh. The wire-mesh has a spacing of 150 mm in the horizontal direction and 150 mm in the vertical direction. The target compressive strength of the concrete panel is 25 MPa, and the design yield strength of the wire-mesh is 485 MPa with an ultimate strength of 600 MPa. Figure 3-8 is an illustration of the concrete panel with exposed internal wire-mesh.

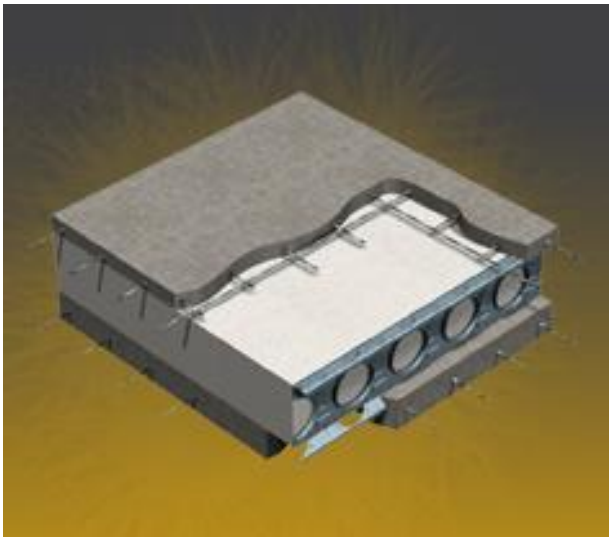

Figure 3-8 Thin concrete panel with internal and external reinforcement ("About@www.nexcon.ca" 2011)

The panels incorporate top and bottom longitudinal beams that serve as elements upon which other structural members rest and as a means to connect to the structure, respectively. The beams are 250 mm in width and 250 mm in height and are reinforced longitudinally with 4-15M deformed bars that span the entire length of the beam. The concrete cover in the top and bottom beams is 50 mm. Also, 10M stirrups are placed along

the 4-15M bars at a 300 mm spacing. The external light gauge steel extends 100 mm into the beams at either end. Figure 3-9 illustrates the top and bottom beams.

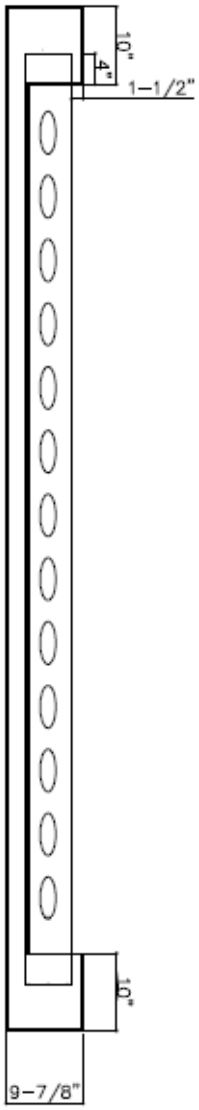

Figure 3-9 Panel cross-section with top and bottom beams (Karimi, 2015a)

Figure 3-10 provides an elevation of the slender-type of the thin shell precast wall system as constructed for field application.

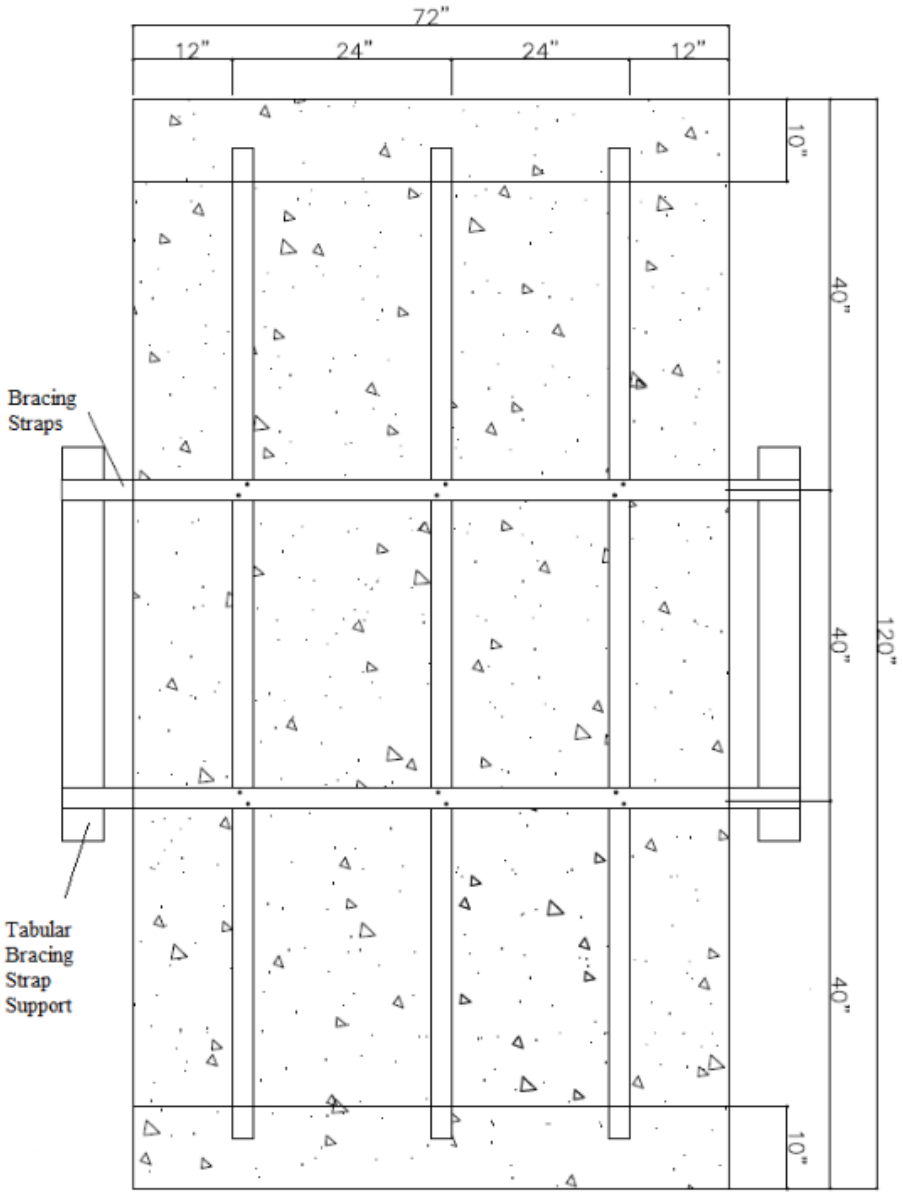

Figure 3-10 Elevation view of the slender panel with bracing support (Karimi, 2015a)

As part of the construction of the panels, and in preparation for the field, horizontal bracing straps (65 mm wide, 1.5 mm thick, and 1800 mm long) are connected to the external steel

joists with two self-drilling wafer headed screws. The spacing of the horizontal straps is 1000 mm.

3.3 Current Applications

The current application of the thin shell precast system is limited to one- to two-storey structures. Currently, the system serves as a floor slab to resist gravity loading, as a bearing wall to withstand axial loads, as a foundation wall and cladding that can support out-plane loading. Lateral loads due to wind and earthquake are controlled by a secondary bracing system (cross bracing). Figure 3-11 illustrates the panel system in a two-storey configuration with cross bracing.

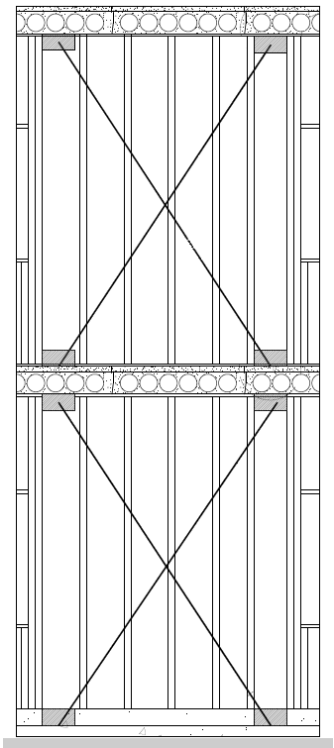

Figure 3-11 Secondary bracing for in-plane lateral resistance (Tuck, 2014)

The focus of this current study is to assess the in-plane lateral load performance of the Thin Shell Precast Panel without the secondary cross bracing. To achieve this, an understanding of the contribution of the exterior steel to the lateral load resistance is critical.

Chapter 4 Nonlinear Analysis Methodology

4.1 Introduction

Program VecTor2 was developed with capabilities to perform both linear and nonlinear finite element analysis of two-dimensional membrane-type reinforced concrete structures. The program was developed at the University of Toronto over the past four decades by researchers working on nonlinear behaviour of reinforced concrete structures. The program offers assessments of structural performance, including strength, concrete cracking, reinforcement yielding, failure mode, displacements, and post-peak behaviour, to name a few. VecTor2 has been corroborated through experimental test data to verify the ability to predict the load-deformation response for different types of reinforced concrete structures subjected to monotonic, cyclic and reverse cyclic loading. VecTor2 is based on the MCFT (Modified Compression Field Theory) (Frank J. Vecchio & Collins, 1986) and the DSFM (Disturbed Stress Field Model)(F. J. Vecchio, 2000). VecTor2 was developed initially with the MCFT and later expanded to include the DSFM. The following sections expand on the MCFT and DSFM.

4.2 Modified Compression Field Theory (MCFT)

The Modified Compression Field Theory (MCFT) (Vecchio and Collins 1986) is an analytical model that predicts the load-deformation response of reinforced concrete membrane elements subjected to shear and normal stresses (Wong, Vecchio, & Trommels,

2000). Figure 4-1 illustrates the components of a typical concrete panel from which the equilibrium, compatibility, and constitutive relations were derived.

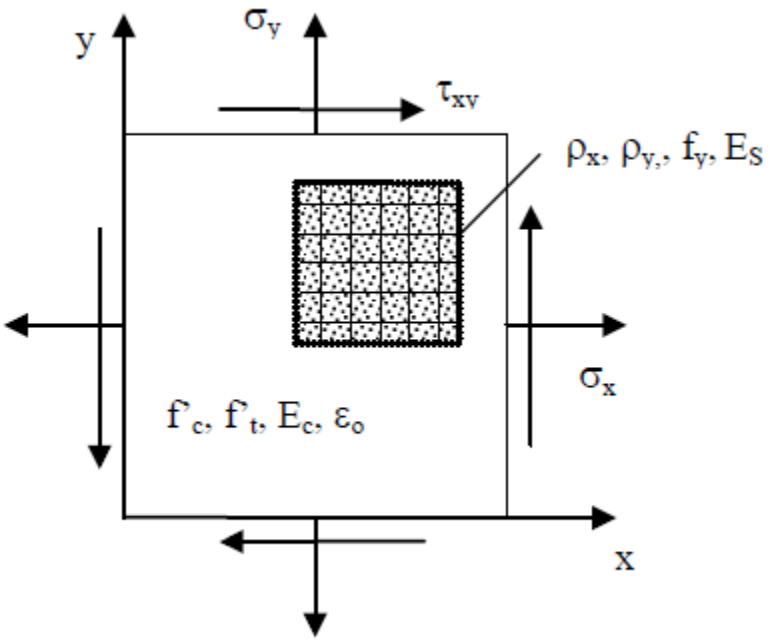

Figure 4-1 Reinforced concrete element subjected to in-plane loading (Wong et al., 2000)

The MCFT determines the average and local strains and stresses of the concrete and reinforcement, and the widths and orientation of cracks throughout the load-deformation response. Based on this information, the failure mode can be determined (Wong et al., 2000). The MCFT forms its basis from three different sets of the relationships between the concrete and reinforcement: compatibility, equilibrium, and constitutive. Compatibility relates the average strain in the concrete with the average strain in the reinforcement; equilibrium relates the average stress in concrete and reinforcement to the external forces

(stresses); and the constitutive relationships provide a link between the average strains and the average stresses in the materials.

In the development of the MCFT, a number of assumptions were implemented. The stress and cracks in the concrete are uniformly distributed, the principal strain direction coincides with the primary stress direction, a separate constitutive relationship exists for concrete and reinforcement, perfect bonding exists between the concrete and reinforcement, negligible shear stress on the reinforcement, and unique state of stress for each strain state.

The following sections provide a brief overview of the compatibility, equilibrium and constitutive relationships of the MCFT. Full details can be found elsewhere (Wong et al., 2000).

4.2.1 Compatibility Relationships

For compatibility relationships, perfect bonding between the reinforcement and concrete is assumed. Therefore the total strain experienced by the concrete is the same as the total strain of the reinforcement. Figure 4-2 depicts the average concrete strains in a typical concrete element.

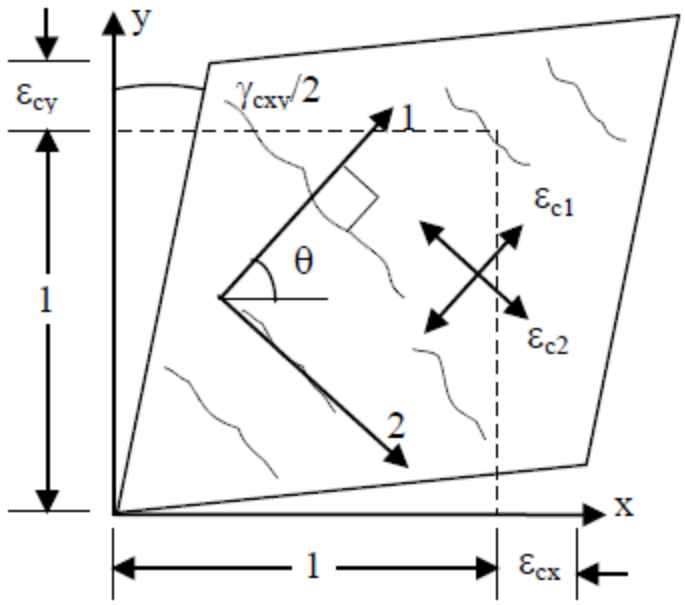

Figure 4-2 Average concrete strain in two directions (Wong et al., 2000)

The average principal strains in the concrete are computed from the total strains by the following equation:

$$\varepsilon_{c2}, \varepsilon_{c1} = \frac{1}{2}(\varepsilon_x + \varepsilon_y) \pm \frac{1}{2}\left((\varepsilon_x - \varepsilon_y)^2 + {\gamma_{xy}}^2\right)^{\frac{1}{2}} \quad \textbf{(4-1)}$$

Where ε_{c1} and ε_{c2} are the principal average tensile and compressive strains in the concrete, respectively; γ_{xy} is the shear strain of the element; and ε_x and ε_y are the strain in x and y directions, respectively. The relationship is derived from Mohr's circle. Also, the principal tensile strain direction is calculated as follows:

$$\theta = \theta_\varepsilon = \theta_\sigma = \frac{1}{2} tan^{-1}\left(\frac{\gamma_{xy}}{\varepsilon_x - \varepsilon_y}\right) \quad \textbf{(4-2)}$$

Where θ_ε and θ_σ are the orientations of the average principal tensile strain axis and stress axis, respectively.

4.2.2 Equilibrium Relationships

The equilibrium relationships balance the applied normal stresses in x- and y-directions with the average stresses in the concrete and reinforcement. Figure 4-3 illustrates the external and internal stresses on a reinforced concrete element.

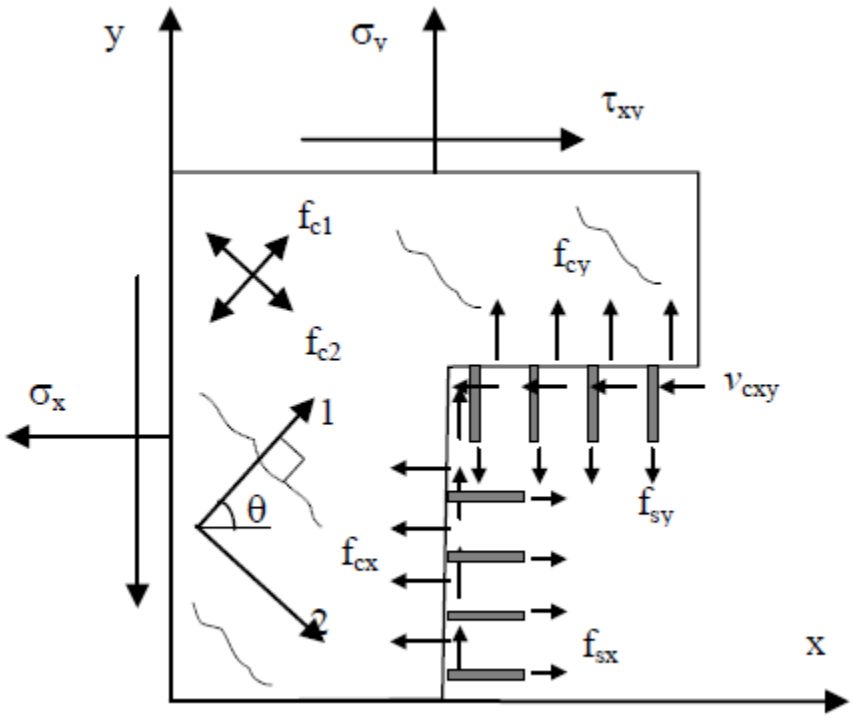

Figure 4-3 Free body diagram of a reinforced concrete element (Wong et al., 2000)

The equilibrium equations are summarized as follows:

$$\sigma_x = f_{cx} + \rho_{sx} f_{sx} \quad \textbf{(4-3)}$$

$$\sigma_y = f_{cy} + \rho_{sy} f_{sy} \quad \textbf{(4-4)}$$

$$\tau_{xy} = v_{cxy} \quad \textbf{(4-5)}$$

Where ρ_{sx} and ρ_{sy} are the reinforcement ratios in the x-and y-directions, respectively. σ_x and σ_y are applied normal stresses in the x-direction and y-direction, respectively. f_{sx} and f_{sy} are average stresses in the reinforcement parallel to the x-direction and y-direction, respectively.

4.2.3 Constitutive Relationships

Vecchio and Collins (1986) defined constitutive relationships to link the average strains to the average stresses. The original constitutive relations were developed from test results of thirty panels that were subjected to in-plane stress. The constitutive relationship that relates the principal compressive strength (f_{c2}) in the concrete to principal compressive strain (ε_{c2}) is as follows:

$$f_{c2} = \frac{f_c' \left(2\left({\varepsilon_{c2}}/{\varepsilon_0}\right) - \left(\frac{\varepsilon_{c2}}{\varepsilon_0}\right)^2\right)}{0.8 - 0.34\left(\frac{\varepsilon_{c1}}{\varepsilon_0}\right)} \quad \textbf{(4-6)}$$

Where ε_0 is the strain at the peak compressive strength for the concrete. ε_{c1} and ε_{c2} are average net concrete strain in the principal 1- and 2–directions. The principal tensile strength of the concrete before cracking is determined from the following formulation:

$$f_{c1} = E_c \times \varepsilon_{c1} \qquad for\ 0 < \varepsilon_{c1} < \varepsilon_{cr} \tag{4-7}$$

Where E_c is the initial tangent stiffness of the concrete and is calculated from:

$$E_c = 5000\sqrt{f_c'} \tag{4-8}$$

The cracking strain of the concrete, ε_{cr}, in Equation (4-6) is calculated from:

$$\varepsilon_{cr} = \frac{f_t'}{E_c} \tag{4-9}$$

The uniaxial cracking strength of the concrete, f'_t, is determined using the following formulation:

$$f'_t = 0.33\sqrt{f_c'} \tag{4-10}$$

Before cracking, the concrete is assumed to exhibit a linear response as captured by Equation (4-7). After cracking, tensile stress exists between the cracked concrete and the reinforcement. This phenomenon is called tension stiffening. The formulation to calculate this follows:

$$f_{c1} = \frac{f_t'}{1 + \sqrt{200\varepsilon_{c1}}} \tag{4-11}$$

Although the MCFT predicts the response for a number of membrane-type structures subjected to various load scenarios, deficiencies have been noted under certain situations. In response, the Distributed Stress Field Model was developed (Vecchio, 2000) to address these deficiencies as discussed in the following section.

4.3 Disturbed Stress Field Model (DSFM)

Although the MCFT provides satisfactory results for the behaviour of cracked reinforced concrete elements subjected to in-plane forces, some deficiencies have been noted in specific situations. The accuracy of the MCFT is reduced under the following conditions:

1) The shear strength and stiffness is underestimated in reinforced concrete panels with large quantities of reinforcing in two directions and under biaxial compression loading; and
2) The shear strength and stiffness is overestimated in lightly reinforced panels under uniaxial tension and shear. These problems tend to arise in lightly reinforced concrete structures that experience crack shear slip.

The Distributed Stress Field Model (DSFM) builds upon the MCFT by providing explicit consideration to crack shear-slip deformations in the compatibility, equilibrium and constitutive relationships. Essentially, strains that develop due to discrete slip is treated as a component in the total strain calculation. In doing so, the principal stress field is no longer assumed to coincide with the principal strain field; one of the central assumptions of the MCFT.

4.3.1 DSFM Compatibility Relationships

As stated above, the MFCT considered the principal stress orientation to be coincident with the principal strain direction, and no explicit consideration was given to discrete shear slip. A separate check was performed to ensure the stress on the crack was below a limiting value. Vecchio (F. J. Vecchio, 2000) discussed how the orientation of the principal strain

field could diverge from the principal stress field in a rotating crack model. The DSFM harmonizes the crack shear-slip deformation phenomena as illustrated in Figure 4-4.

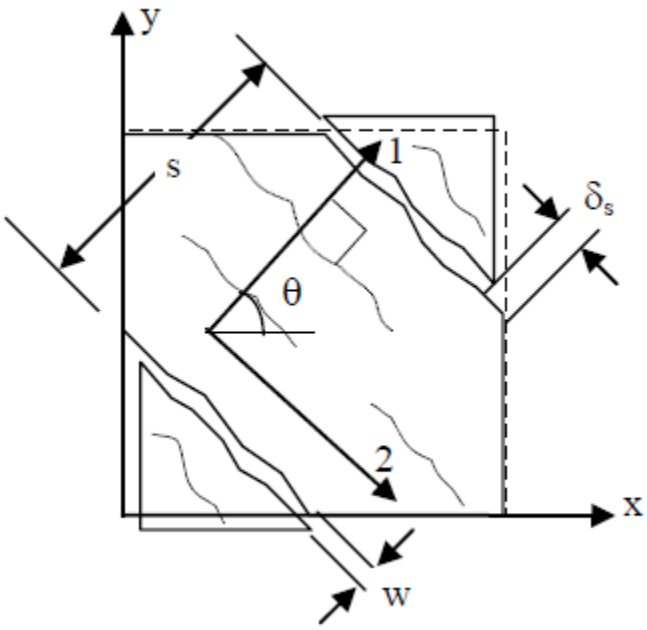

Figure 4-4 Crack shear slip phenomena (Wong et al., 2000)

Within the formulations of the DSFM, the strain due to stress and the strain due to shear slip are separate components in determining the total strain as follows:

$$\varepsilon_x = \varepsilon_{cx} + \varepsilon_x^s \quad \textbf{(4-12)}$$

$$\varepsilon_y = \varepsilon_{cy} + \varepsilon_y^s \quad \textbf{(4-13)}$$

$$\gamma_{xy} = \gamma_{cxy} + \gamma_{xy}^s \quad \textbf{(4-14)}$$

Where ε_x^s , ε_y^s and γ_{xy}^s are the crack slip-shear components. γ_{cxy} is the average net concrete shear strain and γ_{xy} is total shear strain. These components are calculated from the following formulations:

$$\varepsilon_x^s = -\frac{1}{2}\gamma_s \sin(2\theta) \quad \textbf{(4-15)}$$

$$\varepsilon_y^s = \frac{1}{2}\gamma_s \sin(2\theta) \quad \textbf{(4-16)}$$

$$\gamma_{xy}^s = \gamma_s \cos(2\theta) \quad \textbf{(4-17)}$$

γ_{xy}^s is average shear strain due to shear slip, γ_s is average crack slip shear strain, which is established from the crack slip deformation (δ_s) divided by average crack spacing (s).

$$\gamma_s = \frac{\delta_s}{s} \quad \textbf{(4-18)}$$

The orientation of the principal stresses θ is calculated using Mohr's circle as follows:

$$\theta = \frac{1}{2}\, tan^{-1}\left(\frac{\gamma_{cxy}}{\varepsilon_{cx} - \varepsilon_{cy}}\right) \quad \textbf{(4-19)}$$

The orientation of the principal strain field (θ_ε) can be calculated from Equation 4-18 by substituting the net concrete strains with the apparent total strains. The lag in the rotation in the principal stress direction and apparent principal strain direction is the difference between these two orientation calculations. The DSFM is similar to the MCFT in that perfect bond is assumed to exist.

4.3.2 DSFM Equilibrium Relationships

The equilibrium relationships are the same for both the MCFT and the DSFM and are governed by Equations 4-3 to 4-5. Also, the DSFM gives explicit consideration to the average concrete tensile stresses that can be transferred across the crack and the development of shear stresses on the crack. The equilibrium equations to capture these effects are provided below:

$$f_{c1} = \rho_x(f_{s\,crx} - f_{sx})cos^2\theta_{nx} + \rho_y(f_{s\,cry} - f_{sy})cos^2\theta_{ny} \quad \textbf{(4-20)}$$

$$\vartheta_{ci} = \rho_x(f_{s\,crx} - f_{sx})cos^2\theta_{nx}.sin\theta_{nx} + \rho_y(f_{s\,cry} - f_{sy})cos^2\theta_{ny}.sin\theta_{nx} \quad \textbf{(4-21)}$$

Where θ_{nx} and θ_{ny} are the angles between the normal to crack surface and the longitudinal axes of the reinforcement with respect to the x- and y-directions. ϑ_{ci} is local concrete shear stress at a crack, $f_{s\,crx}$ and $f_{s\,cry}$ are the local reinforcement stresses at a crack parallel to the x-direction and y-direction, respectively, and f_{sx} and f_{sy} are average reinforcement stresses parallel to the x-direction and y-direction, respectively.

4.3.3 DSFM Constitutive Relationships

In the development of the DSFM, the constitutive relationships were revised. The softening effect of concrete in compression due to co-existing transverse tensile straining was modified to take into account a further reduction factor β_d, defined as follows:

$$\beta_d = \frac{1}{1 + c_s c_d} \leq 1.0 \quad \textbf{(4-22)}$$

Where c_s represents the softening effect due to transverse tensile strains in the concrete and c_d represents the effect of element slip deformation. The parameter c_s is calculated with the following equation:

$$c_d = 0.35\left(-\frac{\varepsilon_{c1}}{\varepsilon_{c2}} - 0.28\right)^{0.8} \quad \textbf{(4-23)}$$

In the MCFT, c_s is implicitly set to unity, and compression softening is affected only by co-existing tensile strains. In the DSFM, c_s is set to 0.55. The compression softening effect is used to determine the peak compression strength and the corresponding strain as follows:

$$f_p = -\beta_d f_c' \quad \textbf{(4-24)}$$

$$\varepsilon_p = -\beta_d \varepsilon_0 \quad \textbf{(4-25)}$$

The compression softened strength and strain are implemented into a suitable compression response relationship to establish the principal compressive stress (f_{c2}) curve as a function of the net principal strain as follows:

$$f_{c2} = f_p \frac{n\left({\varepsilon_{c2}}/{\varepsilon_p}\right)}{(n-1) + \left(\frac{\varepsilon_{c2}}{\varepsilon_p}\right)^{nk}} \quad \textbf{(4-26)}$$

Where n is:

$$n = 0.80 - {f_p}/{17} \quad \textbf{(4-27)}$$

And k is:

$$k = \begin{cases} 1.0 & for\ \varepsilon_p < \varepsilon_{c2} < 0 \\ 0.67 - {f_p}/{62} & for\ \varepsilon_{c2} < \varepsilon_p < 0 \end{cases} \quad \textbf{(4-28)}$$

The behaviour of concrete in tension (f_{c1}) is assumed linear elastic prior to cracking. Post-cracking, tension stiffening is considered ($f_{c1}{}^{a}$). The formulations for pre- and post-cracking are as follows:

$$k = \begin{cases} f_{c1} = E_c . \varepsilon_{c1} & for\ 0 < \varepsilon_{c1} < \varepsilon_{cr} \\ f_{c1}^{a} = \dfrac{f_t{}'}{1 + \sqrt{c_t \varepsilon_{c1}}} & for\ \varepsilon_{cr} < \varepsilon_{c1} \end{cases} \quad \textbf{(4-29)}$$

Bentz (1999) suggested a coefficient c_t within the tension stiffening formulation to account for reinforcement bond characteristics in concrete:

$$c_t = 2.2\ m \quad \textbf{(4-30)}$$

Where m is dependent on the bar diameter, steel reinforcement ratio, and number of reinforcing bars. In addition to the average tensile stress for cracked concrete based on tension stiffening (f_{c1}^{a}), tension softening is also considered in the post-cracking state in cases where there is little to no reinforcement. In the analysis of concrete structures, the larger of the tension stiffening or tension softening value governs. Detailed formulations for both effects are readily available elsewhere (Wong et al., 2000).

4.4 Finite Element Operation

The finite element method incorporated in Program VecTor2 is displacement-based. The following sections provide an overview of the finite element formulation.

4.4.1 Composite Material Stiffness Matrix

The total strain experienced by a composite element is represented by the matrix $[\varepsilon] = [\varepsilon_x, \varepsilon_y, \gamma_{xy}]$. ε_x and ε_y represent the total strain in x-direction and y-direction, respectively, and γ_{xy} represents the total shear strain. Considering the concrete, the total strain contains the net concrete strain (ε_c), which is used to establish the stresses in the material. Strains due to lateral expansion, thermal effects, pre-straining and shrinkage are handled as elastic strain offsets (ε_c^0). Residual strains that arise during cyclic loading are treated separately as plastic offsets (ε_c^p), and slip along the crack is explicitly considered as it own strain component (ε^s). The total strain is the sum of the various strain components as follows:

$$[\varepsilon] = [\varepsilon_c] + [\varepsilon_c^0] + [\varepsilon_c^p] + [\varepsilon^s] \quad \textbf{(4-31)}$$

Similarly, the total strain in the reinforcement consists of various components. The thermal effects and restraining are considered as elastic strain offsets, and residual strains due to cyclic loading are treated as plastic strain offsets. The total strain in the reinforcement is determined from the following:

$$[\varepsilon] = [\varepsilon_s] + [\varepsilon_s^0] + [\varepsilon_s^p] \quad \textbf{(4-32)}$$

Where $[\varepsilon_s]$ is the net strain in the reinforcement, $[\varepsilon_s^0]$ is the elastic strain offset, and $[\varepsilon_s^p]$ is the plastic strain offset.

The total strains are related to the overall stress by the composite material stiffness matrix [*D*]:

$$[\sigma] = [D][\varepsilon] \quad \textbf{(4-33)}$$

The composite material stiffness matrix is the sum of the concrete material stiffness matrix and the reinforcement material stiffness matrix:

$$[D] = [D_c] + \sum_{i=1}^{n} [D_s]_i \quad \textbf{(4-34)}$$

The concrete material stiffness matrix ($[D_c]'$) is calculated based on principal stress directions as follows:

$$[D_c]' = \begin{bmatrix} \overline{E_{c1}} & 0 & 0 \\ 0 & \overline{E_{c2}} & 0 \\ 0 & 0 & \overline{G_c} \end{bmatrix} \quad \textbf{(4-35)}$$

$\overline{E_{c1}}$ and $\overline{E_{c2}}$ are the secant moduli of the concrete in the principal tensile and compressive directions, respectively, and $\overline{G_c}$ is the secant shear modulus of concrete. Figure 4-5 illustrates the secant modulus for concrete.

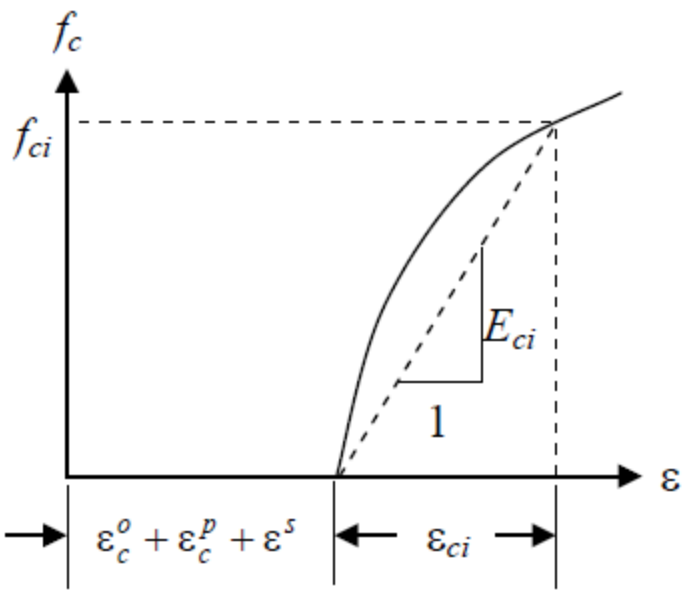

Figure 4-5 Secant stiffness modulus for concrete (Wong et al., 2000)

The secant stiffness is calculated from the principal stresses and principal strains:

$$\overline{E_{c1}} = \frac{f_{c1}}{\varepsilon_{c1}}\,;\, \overline{E_{c2}} = \frac{f_{c2}}{\varepsilon_{c2}} \quad \textbf{(4-36)}$$

$$\overline{G_c} = \frac{\overline{E_{c1}}.\overline{E_{c2}}}{\overline{E_{c1}} + \overline{E_{c2}}} \quad \textbf{(4-37)}$$

The reinforcement resists forces along its axis, which is reflected in the material stiffness matrix as follows:

$$[D_s]_i{}' = \begin{bmatrix} \overline{\rho_i.E_{si}} & 0 & 0 \\ 0 & 0 & 0 \\ 0 & 0 & 0 \end{bmatrix} \quad \textbf{(4-38)}$$

Where ρ_i is the reinforcement ratio for the i^{th} reinforcement component. The secant stiffness for the reinforcement is illustrated in Figure 4-6 below.

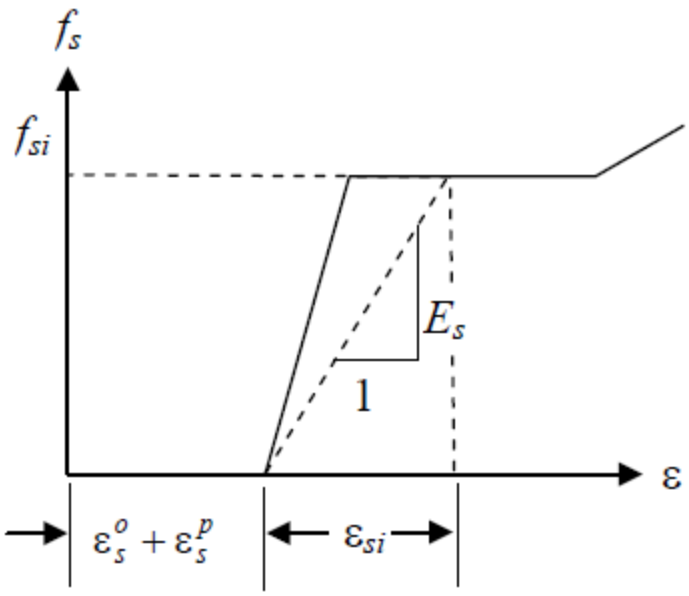

Figure 4-6 Secant stiffness modulus for reinforcement (Wong et al., 2000)

The secant stiffness for the reinforcement is calculated from the following expression:

$$\overline{E_{si}} = \frac{f_{si}}{\varepsilon_{si}} \quad \textbf{(4-39)}$$

4.4.2 Element Stiffness Matrices

The element stiffness matrix $[k]$ relates nodal forces to nodal displacements, and is established from the composite material stiffness matrix as follows:

$$[k] = \int [B]^T [D][B] dV \quad \textbf{(4-40)}$$

Where $[B]$ is the strain-displacement matrix and $[D]$ is the composite material stiffness matrix. The element stiffness matrix can be separated into contributions from the concrete $[k_c]$ and the reinforcement $[k_s]$.

The element stiffness matrix performs calculations on the total nodal displacements; therefore, it is necessary to subtract the nodal forces that arise from strain offsets and crack shear slip. This can be achieved through the use of a pseudo nodal load vector. For concrete, the offset and crack shear slip strains are resolved into the x- and y-axes as follows:

$$[\varepsilon_c^o] = \begin{bmatrix} \varepsilon_c^o \\ \varepsilon_c^o \\ 0 \end{bmatrix} ; [\varepsilon_c^p] = \begin{bmatrix} \varepsilon_{cx}^p \\ \varepsilon_{cy}^p \\ \gamma_{cxy}^p \end{bmatrix} ; [\varepsilon_c^s] = \begin{bmatrix} \varepsilon_x^s \\ \varepsilon_y^s \\ \gamma_{xy}^s \end{bmatrix} \quad \textbf{(4-41)}$$

Where ε_c^o represents the elastic concrete strain offset and ε_c^p expresses the plastic concrete strain offset. Similarly, the strain offset components for the reinforcement are provided below:

$$[\varepsilon_s^o]_i = \begin{bmatrix} \varepsilon_{si}^o . \frac{1+\cos 2\alpha_i}{2} \\ \varepsilon_{si}^o . \frac{1-\cos 2\alpha_i}{2} \\ \varepsilon_{si}^o . \sin 2\alpha_i \end{bmatrix} ; [\varepsilon_s^p]_i = \begin{bmatrix} \varepsilon_{si}^p . \frac{1+\cos 2\alpha_i}{2} \\ \varepsilon_{si}^p . \frac{1-\cos 2\alpha_i}{2} \\ \varepsilon_{si}^p . \sin 2\alpha_i \end{bmatrix} \quad \textbf{(4-42)}$$

Where α_i is the angle of each reinforcement component relative to the x-axis. The strain components described lead to free nodal displacements that, in turn, are used to establish the pseudo nodal loads. The peusdo nodal loads are combined with the external loads to provide the total nodal forces.

The global stiffness matrix [*K*] of the entire structure is the summation of the element stiffness matrices. The nodal displacements are calculated through the global stiffness matrix and the applied force matrix:

$$[F] = [K][r] \quad \textbf{(4-43)}$$

Thereafter, the element strains (ε) are determined using the nodal displacements and the strain-displacement matrix [B]. Further details of the finite element formulation can be found elsewhere (Wong et al., 2000) and are out of the scop of this research.

4.5 Analysis Models

Program VecTor2 has been expanded through numerous developments to model salient characteristics of material behaviour including lateral expansion of concrete, triaxial stresses, and bond-slip to name a few. In addition, modelling of cyclically loaded structures, and consideration to the sequence of construction and loading chronology is possible. More recently, dynamic analysis of reinforced concrete structures is possible. Among the various models, cyclic loading and bond-slip will be discussed in further detail as they are more relevant to the current research.

4.5.1 Analysis of Cyclically Loaded Structures

In the development of the MCFT, strain history was not considered in determining the stress-strain response of the concrete and the reinforcement. The original constitutive relationships were applicable to monotonic loading where one stress value corresponded to a single strain value. However, this approach was not valid for cyclic loading where the materials experience hysteresis in the stress-strain response. The formulations of the MCFT/DSFM were modified to consider explicitly plastic offset strains and strain envelopes in consideration of the hysteretic response under cyclic loading. The constitutive relations for monotonic loading are based on the strains that correspond to the principal net

concrete strains. Under cyclic loading, the directions rotate as the load is reversed. Mohr's circle is used to record the strains for the changing rotation of the axes and transforms them to the global directions. The following formulations for concrete relate the plastic strain of concrete in the x, y-axes to plastic strains concerning principal directions:

$$\varepsilon_{c1}^{p} = \frac{\varepsilon_{cx}^{p} + \varepsilon_{cy}^{p}}{2} + \frac{\varepsilon_{cx}^{p} - \varepsilon_{cy}^{p}}{2} \cdot \cos 2\theta + \gamma_{cx}^{p} \cdot \sin 2\theta \quad \textbf{(4-44)}$$

$$\varepsilon_{c2}^{p} = \frac{\varepsilon_{cx}^{p} + \varepsilon_{cy}^{p}}{2} - \frac{\varepsilon_{cx}^{p} - \varepsilon_{cy}^{p}}{2} \cdot \cos 2\theta - \gamma_{cx}^{p} \cdot \sin 2\theta \quad \textbf{(4-45)}$$

The plastic strains change for a given load step by $\Delta\varepsilon_{c1}^{p}$ and $\Delta\varepsilon_{c2}^{p}$. The following is used to transform the plastic strain increments from the principal 1, 2 directions to the x, y axes, after which they are added to the previous plastic strains:

$$\varepsilon_{cx}^{p\,\prime} = \varepsilon_{cx}^{p} + \frac{\Delta\varepsilon_{c1}^{p}}{2} \cdot (1 + \cos 2\theta) + \frac{\Delta\varepsilon_{c2}^{p}}{2} \cdot (1 - \cos 2\theta) \quad \textbf{(4-46)}$$

$$\varepsilon_{cy}^{p\,\prime} = \varepsilon_{cy}^{p} + \frac{\Delta\varepsilon_{c2}^{p}}{2} \cdot (1 - \cos 2\theta) + \frac{\Delta\varepsilon_{c2}^{p}}{2} \cdot (1 + \cos 2\theta) \quad \textbf{(4-47)}$$

$$\gamma_{cxy}^{p\,\prime} = \gamma_{cxy}^{p} + \Delta\varepsilon_{c1}^{p} \cdot \sin 2\theta - \Delta\varepsilon_{c2}^{p} \cdot \sin 2\theta \quad \textbf{(4-48)}$$

The strain envelopes are defined by the maximum compressive strains ($\varepsilon_{cmx}, \varepsilon_{cmy}, \gamma_{cmxy}$), and similarly the maximum tensile strains. These maximum strains are transformed to principal axes based on Mohr's Circle:

$$\varepsilon_{cm1} = \frac{\varepsilon_{cmx} + \varepsilon_{cmy}}{2} + \frac{\varepsilon_{cmx} - \varepsilon_{cmy}}{2} \cdot \cos 2\theta + \gamma_{cmx} \cdot \sin 2\theta \quad \textbf{(4-49)}$$

$$\varepsilon_{cm2} = \frac{\varepsilon_{cmx} + \varepsilon_{cmy}}{2} - \frac{\varepsilon_{cmx} - \varepsilon_{cmy}}{2} \cdot \cos 2\theta - \gamma_{cmx} \cdot \sin 2\theta \quad \textbf{(4-50)}$$

For each load step, ε_{c1} and ε_{c2} define the principal net concrete strains. These strains are then referred to update the maximum strains. For example, if ε_{c1} is greater than ε_{cm1}, $\Delta\varepsilon_{cm1}$ is set to 0. Otherwise, the difference between these two strain values is set as the increment maximum strain. A similar procedure is used for the principal 2 direction. The maximum strains are then updated using the changes in the incremental maximum strain as follows:

$$\varepsilon_{cmx}{}' = \varepsilon_{cmx} + \frac{\Delta\varepsilon_{cm1}}{2} \cdot (1 + \cos 2\theta) + \frac{\Delta\varepsilon_{cm2}}{2} \cdot (1 - \cos 2\theta) \quad \textbf{(4-51)}$$

$$\varepsilon_{cmy}{}' = \varepsilon_{cmy} + \frac{\Delta\varepsilon_{cm1}}{2} \cdot (1 - \cos 2\theta) + \frac{\Delta\varepsilon_{cm2}}{2} \cdot (1 + \cos 2\theta) \quad \textbf{(4-52)}$$

$$\gamma_{cmx}{}' = \gamma_{cmx} + \Delta\varepsilon_{cm1} \cdot \sin 2\theta - \Delta\varepsilon_{cm2} \cdot \sin 2\theta \quad \textbf{(4-53)}$$

After calculating the strain envelopes and plastic strains, VecTor2 can resolve the hysteretic response for the concrete. The same strategy has been implemented for reinforcement.

4.5.2 Bond Mechanism

In a reinforced concrete structure, the stresses are resisted by the concrete and reinforcement simultaneously. The stress transfer between the concrete and reinforcement to form a composite structure occurs due to bond action between the two materials. The bond stresses develop through a mechanical interlock with the concrete, chemical adhesion and friction in the case of embedded reinforcement. Bond action near cracks is critical, where the level of bond stresses increases. Perfect bonding can be assumed with confidence where the bond stresses are low. In such a situation, the change in reinforcement strain is equal to the change in the total concrete strain. Conversely, assuming imperfect bonding is more appropriate at locations of higher bond stress. Imperfect bonding refers to a strain differential between the concrete and the reinforcement due to slip.

Under normal loading conditions, such as monotonic loading, well-designed structures following modern building codes are not expected to be controlled by failure due to bond issues. The MCFT was developed assuming perfect bond, and for monotonic loading of well-detailed structures, this is acceptable. Structures that are vulnerable to bond failure are best modelled considering bond-slip that modifies the internal stress distribution between the concrete and reinforcement and load-deformation response. Specifically,

cyclically loaded structures experience continual degradation of the concrete that, in turn, affects the bond and the hysteretic response.

Program VecTor2 models bond slip through bond-link or contact elements and its constitutive bond-slip models. The bond element is deformable (similar to a spring) that links the concrete and reinforcement elements. The element removes the perfect bond condition. The response of the bond element is based on the bond-slip response curve which relies on the confining pressure in the concrete, the reinforcement layout, and material properties.

4.6 Models for Concrete Material

Program VecTor2 houses a suite of concrete material models. Typically, the default constitutive models are selected for analysis. Within the concrete material models, the stresses are calculated from the strains at each load step based on constitutive relationships. VecTor2 employs constitutive relations that are Cauchy-type models, which describe the concrete response through nonlinear functions of stress and strain. These relationships are derived from standard specimens rather than from the materials.

Constitutive models are available to capture: the compressive stress-strain response of concrete, including compression pre-peak response, compression post-peak response, and compression softening; the tension response, including tension softening; the hysteretic response; and other physical and mechanical properties of concrete. The description of the models that follow are those that were selected to conduct the analyses in this research. Detailed explanations for other models are available elsewhere (Wong et al., 2000).

4.6.1 Compression Pre-Peak Response

The stress-strain response of concrete in compression is non-linear, particularly at higher compressive stresses. Although cement and aggregates exhibit a separately linear response, the composite material provides nonlinearity.

The compression pre-peak response models calculate the principal compressive stress (f_{ci}) if the compressive principal strain (ε_{ci}) is less than the strain (ε_p) corresponding to the peak compressive strength (f_p). The default pre-peak model is the Hognestad (Parabola) model. It is suitable for modelling of normal strength concrete with a strength less than 40 MPa. Figure 4-7 illustrates the pre- and post-peak concrete compression response based on the Hognestad model.

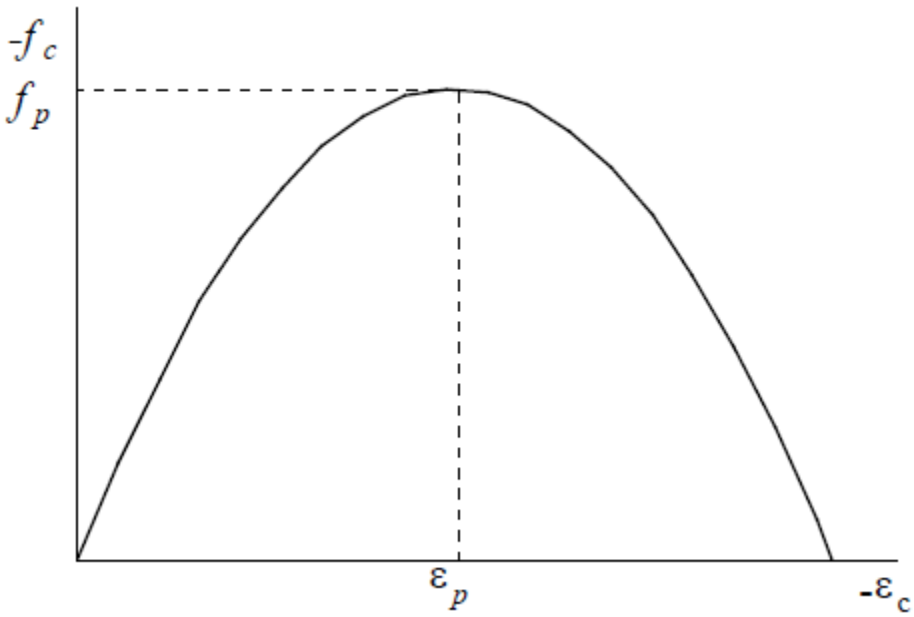

Figure 4-7 Hognestad pre-peak and post-peak compression response (Wong et al., 2000)

The stress-strain curve is defined by the following expression:

$$f_{ci} = -f_p \left(2\left(\frac{\varepsilon_{ci}}{\varepsilon_p}\right) - \left(\frac{\varepsilon_{ci}}{\varepsilon_p}\right)^2 \right) < 0 \qquad for\ \varepsilon_{ci} < 0 \tag{4-54}$$

As illustrated in Figure 4-7, the stress-strain relationship is symmetric about the strain ε_p. The initial tangent stiffness of concrete (E_c) is defined as follows:

$$E_c = 2\left(\frac{f_p}{|\varepsilon_p|}\right) \tag{4-55}$$

Where f_p and ε_p are peak concrete compressive stress and the corresponding strain.

4.6.2 Compression Post-Peak Response

The compression post-peak models are utilized beyond the peak compressive strength (f_p) and corresponding strain (ε_p). These models calculate the principal compressive strength (f_{ci}) if the principal strain (ε_{ci}) exceeds the strain corresponding to the peak compressive strength. The peak compressive stress and corresponding strain are modified from the unconfined uniaxial concrete compressive strength (f_c') and corresponding strain (ε_0), respectively, for compression softening effects due to co-existing transverse tensile strains and strength gain due to confinement (Wong et al., 2000). For confined concrete, the Modified Park-Kent, Popovic/Mander, Hoshikama et al., and Saenz models are available. The Modified Park-Kent (default model) was used in the analyses and is further described. The Modified Park-Kent model considers the improvement in concrete strength and ductility due to confinement. The stress-strain curve for the post-peak concrete compression response following the Modified Park-Kent model is shown in Figure 4-8.

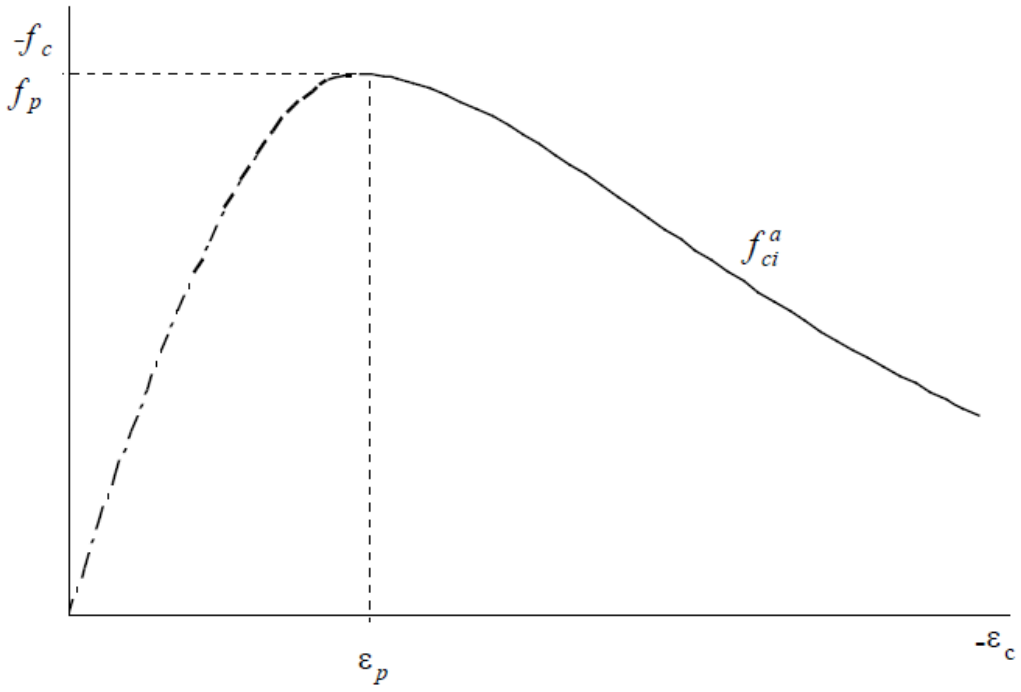

Figure 4-8 Modified Park-Kent post-peak concrete compression response (Wong et al., 2000)

The post-peak compression stress (f_{ci}) is calculated according to the following:

$$f_{ci} = (1 - c)f_{ci}^{a} + c.f_{ci}^{b} \quad \textbf{(4-56)}$$

Where f_{ci}^{b} represents the stress for confined concrete and f_{ci}^{a} is the stress for unconfined concrete. Where:

$$c = 4\left(\frac{f_p - f_c'}{f_c'}\right) \qquad 0 \le c \le 1 \quad \textbf{(4-57)}$$

The parameter c increases from zero to one when f_p increases from f'_c to 25% above f'_c. This parameter provides a linear transition from the unconfined to the confined compression post-peak response. f_{ci}^{a} is calculated as follows:

$$f_{ci}^{a} = -f_p\left(\frac{\varepsilon_{ci}}{\varepsilon_p}\right).\exp\left(1-\left(\frac{\varepsilon_{ci}}{\varepsilon_p}\right)\right) \quad \textbf{(4-58)}$$

Also, the post-peak response is assumed to have a sustaining stress level of $0.2f_p$ when $f_p > f_c'$

4.6.3 Compression Softening

Concrete cracking plays a critical role in the compressive strength of concrete through the phenomena known as compression softening. Substantially, the presence of transverse tensile straining reduces the compressive strength and ductility.

Compression softening is defined by the parameter β_d and varies from zero to one. A β_d value corresponding to one indicates the absence of compression softening. The default Vecchio 1992-A model was selected for the analyses. The basis of this model is a statistical analysis of the response of numerous panels tested at the University of Toronto (B. F. J. Vecchio, 1993). The compression softening model is classified by two types: strength- and strain-softened, and strength-only softened. Strength- and strain-softened models uses β_d as a function of the principal tensile strain to compressive strain to reduce the compressive strength (f_c') and the corresponding strain, ε_0, to determine the peak compressive strength f_p and corresponding strain ε_p. The strength-only softened model applies β_d to reduce the compressive strength only. Figure 4-9 and Figure 4-10 illustrate the strength- and strain-softened and strength-only softened models, respectively.

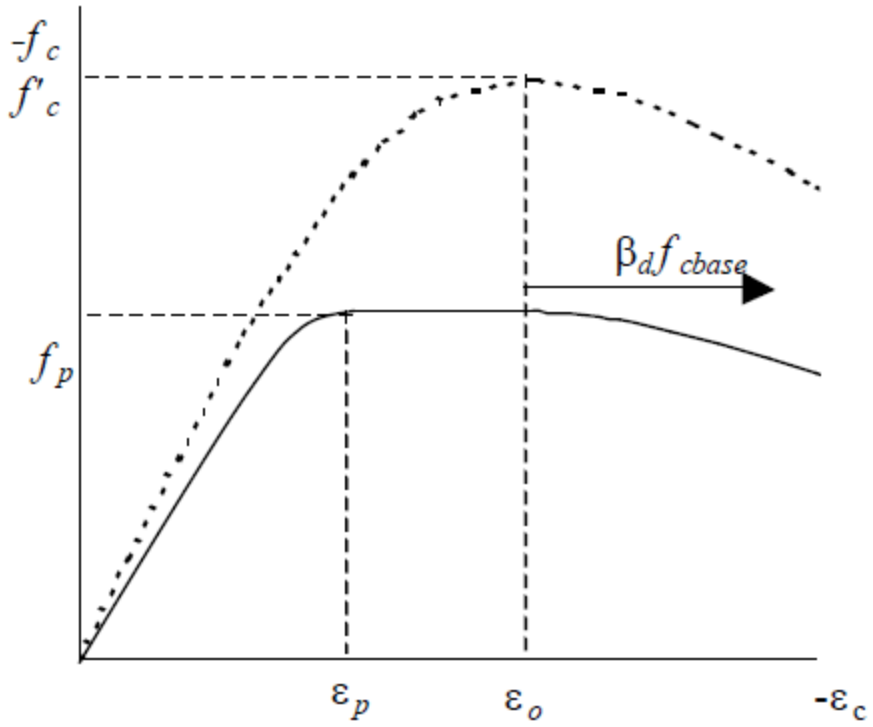

Figure 4-9 Strength- and strain-softened compression stress-strain response (Wong et al., 2000)

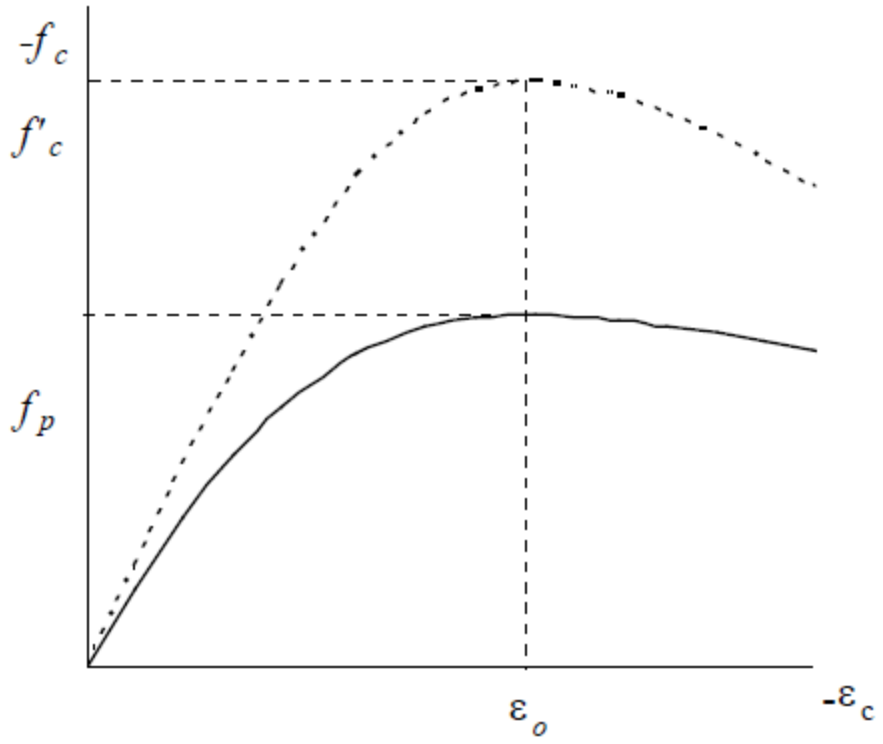

Figure 4-10 Strength-only softened compression stress-strain response (Wong et al., 2000)

The Vecchio 1992-A model is the strength- and strain-softened model. The factor C_s is proposed in the formulation to consider the effect of shear slip. The formulation developed to calculate β_d (compression softening reduction factor) follows:

$$\beta_d = \frac{1}{1 + C_s . C_d} \leq 1 \qquad \textbf{(4-59)}$$

$$C_d = \begin{cases} 0 & if\ r < 0.28 \\ 0.35(r - 0.28)^{0.80} & if\ r > 0.28 \end{cases} \qquad \textbf{(4-60)}$$

Where *r* is the ratio of the principal tensile strain to the principal compressive strain:

$$r = \frac{-\varepsilon_{c1}}{\varepsilon_{c2}} \leq 400 \quad \textbf{(4-61)}$$

The upper value of 400 is intended to limit the softening effect when the principal tensile strain is large such that the reinforcement has yielded. The C_s factor is used in compression softening to account for the effects of shear slip. In Equation 4-59, C_s = 0.55 where shear slip is assumed; otherwise C_s is set to 1. The peak compressive strength and similarly the corresponding strain are modified as follows:

$$f_p = \beta_d f_c' \quad \textbf{(4-62)}$$

Figure 4-11 illustrates the variation of compression softening based on the Vecchio 1992-A model.

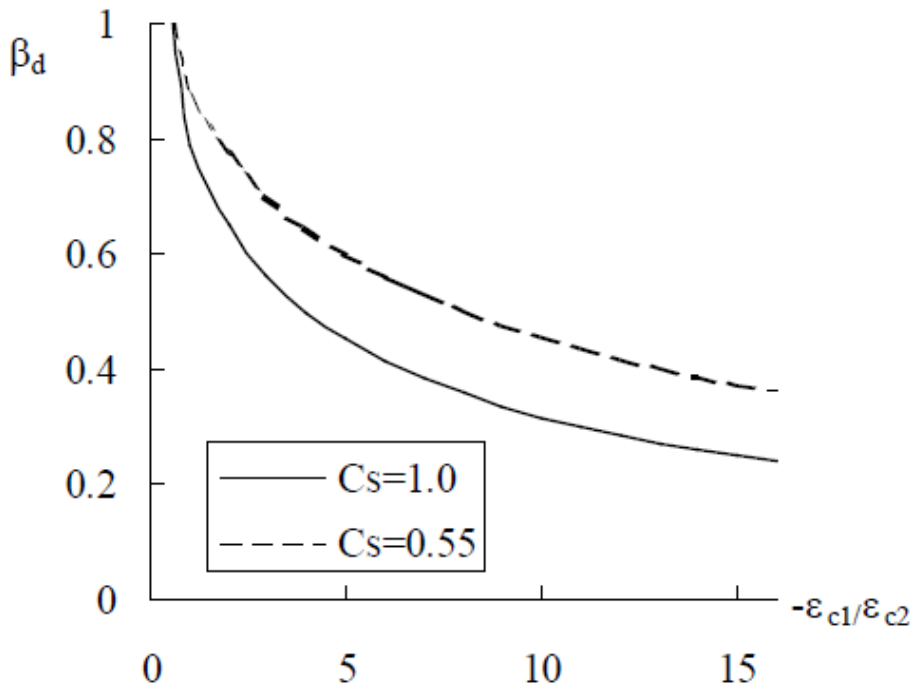

Figure 4-11 Vecchio 1992-A compression softening model (Wong et al., 2000)

4.6.4 Tension Stiffening

Concrete is a brittle material when subjected to tensile stresses. Before cracking, the behaviour of concrete is linear elastic. Beyond cracking, the tensile stresses drop to zero at the location of the crack. However, between cracks, concrete develops tensile stresses due to the bond between the reinforcement and the concrete. This phenomenon is referred to as tension stiffening, which aids to stiffen the structure more than the reinforcement alone. Figure 4-12 illustrates the influence of tension stiffening.

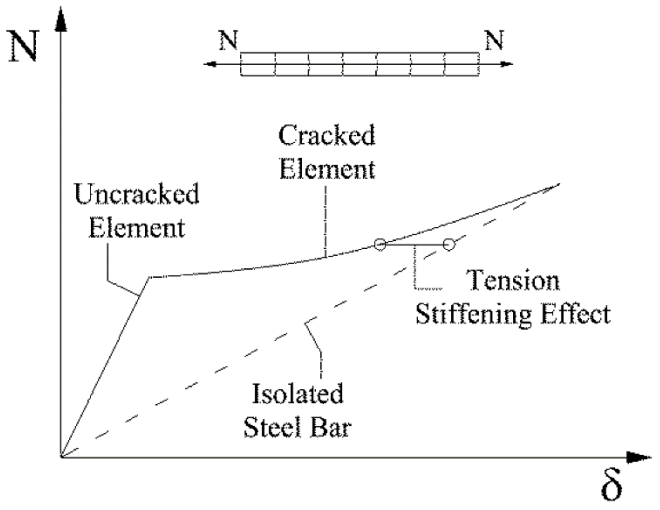

Figure 4-12 Effect of the tension stiffening (Allam, Shoukry, Rashad, & Hassan, 2013)

If tension stiffening is neglected, the reinforcement is assumed to carry all the tensile stresses at and between cracks. In VecTor2, the area of concrete that develops tension stiffening is defined (bounded) by 7.5 times the diameter of the reinforcing bar. The post-cracking tensile strength of concrete (f_{c1}) is the maximum of tension stiffening effects

(f_{c1}^{a}) and tension softening (f_{c1}^{b}). Tension softening tends to control in situations with little to no reinforcement.

The default Modified Bentz 2003 model was selected in the analyses to capture tension stiffening. The model considers the influence of reinforcement ratio and bond characteristics. The tensile stresses due to tension-stiffening for cracked concrete are calculated with the following formulation:

$$f_{c1} = \frac{f_t'}{1 + \sqrt{c_t \varepsilon_{c1}}} \qquad for\ \varepsilon_{c1} > \varepsilon_t' \tag{4-63}$$

Where f_t' is the concrete cracking strength and ε_t' is the concrete cracking strain. The c_t factor is the tension stiffening coefficient and is calculated as follows:

$$c_t = 3.6\ t_d . m \tag{4-64}$$

Where $t_d = 0.6$ and m is:

$$\frac{1}{m} = \sum_{i=1}^{n} \frac{4\rho_i}{d_{bi}} .\ |\cos(\theta - \alpha_i)| \tag{4-65}$$

Where ρ_i is the reinforcement ratio, d_{bi} is the reinforcement bar diameter, θ is the orientation of the principal direction, and α_i is the orientation of the reinforcement with respect to the x-axis.

4.6.5 Tension Softening

The tension softening phenomenon is based on the development of post-cracking tensile stress in plain concrete given that concrete is not a perfectly brittle material. As the crack

widens, the tensile stresses in the concrete in the area of the crack are gradually reduced to zero. Tension softening is an important phenomenon in lightly reinforced concrete structures. The inclusion of tension softening leads to a more accurate load-deformation response. Also, the descending portion of the post-cracking stress-strain response captures better the ductility. In VecTor2, the average tension softening stress is denoted by f_{c1}^{b}. The larger of tension softening and tension stiffening controls the post-cracking stress for the concrete. The Bilinear model (default) in VecTor2 was chosen for all analyses. The calculation of f_{c1} considering the effect of tension softening follows:

$$f_{c1} = \begin{cases} f_{cr}\left(1 - 0.8\left(\dfrac{\varepsilon_{c1} - \varepsilon_{cr}}{\varepsilon_{ch3} - \varepsilon_{cr}}\right)\right) & when\ \varepsilon_{c1} < \varepsilon_{ch3} \\ 0.2 f_{cr}\left(1 - \left(\dfrac{\varepsilon_{c1} - \varepsilon_{ch3}}{\varepsilon_{ch4} - \varepsilon_{ch3}}\right)\right) & when\ \varepsilon_{ch3} \le \varepsilon_{c1} < \varepsilon_{ch4} \end{cases} \quad \textbf{(4-66)}$$

Where:

$$\varepsilon_{ch3} = 0.64\varepsilon_{ch} + \varepsilon_{cr} \quad \textbf{(4-67)}$$

$$\varepsilon_{ch4} = 6.8\varepsilon_{ch} + \varepsilon_{cr} \quad \textbf{(4-68)}$$

ε_{ch} is the characteristic strain for concrete in tension. Bazant (2002) suggested a factor to quantify the resistance of concrete to cracking. The factor is known as G_f, which is the fracture energy factor. It is the energy required to form a complete crack. The characteristic strain is calculated from the following and includes the fracture energy:

$$\varepsilon_{ch} = \frac{G_f}{L_{ref}.\varepsilon_{cr}} \quad \textbf{(4-69)}$$

Where L_{ref} is characteristic length and ε_{cr} is the concrete cracking strain.

Several other constitutive models are available to capture different physical phenomena in the concrete. These include confining strength, dilation, cracking criterion, crack shear slip, to name a few. For all analyses presented herein, the default models have been selected. Constitutive models are also available for reinforcement. These models consider the hysteretic response of reinforcement, dowel action, and buckling. The following sections provide further details of the reinforcement models.

4.7 Models for Reinforcement

In this section, the constitutive and behavioural models for reinforcement are described. The monotonic and hysteretic stress-strain responses of reinforcement are followed by models for dowel action and buckling.

Program VecTor2 requires input regarding the type of reinforcement (prestressed steel, tension-only reinforcement, ductile steel reinforcement, compression-only reinforcement, external skin plate, etc.) to ensure the proper material properties are provided for the constitutive models. The main reinforcement modelled in the analyses was ductile steel reinforcement.

The stress-strain response for ductile steel reinforcement contains there phases: 1) initial linear elastic region; 2) yielding; and 3) linear or nonlinear strain hardening. The monotonic stress-strain response defines the backbone for the hysteretic response. Figure 4-13

illustrates the ductile steel stress-strain response with either linear or non-linear strain hardening.

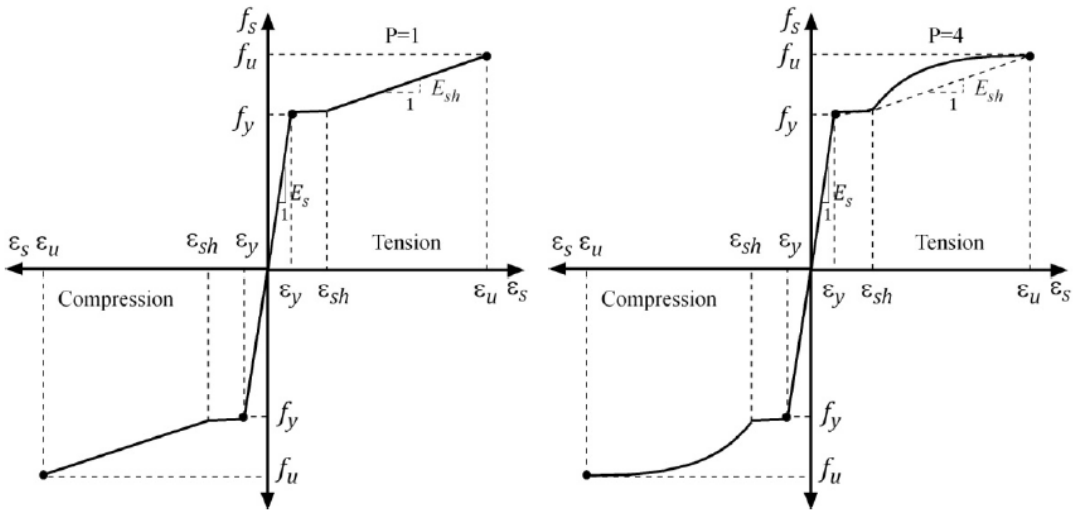

Figure 4-13 Ductile steel stress-strain response with linear strain hardening (Left) and non-linear strain hardening (Right) (Wong et al., 2000)

The default model in VecTor2 considers non-linear strain hardening. As shown in Figure 4-13, E_{sh} is the strain hardening modulus and is calculated from the following:

$$E_{sh} = \frac{f_u - f_y}{\varepsilon_u - \varepsilon_{sh}} \quad \textbf{(4-70)}$$

VecTor2 houses options for tension-only or compression-only reinforcement. In tension-only reinforcement, the strain-stress curve is similar to the ductile steel reinforcement model, and the compression stress is set to zero. This model is more suitable for FRP-type reinforcement which does not provide resistance in compression. In compression-only reinforcement, the ductile steel reinforcement compression response is used, and the tensile stress is zero.

Several models are available for the hysteretic response of reinforcement and dowel action and buckling. In the following section, the hysteretic model for reinforcement utilized in the analyses is described along with dowel action. Three different models have been proposed in VecTor2 to capture reinforcement buckling: Dhakal-Maekawa 2002 (DM), Refined-Maekawa Model (RDM) and Asatusu Model. The default model in VecTor2 is RDM. Further information about the buckling model is available elsewhere (Wong et al., 2000).

4.7.1 Hysteretic Response (Seckin Model)

The hysteretic response simulates the response of the reinforcement during unloading and reloading. The backbone curve follows the monotonic stress-strain response. The hysteretic response (unloading/reloading) can be simulated with a linear model considering no plastic offset strain as the basic model. The model developed by Seckin (1981) that includes the Bauschinger effect as shown in Figure 4-14 was used in the analyses and is the default model in VecTor2. With the Bauschinger effect, the reinforcement exhibits early yielding upon load reversal after plastic straining due to stress changes at the microscopic level (Wong et al., 2000).

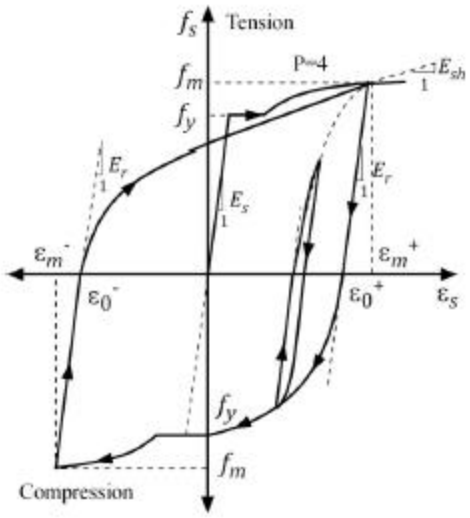

Figure 4-14 Seckin hysteretic response model with Bauschinger effect for steel reinforcement (Wong et al., 2000)

Reloading to a strain ε_j follows a nonlinear path and includes the Bauschinger effect. The stress on this reloading branch is calculated as follows:

$$f_s = E_r(\varepsilon_j - \varepsilon_0) + \frac{E_m - E_r}{N(\varepsilon_m - \varepsilon_0)^{N-1}}(\varepsilon_j - \varepsilon_0)^N \quad \textbf{(4-71)}$$

Where *N* is:

$$N = \frac{(E_m - E_r)(\varepsilon_m - \varepsilon_0)}{f_m - E_r(\varepsilon_m - \varepsilon_0)} \quad \textbf{(4-72)}$$

The unloading modulus, E_r, is determined from the following formulations:

$$E_r = \begin{cases} E_s & for\ (\varepsilon_m - \varepsilon_0) \le \varepsilon_y \\ E_s\left(1.05 - 0.05\dfrac{(\varepsilon_m - \varepsilon_0)}{\varepsilon_y}\right) & for\ \varepsilon_y < (\varepsilon_m - \varepsilon_0) < 4\varepsilon_y \\ E_s & for\ 4\,\varepsilon_y \le (\varepsilon_m - \varepsilon_0) \end{cases} \quad \textbf{(4-73)}$$

Where ε_0 is the plastic offset strain in the cycle, ε_y is the yield strain, ε_m is the maximum strain during the last cycle with f_m the corresponding stress and E_m the corresponding tangent stiffness, and E_s is the elastic modulus. During unloading, the response is linear and the reinforcement stress is calculated as follows:

$$f_s = f_{s_j-1} + E_r(\varepsilon_j - \varepsilon_{j-1}) \quad \textbf{(4-74)}$$

4.7.2 Dowel Action

The dowel model incorporates the resistance of reinforcement crossing a crack. The shear resistance due to the dowel action is denoted as v_d and is calculated based on shear-slip resistance δ_s. This shear resistance from dowel action is subtracted from the local shear stress on the crack and, thus, reduces the amount of shear slip.

The Tassios model for dowel action is based on an elastic-plastic force-displacement relationship. In this model, the crack and reinforcement are assumed to be perpendicular as shown in Figure 4-15.

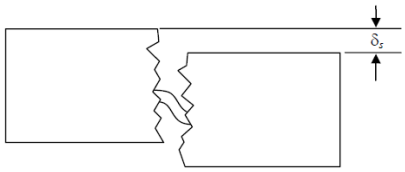

Figure 4-15 Dowel resistance assumption for the Tassios Model (Wong et al., 2000)

Two (2) Tassios dowel models are available in VecTor2: Tassios crack slip, which is the default option; and Tassios crack strength. The dowel force, V_d, is calculated as a function of the relative displacement of the crack, δ_s, as follows:

$$V_d = E_s I_z \lambda^3 \delta_s \leq V_{du} \quad \textbf{(4-75)}$$

Where V_{du} is the ultimate dowel force and it is calculated as follows:

$$V_{du} = 1.27 d_b^2 \sqrt{f_c' f_y} \quad \textbf{(4-76)}$$

Where d_b is the bar diameter, f_c' is the compressive strength of the concrete, and f_y is the yield strength of the reinforcement. I_z is the moment of inertia for the reinforcement and calculated as follows:

$$I_z = \frac{\pi d_b^4}{64} \quad \textbf{(4-77)}$$

λ is related to the ratio of the stiffness of the concrete to the stiffness of the reinforcement. The following formulation is used:

$$\lambda = \sqrt[4]{\frac{k_c d_b}{4 E_s I_z}} \quad \textbf{(4-78)}$$

Where k_c is the stiffness of the concrete and E_s is the elastic modulus of the reinforcement. The stiffness of the concrete is calculated with the following formulation:

$$I_z = \frac{127. c \sqrt{f_c'}}{d_b^{2/3}} \quad \textbf{(4-79)}$$

In this formulation, c is a coefficient that takes into account the bar spacing. The coefficient is set to 0.8.

4.8 Bond Models

This section describes the bond stress-slip models. Two different bond models are available in VecTor2: models for embedded bars (either smooth or deformed); and models for externally bonded reinforcement. These models are considered for both monotonic and cyclic responses. [Note that the hysteretic response is not discussed herein for brevity]. For embedded bars, the stress-slip response varies between confined and unconfined reinforcing bars. The mode of failure for confined bars is typically pull-out; whereas, for unconfined bars, the mode is splitting. The stress-slip relationship for both cases is defined based on the bond stresses (τ) and bond slips (Δ). The bond stress-slip model is defined by the confinement pressure factor (β) which interpolates between confined and unconfined bond stresses and slips. A confinement pressure for the confined bar is 7.5 MPa and 0 for unconfined cases. Based on the confinement pressure factor (β), the confining pressure (σ) is calculated as follows:

$$\beta = \frac{\sigma}{7.5} \qquad 0 \leq \beta \leq 1 \qquad \textbf{(4-80)}$$

The bond model incorporated in the analyses is based on the work of Eligehausen, which forms the default model in VecTor2. Figure 4-16 illustrates the difference in response between the confined and unconfined bond stress-slip responses.

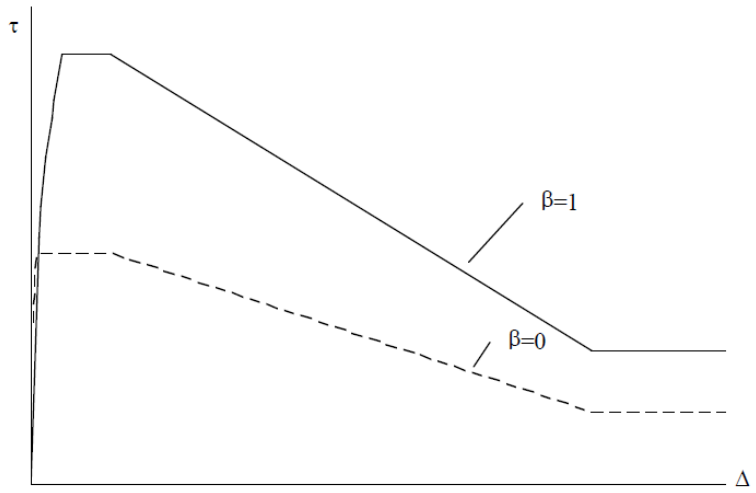

Figure 4-16 Eligehausen bonds stress-slip response (Wong et al., 2000)

The responses are characterized by an ascending linear component followed by a stress plateau (constant bond stress). After that, a linearly declining branch leads to constant residual stress. Further details of the bond model including the formulations are available in the VecTor2 manual (Wong et al., 2000).

Chapter 5 Preliminary Numerical Analysis

In this chapter, preliminary numerical analyses of the walls using the program VecTor2 are presented to evaluate the performance of the walls subjected to in-plane lateral loading. The preliminary assessment considers pushover analyses only of the wall models. Chapter 6 provides detailed analyses including pushover and reverse cyclic loading of the final wall design. The intent of this chapter is to determine the influence of various factors that might affect the performance of the wall. This includes: i) the aspect ratio of the wall panel; ii) smooth or deformed internal wire-mesh reinforcement; iii) size of the internal reinforcement; iv) bond characteristics between the internal reinforcement and the concrete; v) embedment length of the internal vertical reinforcement into the cap beam; vi) end anchorage (hooked versus non-hooked) of the internal reinforcement; and vii) contribution of the external light gauge steel.

5.1 Parametric Study Variables

5.1.1 Aspect Ratio

The first parameter investigated was the height to length ratio of the wall. Two different ratios were considered in consultation with Burnco based on practical applications for this wall system. One was a squat wall with a height of 3000 mm and length of 5000 mm, resulting in an aspect ratio of 0.6. The other was a squat/slender wall (referred to as slender herein) with a height of 3000 mm and a length of 1800 mm proving an aspect ratio of 1.67.

Burnco Manufacturing provided the preliminary design of the wall panels as currently built. The design and material characteristics are similar for both types of walls.

5.1.2 Reinforcement Surface Type

The surface of the internal reinforcing steel (smooth or deformed) is critical to the lateral performance of the wall. Smooth bars in reinforced concrete shear walls are problematic due to the significantly less bond capacity in comparison to deformed bars (Fabbrocino et al. 2005). The influence of smooth bars versus deformed bars is investigated for both the vertical and horizontal components of the internal wire-mesh reinforcement.

5.1.3 Reinforcement Size

Two different sizes (diameter) for the internal wire-mesh reinforcement were studied: 6 mm and 10 mm. The original and current diameter of the wire-mesh used in the wall is 6 mm.

5.1.4 Bond Characteristics

To investigate the full effects of the wire-mesh, the nature of the bonding between the concrete and the reinforcement is essential. To study this, models with perfect bonding and imperfect bonding were considered.

5.1.5 Embedment Length

The original embedment length for the vertical component of the wire-mesh reinforcement is 100 mm. The embedment length is altered to investigate the impact on the performance

of the panel to lateral loading. There is an opportunity to extend the embedment length of the vertical reinforcement into the top and bottom beams.

5.1.6 Anchorage

The effect of end anchorage (hooked versus not hooked) of the internal vertical and horizontal reinforcement in the concrete panel was investigated. The current design of the wall system does not implement hooked vertical or horizontal bars. Thus, consideration of the development length must be considered. Alternatively, hooking the vertical wire-mesh bars ensures that they are more effectively developed at the critical location at the base of the wall panel. The analysis results illustrate that anchorage of the vertical reinforcement was more effective than anchorage of the horizontal reinforcement at improving the lateral performance.

5.1.7 External Light Gauge Steel

One of the primary objectives of this research is to explicitly determine the contribution of the external light-gauge steel to the overall lateral resistance of the wall panels. Models have been created with and without the presence of the steel joists. Also, models considering different cross-sectional areas of the external steel have been investigated. The intent is to determine the contribution of the entire area and only that portion that is embedded into the concrete panel.

5.2 Prototype Wall

Figure 5-1 provides the design and material details of the current wall design. This prototype wall design was used in this study as the benchmark to which improvements, through the parametric study, were suggested.

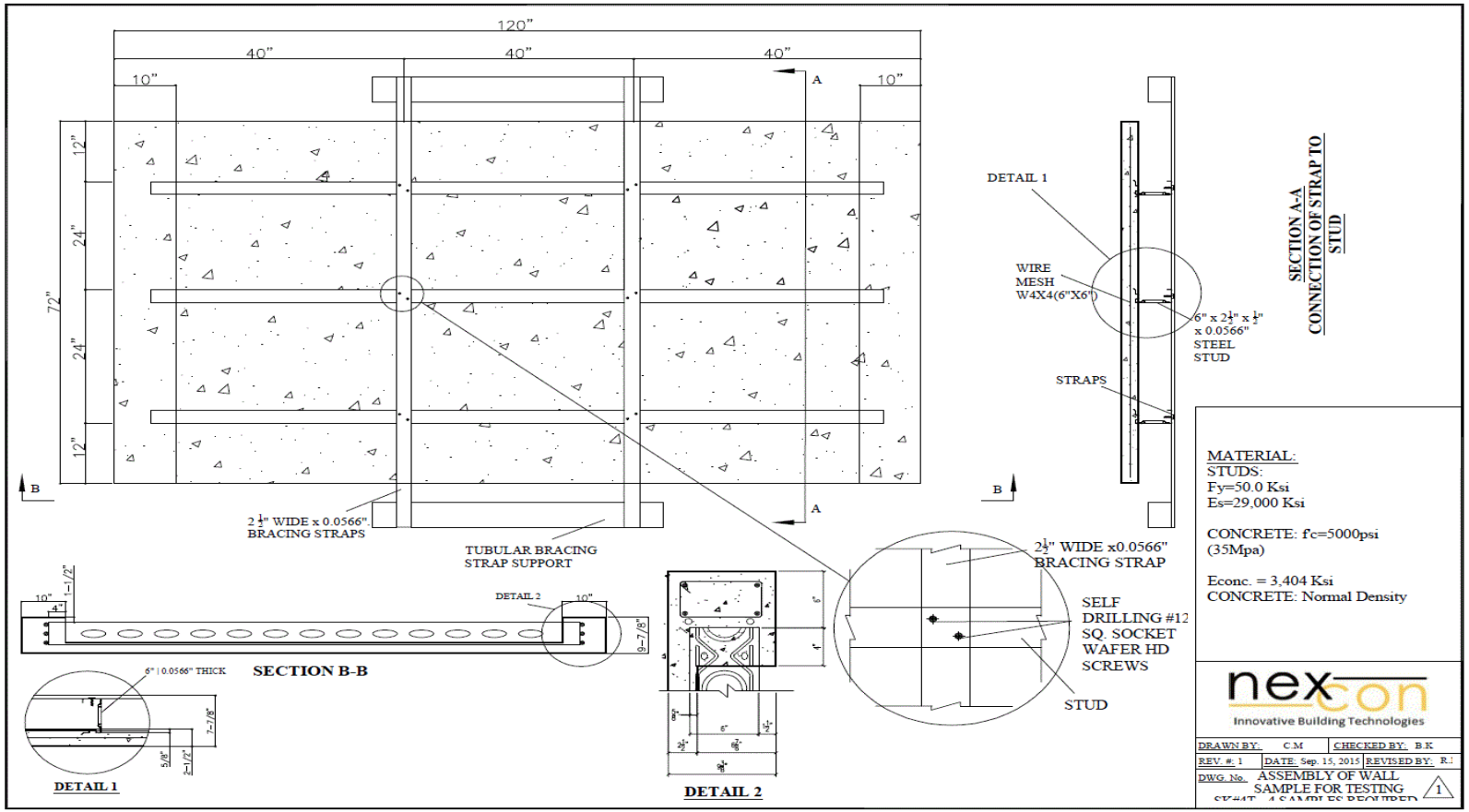

Figure 5-1 Prototype thin shell wall panel (Karimi, 2015a)

The drawing provides details for the prototype slender wall panel with height of 3000 mm and the length of 1800 mm. The exterior steel are located on one side of the concrete panel at a spacing of 600 mm. The flanges of the light-gauge steel are embedded into the concrete, approximately 133 mm^2 of cross-sectional area. Figure 5-2 provides a sectional detail of the external light gauge steel, the thin concrete panel, and the top cap beam.

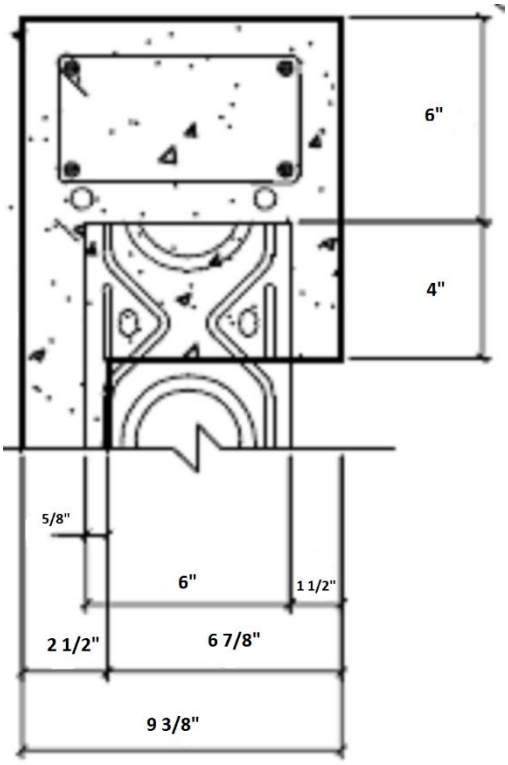

Figure 5-2 Typical detail at the top and bottom beam (Karimi, 2015a)

The base and cap beams have a square section, 250 mm in width and 250 mm in height. 4-15M bars are placed along the length of the beams in the longitudinal direction. The longitudinal reinforcement is confined by closed 10M stirrups spaced at 300 mm throughout. As illustrated in Figure 5-2, approximately 100 mm (4 inches) of each light-

gauge steel joist is embedded into the concrete of the cap and base beams. There is no interaction between the embedded portions of the exterior steel with the 4-15M longitudinal reinforcing bars. As shown in Figure 5-1, two horizontal bracing straps are used to connect the external steel. Figure 5-3 provides a detail of the connection between the bracing strap and external steel.

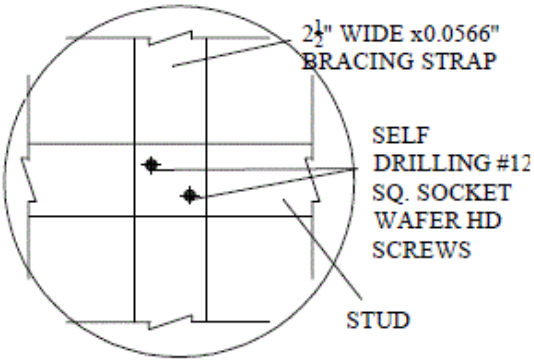

Figure 5-3 Bracing straps connection detail (Karimi, 2015a)

The bracing straps are 65 mm wide, 1.5 mm thick, and 1800 mm long. The straps are connected to the external steel with two self-drilling wafer headed screws. The horizontal straps are spaced vertically at 1000 mm. Figure 5-4 is a drawing of a typical external light-gauge steel joist with the thin concrete panel. The critical cross-sectional area is 385 mm^2. The critical cross-section area is the section with the perforation included. The thickness of the exterior steel is 1.4 mm, and the width is 73 mm. The external steel are perforated along the entire length.

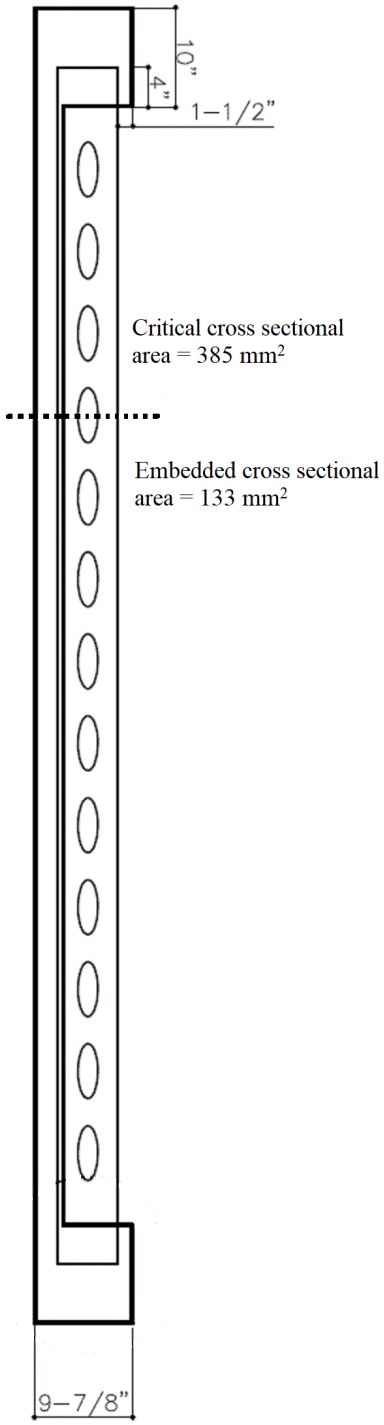

Figure 5-4 Cross section of the panel (Karimi, 2015a)

The 385 mm^2 cross-section area of the critical section is shown in Figure 5-5. This figure depicts a horizontal cut through the external light gauge steel at the location of the perforation. The lower flange of the steel is located away from the concrete panel, while the upper flange is embedded into the concrete. Figure 5-5 also provides the major sectional properties for the steel at this location. The ultimate tensile strength of the steel is reported as 448 MPa, and the yield strength is 358 MPa.

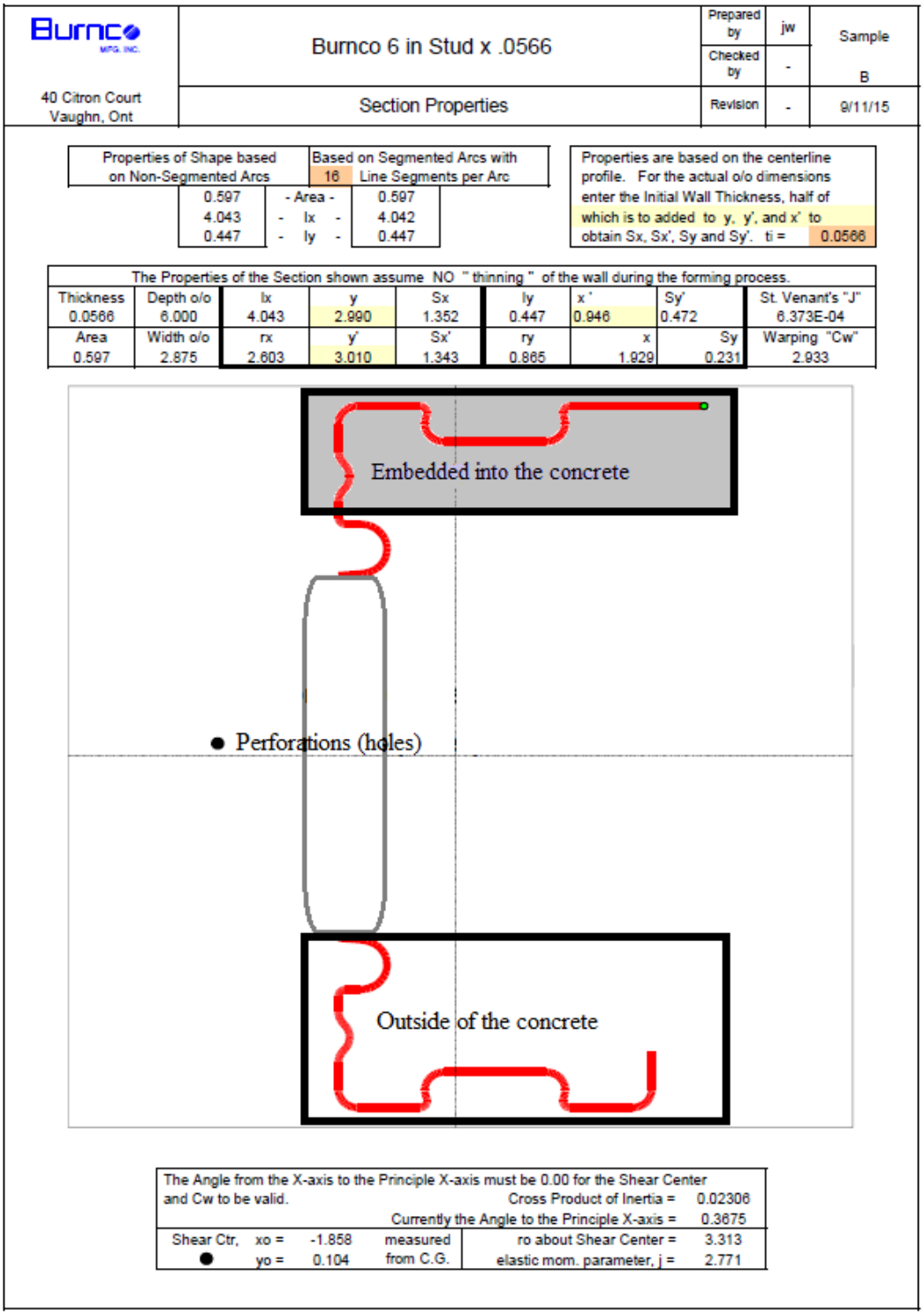

Figure 5-5 External steel section properties (Karimi, 2015b)

5.3 Finite Element Model

In this section, the analyses of the wall system using Program VecTor2 are presented. This section includes limitations in the modelling, the development of the finite element models, the definition of the material properties, selection of the constitutive models, and the results from the analyses.

5.3.1 Modeling Limitations

To simulate more realistically the wall system, a 3-D analysis should be considered. Although 3-D analysis increases the degrees of freedom and stiffness matrix, computational demand, and complexity of the geometry, it provides a more accurate representation, such as out-of-plane response. However, in this study, the 2-D software VecTor2 was employed. It was reasoned that the 2-D model could provide satisfactory simulations. Palermo and Vecchio (2007) illustrated that VecTor2 could simulate the responses of walls with 3-D effects, such as boundary elements, with sufficient accuracy. Furthermore, there is no experimental test data to compare and corroborate the numerical models developed in this study, and thus complex 3-D models were not warranted. Conversely, Program VecTor2 has been used to simulate the response of concrete walls in numerous studies (Palermo and Vecchio, 2004, Palermo and Vecchio, 2007; Cortes and Palermo, 2011; and Cortes and Palermo, 2012).

5.3.2 Structure Definition and Mesh Development

Two models were generated for analyses: a 5000 mm long by 3000 mm high wall panel; and an 1800 mm long by 3000 mm high panel. The former, with an aspect ratio of 0.6, is dominated by squat wall behaviour; while the later, with an aspect ratio of 1.67, illustrates a more flexural behavioural response. Figure 5-6 shows a typical connection of the wall panel at the base beam to the foundation. The connection uses ½ inch-diameter F1554 threaded rods of Grade 55 at 1200 mm spacing. The yield strength of the rods is reported to be 380 MPa, while the ultimate tensile strength is 655 MPa.

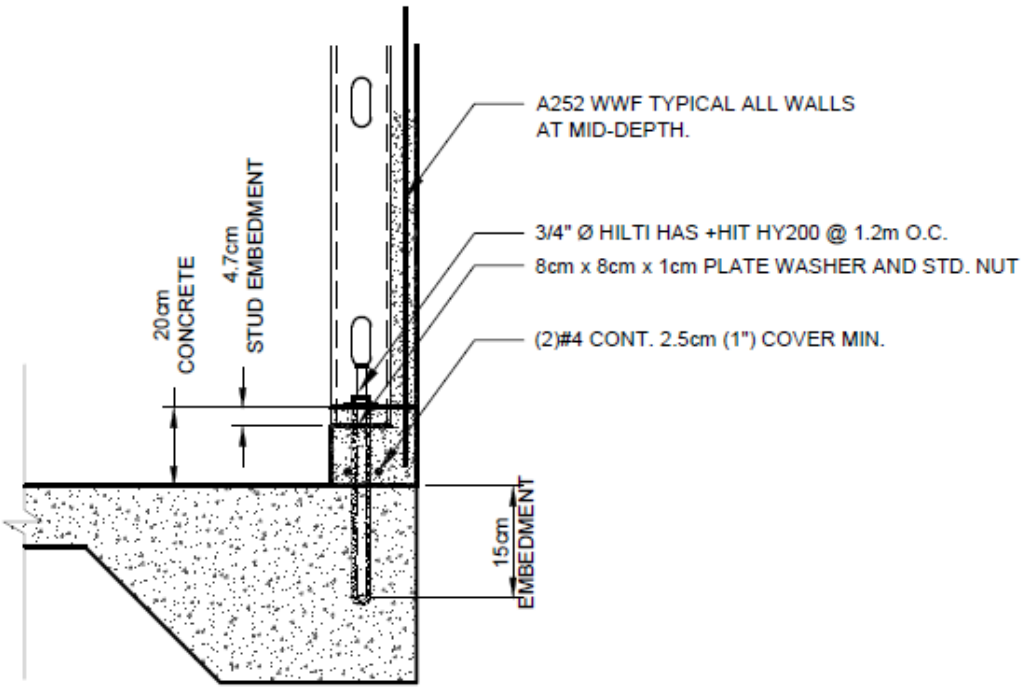

Figure 5-6 Typical connection for the wall panel (Tuck, 2014)

To simulate the base connection, vertical and horizontal restraints were implemented in the models along all the nodes of the finite element model along the base beam. Although the rods in the wall are spaced at 1200 mm, it was assumed that additional rods would be used to provide a greater degree of fixity to sustain the lateral loading. Note that the spacing of the rods in the current design is based on the wall panels sustaining out-of-plane loading only.

The 250 mm wide by 250 mm thick beams along the top and the base of the wall panel contain 4-15M longitudinal reinforcing bars with 10M stirrups at a spacing of 300 mm. The thickness of the beams and the concrete wall panel defined each section in the model. The longitudinal and stirrup reinforcements in the cap and base beams were smeared within the concrete elements in these regions of the model. To determine a smeared reinforcement quantity, the cross-sectional area of the reinforcement in each direction is required. To calculate the reinforcement area in horizontal direction (0° Direction), the cross-sectional area of the reinforcement parallel to x-axis was divided by the total cross-sectional area of the section (see Figure 5-7).

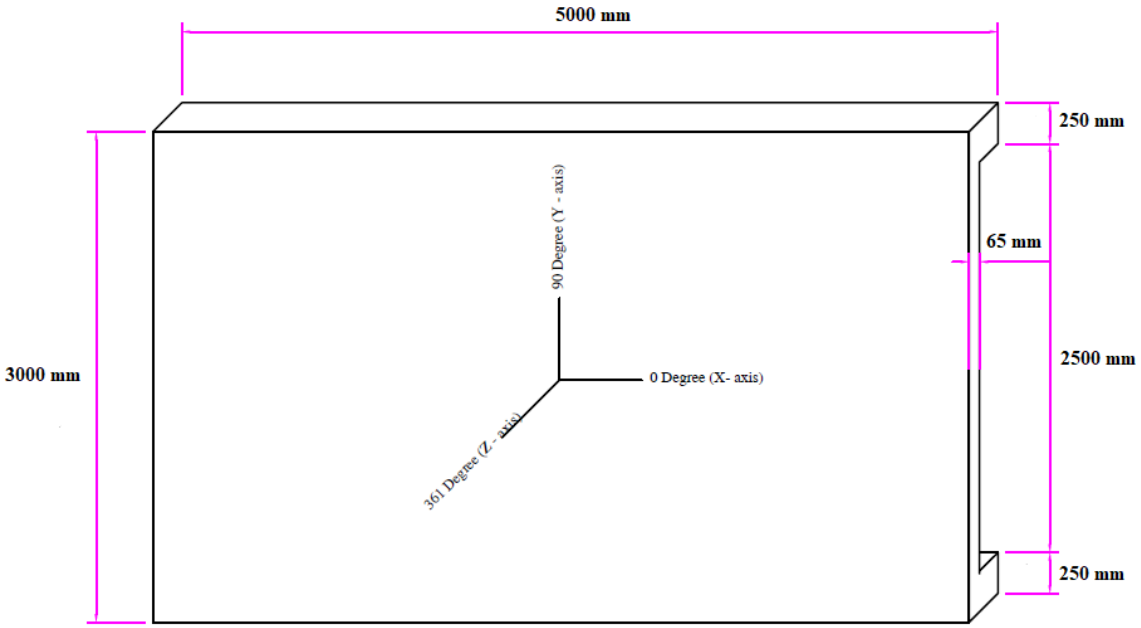

Figure 5-7 Dimensions and directions used in the finite element model

The cross-sectional area for each 15M bar located in the horizontal direction of the beams is 200 $\boldsymbol{mm^2}$, while the area of the 10M bars is 100 $\boldsymbol{mm^2}$. The cover plus the diameter of the stirrup is 65 mm from the edges. The reinforcement ratio in the 0-Degree-direction (x-axis or horizontal direction) is 1.28%. This is based on smearing the 4-15M bars over the beam cross section. The reinforcement ratio in the 90-Degree-direction (y-axis or vertical direction) is 0.267%. This is calculated from the two legs of stirrup running along the beams at 300 mm spacing. The reinforcement ratio in the out-of-plane direction or 361-Degree-direction (z-axis) is 0.267%. This stems from the two legs of the stirrups projecting

in the out-of-plane direction. The formula below was used to calculate the reinforcement ratio in each direction:

$$\rho = \frac{A_S}{A_g} \qquad \textbf{(5-1)}$$

Where A_S is the cross-sectional area of the steel reinforcement and A_g is a gross area of the concrete section over which the reinforcement projects. For example, in the vertical direction parallel to the y-axis (90 Degrees), the calculation was as follow:

$$\rho = \frac{A_S}{A_g} = \frac{2 \times 100\ mm^2}{300\ mm \times 250\ mm} \times 100 = 0.276\ \%$$

Figure 5-8 illustrates the cap and base beams referred to as Zones 1 and 3 in the development of the model, while the thin wall section was designated as Zone 2.

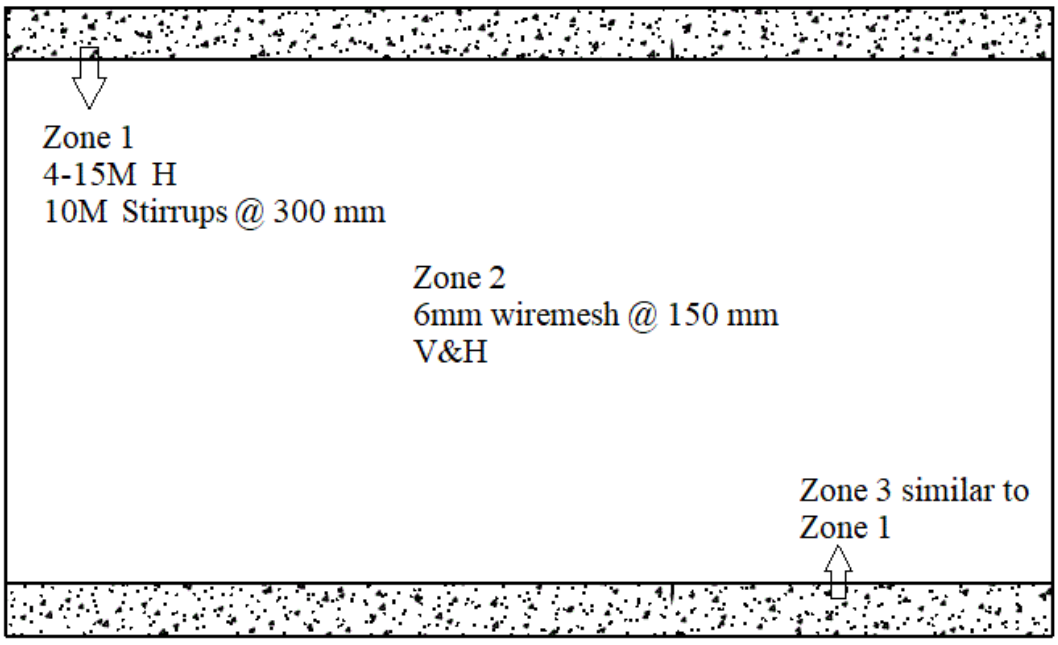

Figure 5-8 Wall panel zones defined for finite element model

In the web area (Zone 2), with a thickness of 65 mm, the single layer of 6 mm-diameter wire-mesh reinforcement was modelled with discrete truss bars at a spacing of 150 mm in vertical and horizontal directions. The truss bar is a 1-D element with two end nodes. The displacements and corresponding material strains are calculated along the axis of the element. Bond models can be assigned to the truss elements via a bond-link element to reflect the bond between the steel reinforcement and the concrete. The bond model cannot be assigned to the smeared reinforcement.

Two materials types were identified in the wall model. Material 1 includes the smeared reinforcement in the three directions for the cap and base beams, while Material 2 was set for the web area of the wall panel. Material 2 consisted of plain concrete elements without any smeared reinforcement. The reinforcement for the web area was defined through truss bars. The thickness of Material 1 is 250 mm and for Material 2 is 65 mm. The initial tangent elastic modulus (E_c) of the concrete is reported as 23 470 MPa which is a property used in the concrete material of the model. Canadian Standard Association suggests Equations (5-2) and (5-3) to calculate the tangent elastic modulus (Canadian Standards Association 2014). Equation (5-3) is suggested for normal strength concrete with compressive strength between 20 MPa to 40 MPa.

$$E_c = (3300\sqrt{\acute{f}_c} + 6900(\gamma_c/2300^{1.5}))\ MPa \quad \textbf{(5-2)}$$

$$E_c = 4500\sqrt{f'_c}\ MPa \quad \textbf{(5-3)}$$

For the analyses conducted in this research, the default option was selected. The default option replaces the 4500 coefficient in Equation 5-3 with 5500 to reflect a direct tension condition. The other mechanical properties of the concrete required during the analysis include the tensile strength of the concrete, the concrete strain at the peak compressive strength, Poisson's ratio, thermal expansion coefficient and density of the concrete. For these parameters, the default values were selected. The default value for Poisson's ratio (M_u) is 0.15. The default value for the thermal coefficient of expansion is $10 \times 10^6/°C$. The tensile strength of concrete (f'_t) is calculated from $f'_t = 0.33 \times \sqrt{f'_c}$ (Wong et al., 2000). The strain corresponding to f'_c is $\varepsilon_0 = 1.8 + 0.0075\, f'_c$ millistrain (Wong et al., 2000). The density of the concrete for normal density concrete is $2400\ \frac{kg}{m^3}$. The concrete material properties are the same for both Material 1 and Material 2. The mechanical properties of the reinforcement are based on reports provided by Burnco MFG. Other physical properties are listed in Tables 5-1 and 5-2.

The properties listed in Table 5-1 were used for the smeared material (Material 1) for the cap and base beams (Zone 1 and Zone 3). The concrete material for the thin panel does not include any smeared reinforcement. The welded wire-mesh in the web area is modelled with truss bars. The concrete properties of the thin panel are the same as Material 1, but the thickness of the section is 65 mm.

Table 5-1 Smeared reinforcement properties for cap and base beams

Reinforcement Diameter (D_b)	16 mm for 15M, 11.3 mm for 10M
Yield Strength (F_y)	410 MPa
Ultimate Strength (F_u)	600 MPa
Elastic Modulus (E_s)	200 000 MPa
Strain Hardening Strain (ε_{sh})	10 me
Ultimate Strain (ε_u)	150 me
Thermal Expansion Coefficient (C_s)	10×10^{-6} /°C

The properties for truss bars are defined separately. The parameters are similar to those required for the smeared reinforcement. The ductile reinforcement option was selected as the reference type for the reinforcement. The cross-sectional area of the wire-mesh is reported as $64mm^2$. Table 5-2 lists the mechanical properties of the wire-mesh that were assigned to the truss bars.

Table 5-2 Welded wire-mesh properties

Reinforcement Diameter (D_b)	6 mm bars
Yield Strength (F_y)	485 MPa
Ultimate Strength (F_u)	600 MPa
Elastic Modulus (E_s)	200000 MPa
Strain Hardening Strain (ε_{sh})	10 me
Ultimate Strain (ε_u)	150 me
Thermal Expansion Coefficient (C_s)	10×10^{-6} /°C

Based on the original design for the Thin Shell Panel (TSP), the exterior light-gauge steel are placed at 600 mm spacing. The steel are simulated with truss bar elements in VecTor2. These truss bars are defined under Reinforcement 2 for the finite element models, and the external skin steel plate reference reinforcement type is selected. The properties assigned to the truss bars to represent the external steel are listed in Table 5-3.

Table 5-3 Exterior Steel properties

Reinforcement Diameter (D_b)	10 mm
Yield Strength (F_y)	358 MPa
Ultimate Strength (F_u)	448 MPa
Elastic Modulus (E_s)	200 000 MPa
Strain Hardening Strain (ε_{sh})	10 me
Ultimate Strain (ε_u)	280 me
Thermal Expansion Coefficient (C_s)	10×10^{-6} /°C

A bond model is incorporated into the analyses to consider the stress-slip relationship between the concrete elements and the truss bars representing the reinforcing steel (Wong et al., 2000). The bond model requires the use of link elements. The nodes of the link elements are connected to the nodes at the ends of the truss bar elements and nodes of the concrete elements. The nodes of the truss elements are initially coincident with the nodes of the concrete elements through the link element. The link element serves as the interface whereby the nodes of the concrete elements and nodes of the truss elements can experience differential displacements. VecTor2 provides bond models for embedded deformed bars

and embedded smooth bars. The model requires the bar clear cover and spacing. The numbers of reinforcement layers is another input required by the bond model. The walls consist of a single layer of wire-mesh reinforcement. Also, the end condition of the reinforcement (hooked or not hooked) must be specified for the bond model. The initial wall models considered the current design state, and thus, no end anchorage (straight bar) was selected.

The wall panel system is modelled with three distinct zones as illustrated in Figure 5-8. Zone 3 represents the base beam; Zone 2 simulates the thin concrete panel, and Zone 1 is intended to model the cap beam. The defined Material 1 with smeared reinforcement is assigned to Zone 1 and Zone 3. The meshing parameters are selected to simplify the mesh and to adhere to the maximum number of the elements permitted by VecTor2. An element size of 100 mm by 100 mm was selected for Zones 1 and 3 and 100 mm by 75 mm for Zone 2. The initial model for the squat wall (5000 mm in length and 3000 mm in height) exceeded the maximum element number due to an increase in elements required when bond is explicitly modeled. The number of rectangular concrete elements was 2640, and the number of truss elements was 2680. The resulting number of nodes were 2747. The size of the elements in Zone 2 was modified to meet the limitation of the number of elements. The size of the elements in horizontal direction remained constant (100 mm), while the size of the elements in the vertical direction was increased to 150 mm. In modelling of the slender wall, the maximum number of the elements was not exceeded. The number of rectangular

concrete elements was 1452, the number of truss elements was 1942, and the number of link elements (bond model) was 861 elements.

The vertical and horizontal components of the internal wire-mesh and the external light-gauge steel are described as a series of line segments which are simulated by truss bar elements. The incorporation of specific bond properties is captured in the model through the use of link elements at the interface of the truss elements and the rectangular concrete elements. VecTor2 models bond-slip mechanisms with bond elements and bond stress-slip responses for embedded reinforcement and externally bonded reinforcement (Wong et al., 2000). The perfectly bonded option is used to replicate conditions where perfect bonding between reinforcement and the concrete are assumed. The perfect bond may exist in regions where bond stresses are sufficiently low. In this case, the change in reinforcement strain in response to loading is equal to the change in the total concrete strain (Wong et al., 2000). There are two types of reinforcement in Zone 2. The first defines the welded wire-mesh, and the other is assigned to the exterior steel. The number of elements required to model each wall is different. One of the controlling parameters was the limit imposed by VecTor2 on the number of elements (5500 in total). Table 5-4 lists the number of each element type for the squat wall.

Table 5-4 Number of elements for the squat wall model

Total number of nodes	2402
Total number of elements	3394
Number of rectangular elements	1452
Number of truss elements	1942
Number of triangular elements	0
Number of bond-link elements	861

The number of elements for the slender wall is listed in Table 5-5 below.

Table 5-5 Number of elements for the slender wall model

Total number of nodes	2042
Total number of elements	1944
Number of rectangular elements	960
Number if truss elements	984
Number of triangular elements	0
Number of bond-link elements	1017

As is evident in Table 5-4 and Table 5-5, triangular elements were not used nor necessary in the modelling. The intent was to not rely on non-rectangular elements to reduce the complexity of the models.

5.3.3 Define Test Controls and Models

A job data file is created at the time of analysis within VecTor2 to define the loading criteria. Each load case, such as gravity or lateral, consists of a set of loads that are proportionally increased by a standard load factor from one load stage to the next (Wong et al., 2000). The analyses presented herein required a single lateral load case for each wall model. Each load case consists of an initial load factor and a final factor to define the start and end points for each load case. Increment factors are assigned to determine the increment in each successive load/displacement step. A load type is selected for the analysis method: monotonic, cyclic or reverse cyclic. Table 5-6 illustrates a typical Job Data for the wall panel models.

Table 5-6 Job File input for the wall panel models

Initial Factor	0
Final Factor	30
Increment Factor	0.25
Load Type	Monotonic
Initial load stage	1

5.3.3.a Concrete Models

Various concrete constitutive material models are available in VecTor2, in addition to constitutive models for reinforcement and bond-slip. The concrete material models are divided into three broad mechanical properties: Compression, Tension, and Cracking. The compression models consist of pre-peak models, post-peak models, and compression

softening. Tension models consist of tension softening and tension stiffening. Cracking models consist of cracking criterion, crack stress calculation, crack width check, and crack slip calculation. Table 5-7 lists the available models for the concrete and the models selected for the analyses conducted herein, which correspond to the default options in VecTor2.

Table 5-7 Concrete constitutive models

Concrete Models		
	Models	**Selected Model**
Compression Pre-Peak	Hognestad (Parabola) Popovics (NSC) Popovics (HSC) Hoshikuma Smith – Young Lee 2011 (FRC) Attard & Setunge 1996 Samani & Attard 2012 Elastic-Plastic Bilinear	Hognestad (Parabola)
Compression Post-Peak	Base Curve Modified Park-Kent Monotoya 2003 Popovics/Mander Hoshikuma Saenz/Spacone Lee 2011 (FRC) Attard & Setunge 1996 Samani &Attard 2012 Elastic-Plastic	Modified Park-Kent
Compression Softening	Vecchio 1992-A ($\frac{\varepsilon_1}{\varepsilon_2}$ – Form) Vecchio 1992-B ($\frac{\varepsilon_1}{\varepsilon_0}$ – Form) Vecchio-Collins 1982 Vecchio-Collins 1986	Vecchio 1992-A ($\frac{\varepsilon_1}{\varepsilon_2}$ – Form)

In addition to the models for the concrete, a number of constitutive models are available to simulate the bond interaction between the reinforcing material and the concrete. These include the Eligehausen, Gan-Vecchio, Harjli, and Fujji models. Further background information for these models is presented in Chapter 4. In this study, the Eligehausen model was selected for the analysis that considered bond explicitly.

Table 5-8 lists the models selected to capture the effects of tension and cracking behavioural effects. The models chosen for the analyses are based on the default options.

Table 5-8 Models for tension and cracked concrete

Selected Models	
Tension Stiffening	Modified Bentz 2003
Tension Softening	Bilinear
Crack Stress Calculation	Basic (DSFM/MCFT)
Crack Width Check	Agg/2.5 Max Crack Width
Crack Slip Calculation	Walraven

5.3.3.b Reinforcement Models

The constitutive models for reinforcement are intended to capture the hysteretic response, dowel action, and buckling as provided in Table 5-9. The hysteretic response of the reinforcement is bound by the envelope for the monotonic behaviour of the reinforcement. The monotonic constitutive models include Elastic-Hardening (Curvilinear), Elastic-Hardening (Trilinear), and Elastic-Plastic (Bilinear).

Dowel action measures the transfer of shear forces in cracked reinforced concrete. The Tassios (crack-slip) model is selected to capture dowel action. Three different options are

available in VecTor2 for reinforcement buckling. The Akkaya 2012 model has been selected for the analyses. Similar to the concrete models, the selected models for reinforcement correspond to the default options.

Table 5-9 Reinforcement constitutive models

Reinforcement Models		
	Models	**Selected Model**
Hysteretic Response	Linear Bauschinger Effect (Seckin) Elastic-Hardening (Curvilinear) Elastic-Hardening (Trilinear) Elastic-Plastic (Bilinear) Seckin Guiffre-Menegotto-Pinto Akkaya 2012	Bauschinger Effect (Seckin)
Dowel Action	Tassios (Crack Slip) Tassios (Strength)	Tassios (Crack Slip)
Buckling	Akkaya 2012 Dhakal-Maekawa 2002 Asatsu	Akkaya 2012

5.3.4 Define Support Restraints and Loading

The support restrains for the wall panel system are defined considering the finite element mesh and the support conditions implemented in the field. Figure 5-6 illustrates the connection of the wall panel to the foundation, consisting of ½ inch-diameter ASTM F1554 Grade 55 anchor bolts at 1200 mm spacing. In the models, vertical and translational restraints were imposed at each node along the base beam. The restraining of each node along the base produced a condition that provides more fixity than what was specified in the original design. Note that the original design is based on the wall panels resisting out-of-plane loading. This research is based on investigating the walls to withstand in-plane

lateral loading. It was decided that the spacing of the anchors would be decreased to produce a higher degree of fixity in the walls to ensure a better response to lateral loading. Table 5-10 provides the properties of the anchor bolts.

Table 5-10 Anchor bolt properties

Grade	Diameter (Inches)	Tensile Strength (MPa)	Yield Strength (MPa)	Ultimate Strain (me)
55	1/4 to 2	517-655	380	210

The lateral load was imposed as a support displacement to ensure the post-peak behaviour would be captured in the analyses. Gravity load is not considered in the analysis to reflect the light axial loading that would be imposed on the walls for their current application. The loading is located near the top of the wall and is imposed at the location of the top beam. For the monotonic loading (pushover) used in the preliminary analyses, the loading is imposed at the left end of the wall. Figure 5-9 illustrates the finite element model and loading condition used for the squat wall model.

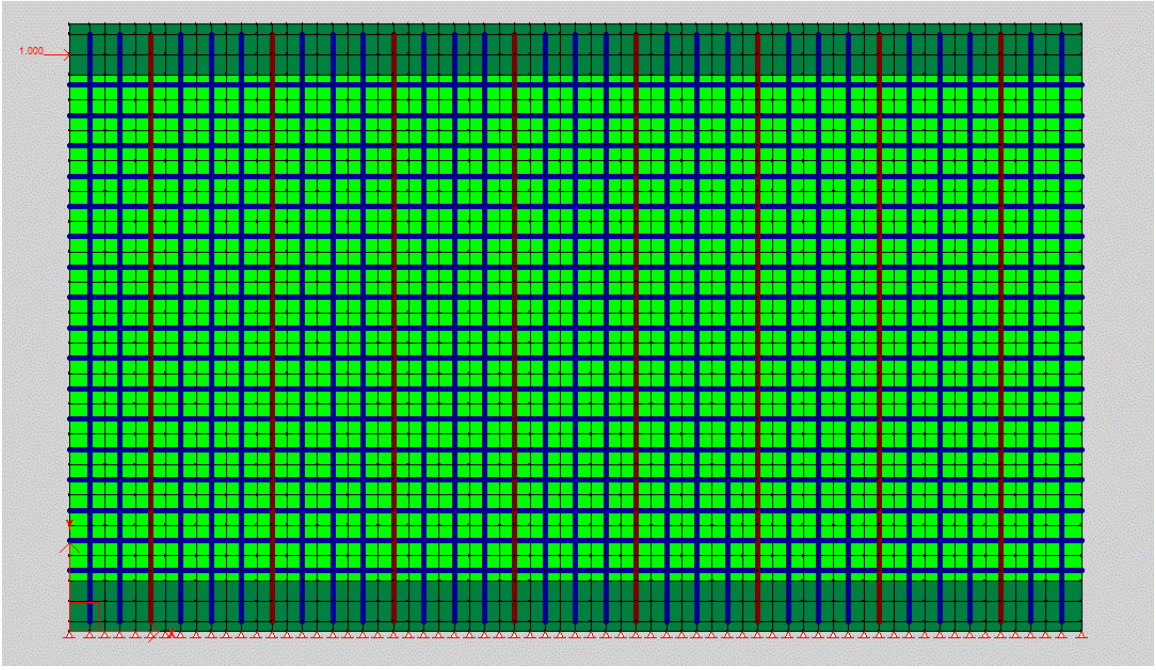

Figure 5-9 Finite element model for the squat wall panel

5.4 Finite Element Results: Slender Wall

In this section, lateral load-displacement responses for the slender wall panel will be presented and discussed. This section provides the results of the parametric study including internal reinforcing bar type, internal reinforcing bar size, bond characteristics, embedment length of the vertical reinforcement into the cap and base beams, anchorage of the internal vertical reinforcement into the cap and base beams, and the influence of the exterior light gauge steel.

To investigate the effect of each parameter, the benchmark design is analyzed in VecTor2 first. Two benchmark models were considered for the parametric analyses based on the aspect ratio of the suggested primary design. The first benchmark model was developed to

represent the slender wall panel and the second for the squat wall panel. The benchmark models are based on the initial design specifications provided by Burnco MFG for the slender wall panel. Figure 5-10 illustrates the finite element model for the benchmark analyses for the slender wall with an aspect ratio of 1.67 (length of 1800 mm and height of 3000 mm height).

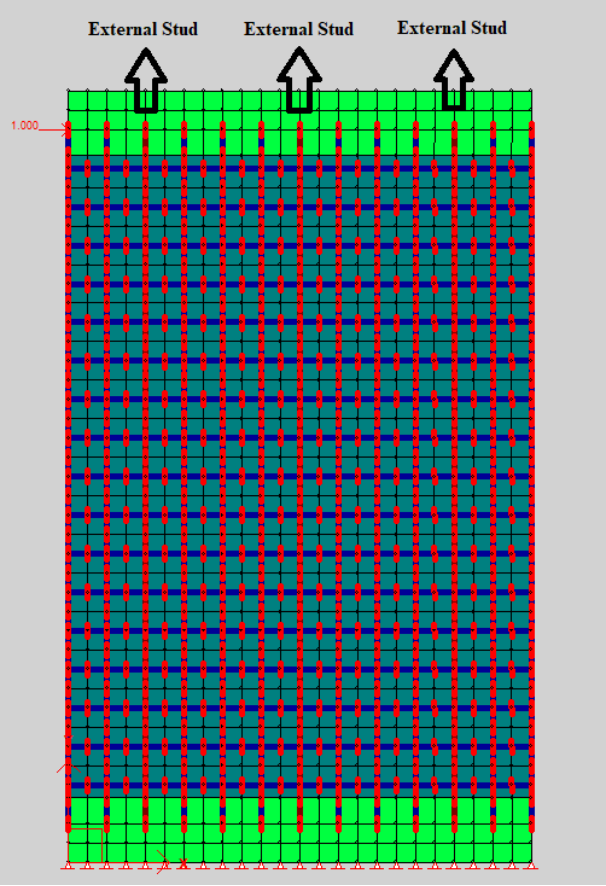

Figure 5-10 Finite element model for slender wall benchmark analysis

To summarize, the benchmark model assumes that the vertical and horizontal reinforcement components of the wire-mesh are imperfectly bonded given the smooth

surface. The diameter of the smooth wire-mesh bars is 6 mm. The vertical bars extend 100 mm into the cap and base beams and are straight (no end hooks). The external steel are extended into the cap and bottom beams with the same embedment length as the vertical wire-mesh bars (100 mm). The external steel have a spacing of 600 mm (3 across the entire panel). The external steel are denoted in Figure 5-10. The small segment of steel embedded into the cap and bottom beams did not have any interaction with the longitudinal reinforcement in those sections. Therefore, the steel were considered imperfectly bonded to the concrete. The cap and base beams were reinforced with 4-15M longitudinal bars and 10M stirrups at 300 mm spacing. The reinforcement in the beams was considered smeared in the model. All nodes along the base beam are restrained in the vertical and horizontal direction, imposing a fixed support condition. The lateral displacement is imposed on the cap beam, pushing the wall from the left side as shown in Figure 5-10.

5.4.1 Bar Type

The first parameter in the initial wall panel design to be investigated to assess the influence on the lateral performance was the type of bar (smooth versus deformed) used for the internal wire mesh. All other characteristics and material specifications remained consistent with the benchmark model. In the benchmark model, the wire-mesh reinforcing consisted of 6 mm-diameter smooth bars, while in the parametric analysis 6 mm-diameter deformed bars were considered. The monotonic lateral force-displacement response of the parametric analysis and the benchmark model are provided in Figure 5-11. The performance of the slender wall with deformed bars is significantly improved over the

benchmark with smooth wire-mesh reinforcement in the panel. The maximum lateral force is increased by a factor of 3.5, and the displacement capacity at peak load is improved by a factor of 23.2. Note that the benchmark analysis is referred to SL, which denotes Slender Wall.

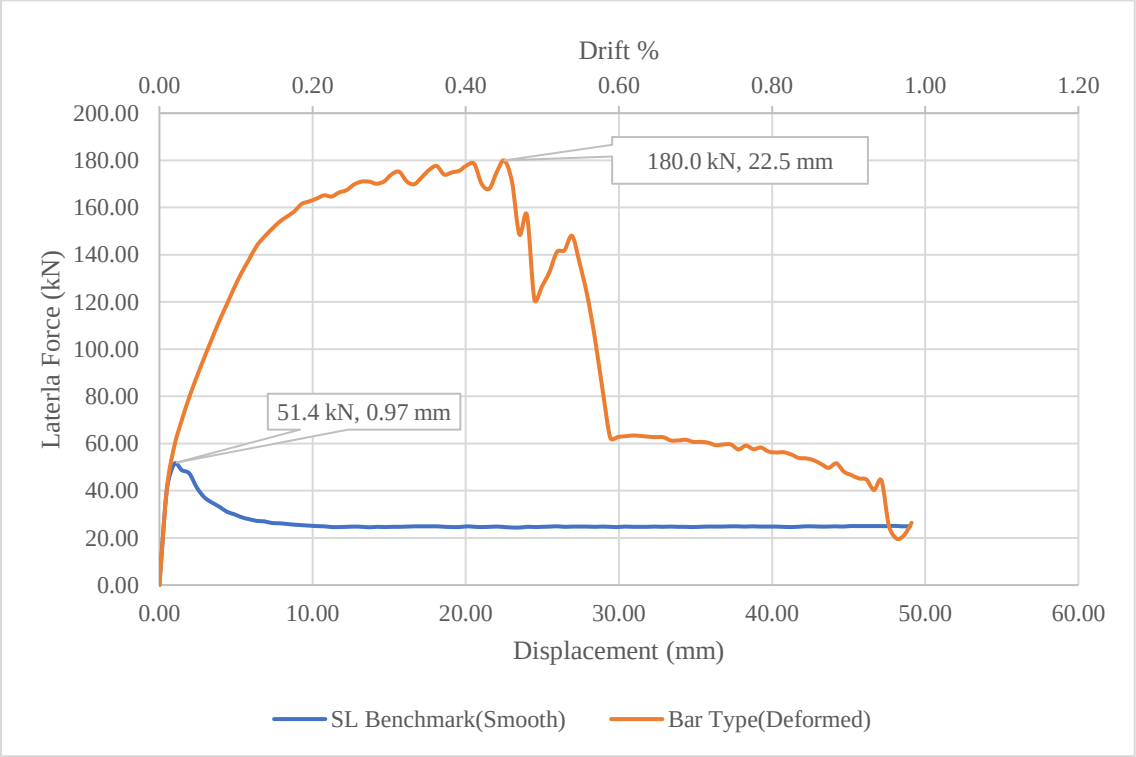

Figure 5-11 Monotonic lateral response for smooth and deformed bars with slender model

As expected, the lateral response of the model with deformed wire-mesh is significantly improved relative to smooth bar model. Recall that the smooth bars are imperfectly bonded in the benchmark model, while the wire mesh with deformed bars is considered fully bonded. Thus, by implementing deformed bars, the bond is improved, resulting in improved lateral response.

5.4.2 Bar Size

The benchmark model consisted of 6 mm-diameter wire-mesh smooth bars. This parametric model is generated to investigate the effect of increasing the bar to a diameter of 10 mm, while all other properties remained consistent with the benchmark model. Figure 5-12 displays the lateral response for the two models under monotonic loading.

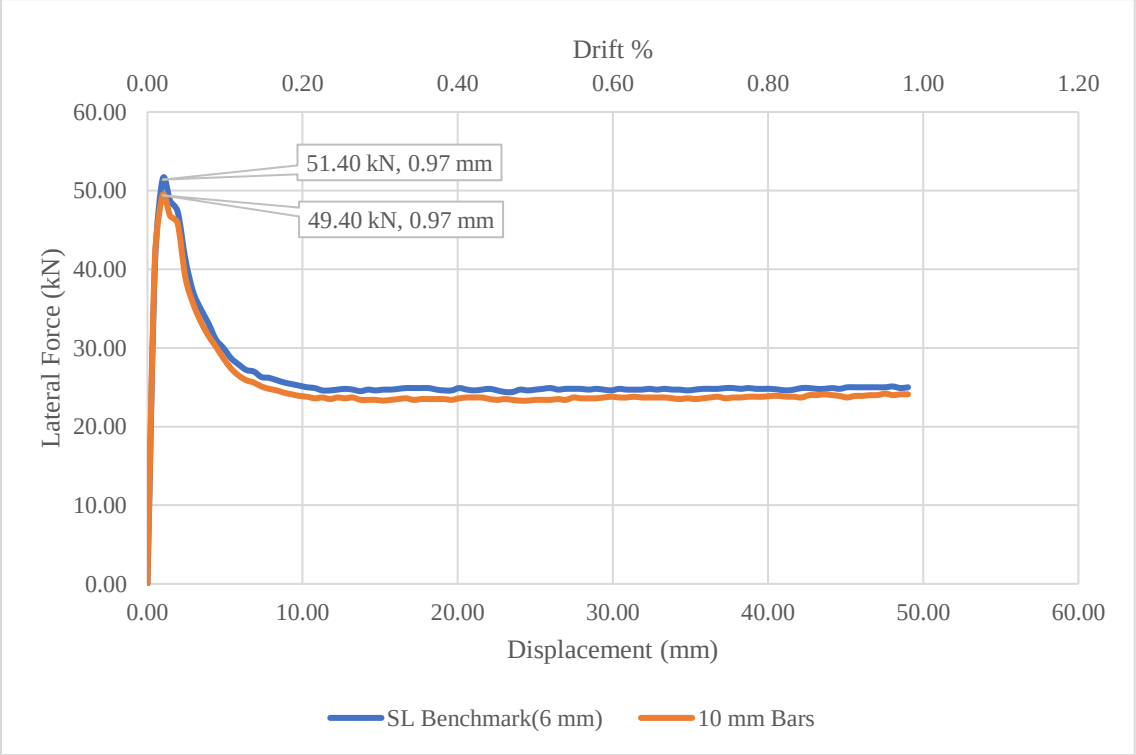

Figure 5-12 Monotonic lateral response for 6 mm and 10 mm diameters wire-mesh bars

The lateral load-lateral displacement responses are approximately identical. Increasing the bar size of the smooth wire-mesh reinforcement had a negligible effect on the lateral performance of the panel. This illustrates that the response of the panel is controlled by the bond characteristics between the smooth wire-mesh reinforcement and the concrete.

5.4.3 Perfect Bonding

As discussed previously, the interaction (bond) between the concrete and reinforcement plays a critical role in the lateral resisting capacity. Three models were generated to determine the influence of bonding of both the vertical and horizontal components of the internal wire mesh reinforcement. Note that for these parametric analyses, all other characteristics were consistent with the benchmark model, including imperfect bonding of the external steel.

5.4.3.1 Perfect Bonding of Vertical Reinforcement

The first model considered ideal bonding of the vertical components of the wire mesh in the panel, while the horizontal components were modeled as imperfect smooth bars. Figure 5-13 illustrates the effect of assuming perfect bonding of the vertical wire mesh. In addition, and for comparison, the response considering perfect bonding of both the vertical wire mesh reinforcement and the external light gauge steel is included. For the light gauge steel, the steel area embedded into the concrete is only considered to contribute.

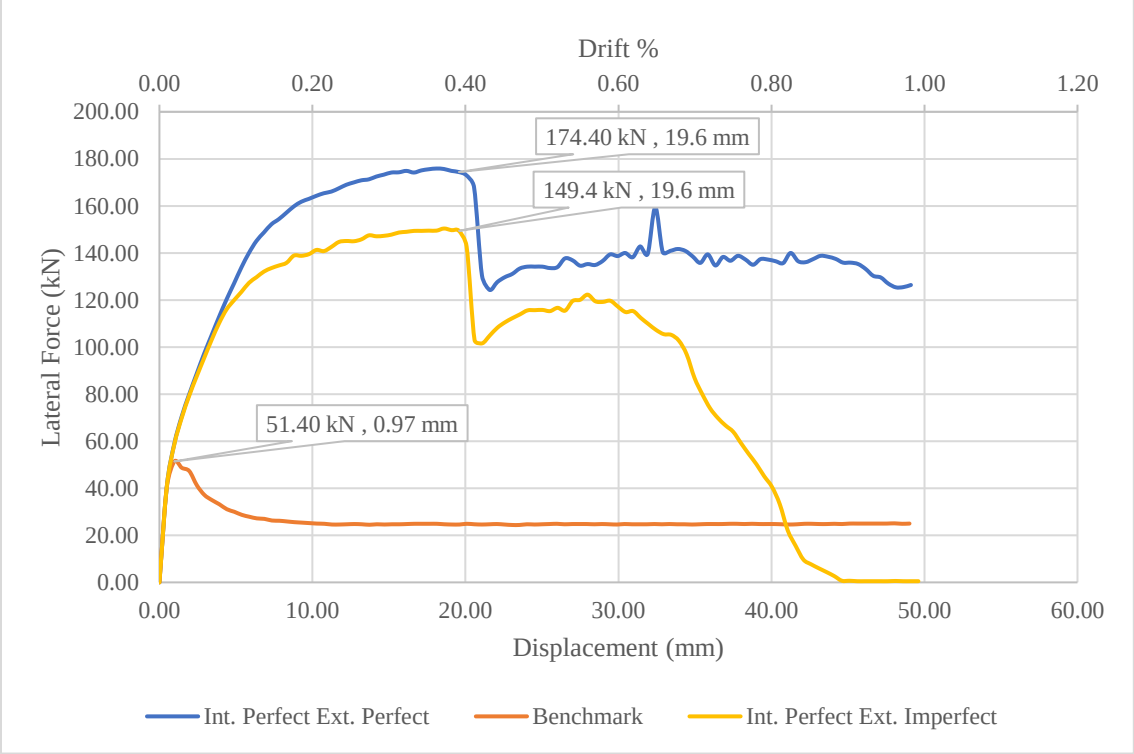

Figure 5-13 Lateral performance with perfect bonding of vertical reinforcement components

The lateral load capacity increased by a factor of 2.9 relative to the benchmark model with the assumption of perfect bonding for the vertical wire mesh reinforcement. In addition, there is a marked improvement in displacement capacity (factor of 20.2) at the peak lateral load capacity. By further assuming full bonding of the light gauge steel, the lateral load capacity increased by a factor of 3.4, while the displacement capacity at peak load increased by a factor of 20.2 relative to the benchmark model.

5.4.3.2 Perfect Bonding of Horizontal Reinforcement

The second model was generated with perfect bonding of the horizontal wire mesh only. Figure 5-14 demonstrates that assuming perfect bond of the horizontal reinforcement does

not influence the performance. The response is a replica of the response predicted with imperfect bonding.

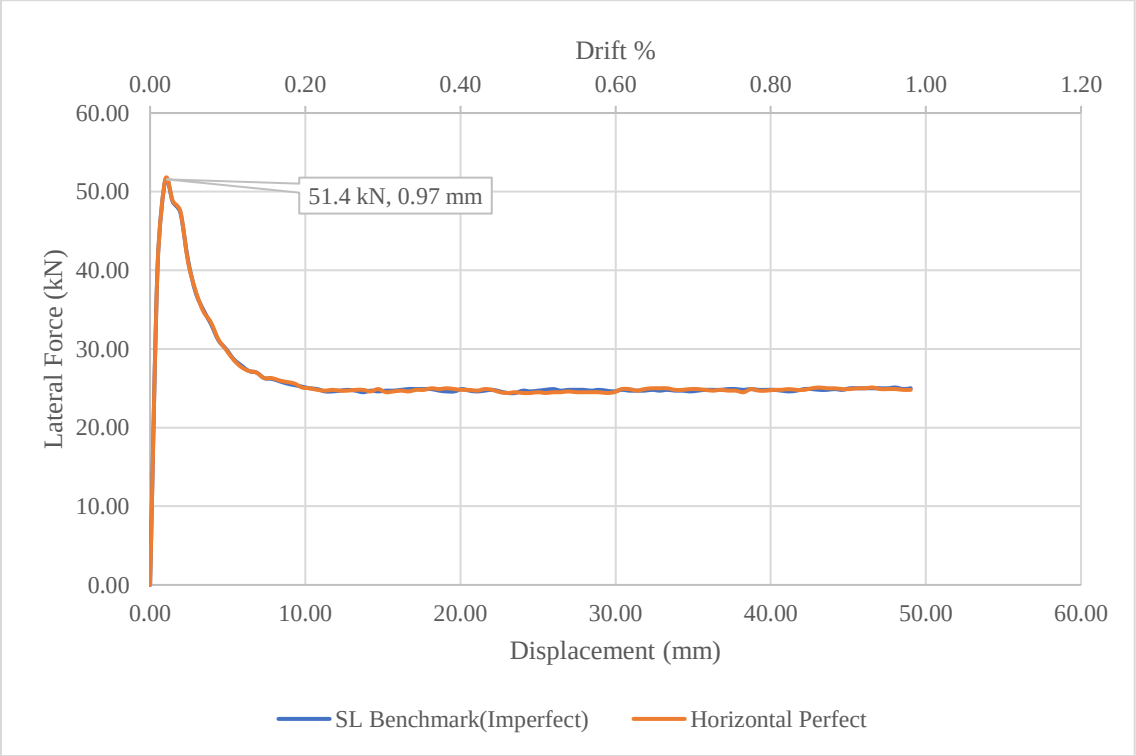

Figure 5-14 Lateral performance with perfect bonding of horizontal wire mesh

5.4.3.3 Perfect Bonding of Vertical and Horizontal Reinforcement

The last model is based on perfect bonding in both directions for the internal wire mesh reinforcement. Note that the embedded section of the external light gauge steel is also considered fully bonded in this model. Figure 5-15 provides a comparison of the lateral resistance of the current model against the benchmark model

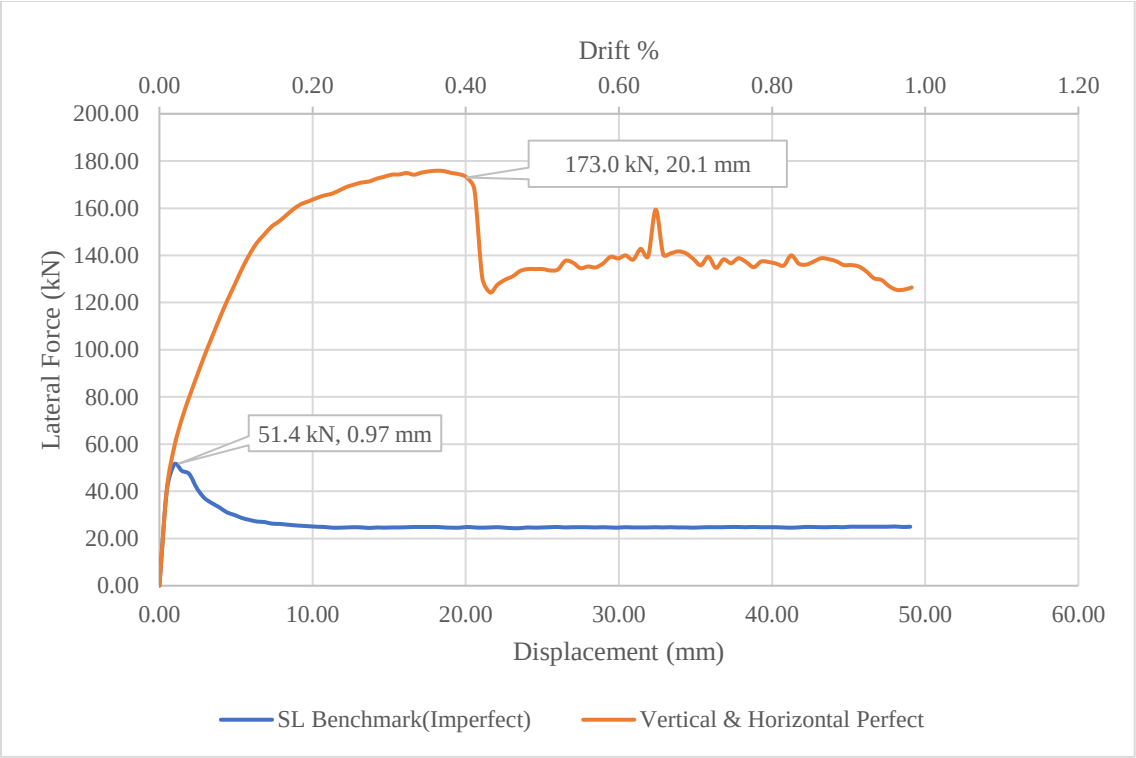

Figure 5-15 Effect of fully bonded reinforcement

In summary, this parametric study of the effect of the bond characteristics of the wire mesh reinforcement illustrated that the horizontal reinforcement, whether modelled as perfect or imperfect, had a negligible effect. The bond condition of the vertical wire mesh controls the response of the wall panel, while perfect bonding of the external light gauge steel provides further strength enhancements but to a lesser extent than the internal wire mesh reinforcement.

5.4.4 Embedment Length

To further understand the influence of the original wall panel design and the detailing, consideration was given to the embedment length of the vertical wire mesh reinforcement and the external light gauge steel into the cap and base beams. The embedment length was increased from 100 mm (benchmark model) to 200 mm in the current model. Figure 5-16 provides the lateral load-lateral displacement responses.

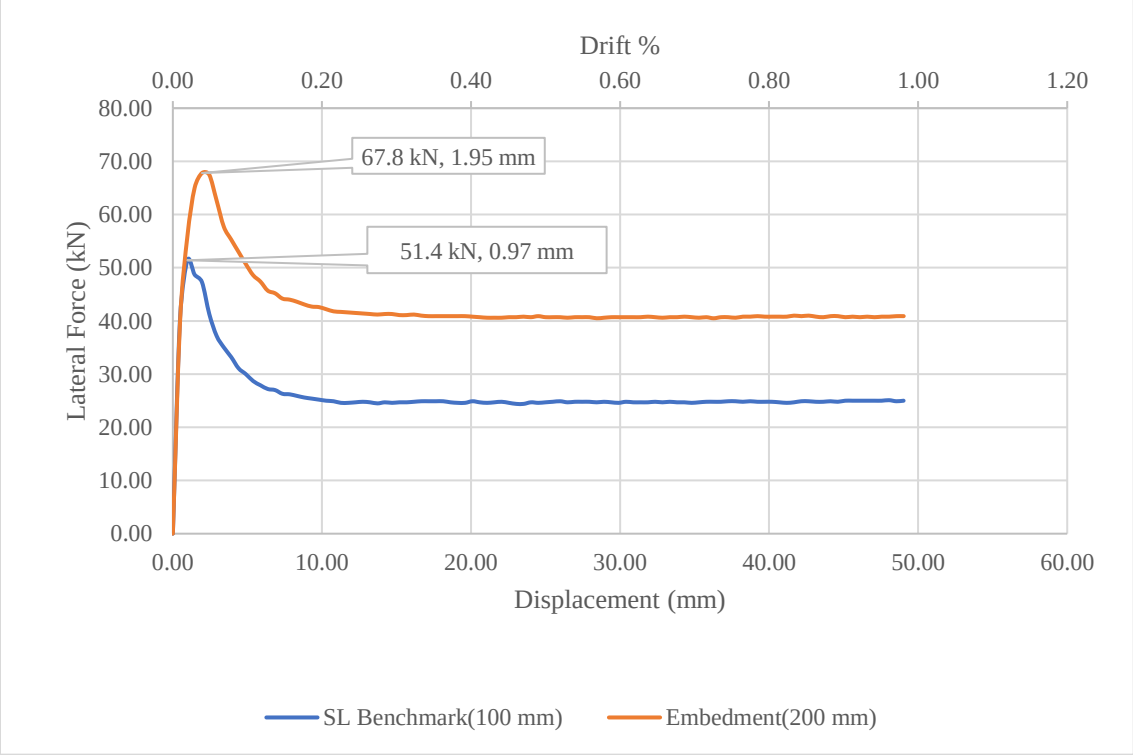

Figure 5-16 Effect of embedment length on lateral response

The increased embedment length resulted in an increase in the lateral strength capacity by a factor of 1.32 and corresponding increase in displacement capacity corresponding to the peak lateral strength capacity by a factor of 2. The increased embedment length resulted in

an improved bond capacity, although not at the same level as the case with fully bonded vertical wire mesh reinforcement and external light gauge steel.

5.4.5 Anchorage of the Internal Reinforcement

The effect of providing hooks at the end of the vertical wire mesh in the cap and base beams was considered. In addition, the external light gauge steel is considered to have improved anchorage in this model. The detailing of this anchorage is discussed in the recommended improvements in the design of the wall panel in subsequent sections. Figure 5-17 illustrates the lateral load-lateral displacement of the current model and the benchmark model.

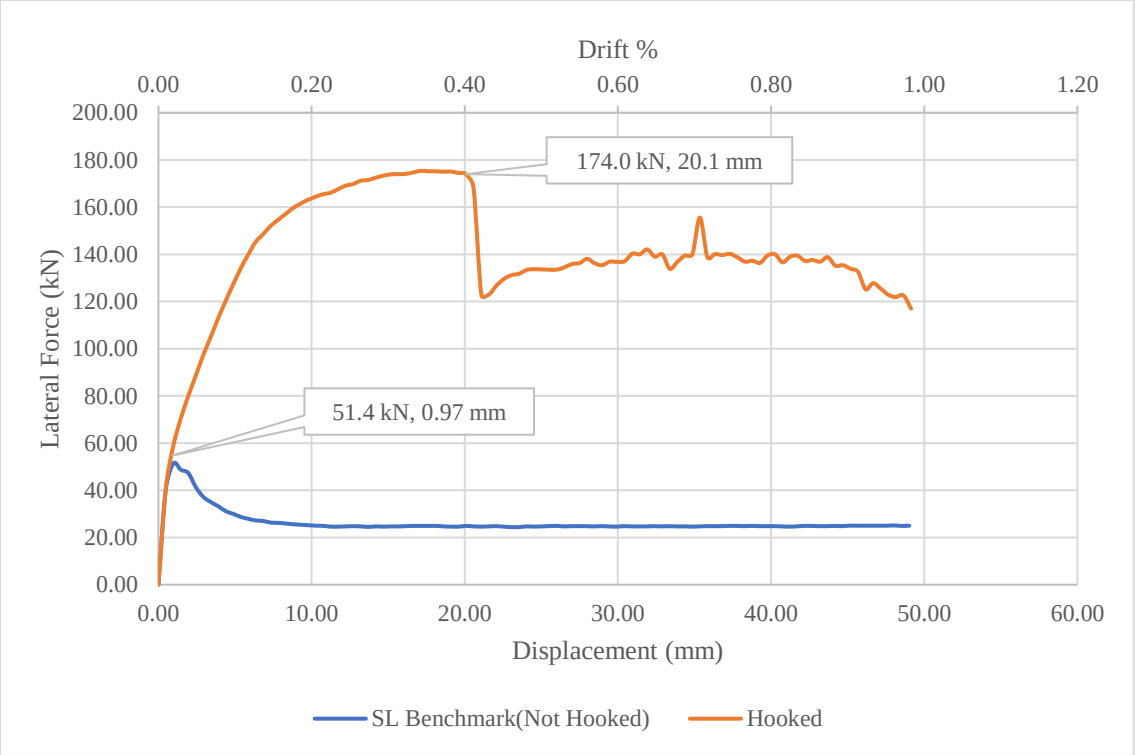

Figure 5-17 Effect of anchored bars in the vertical direction

The lateral strength capacity and the corresponding displacement were significantly increased relative to the benchmark model when applying end hooks to the vertical wire mesh reinforcement and additional anchorage to the external light-gauge steel. The hooks improve the bond characteristics, and the panel exhibits a response that is similar to assuming fully bonded vertical wire mesh reinforcement and external light gauge steel.

5.4.6 Contribution of Light Gauge Steel

The last parameter investigated was the contribution of the external light gauge steel. In the current model, the steel were removed, while they are present in the benchmark model. Note that the joists are considered imperfectly bonded to the concrete panel given that only the flange is embedded into the concrete panel and only 100 mm of the ends extend into the cap and base beams. Figure 5-18 demonstrates the contribution of the external joists.

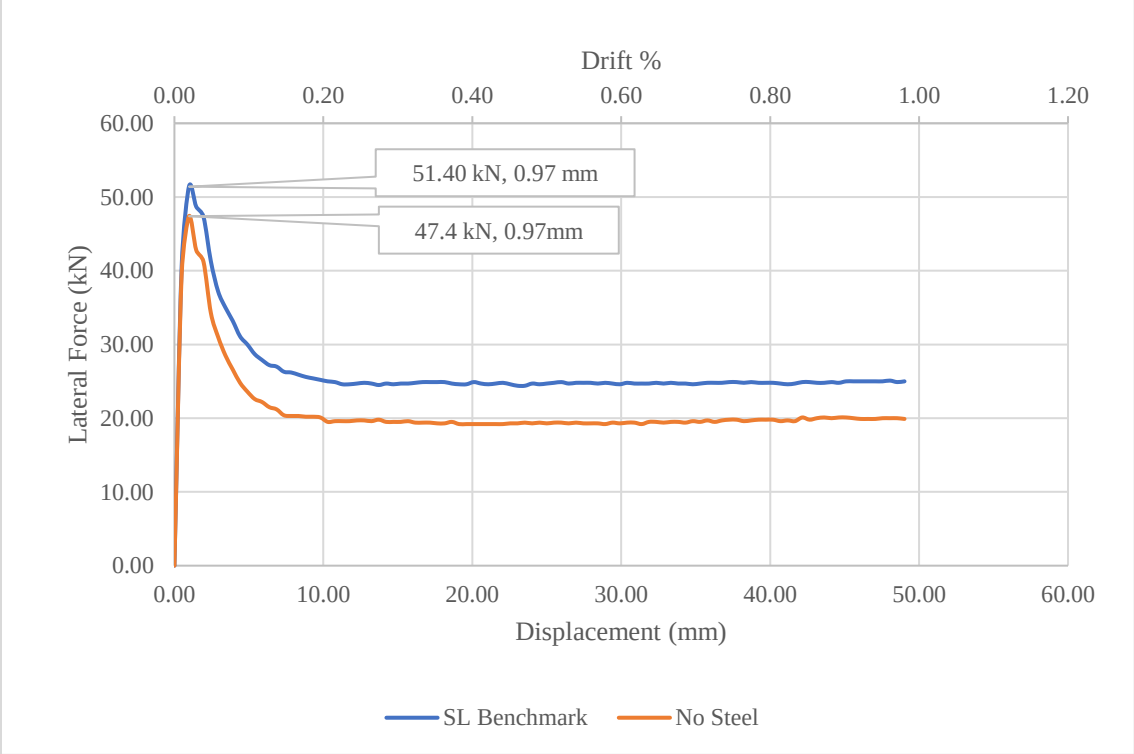

Figure 5-18 Effect of the exterior light gauge steel

The presence of the external light gauge steel provides an increase in the lateral load capacity by a factor of 1.08, while the corresponding displacement capacity at peak lateral load remained the same. This is a consequence of the assumed flange-only portion of the steel contributing to the resistance of the wall, the minimum number of joists across the width of the wall panel, and the assumed imperfect bond between the steel and the concrete. Note that the total area of the steel that are assumed to contribute to the lateral resistance is 399 mm^2, compared to 832 mm^2 provided by the internal vertical wire-mesh reinforcement. Another assumption would be to consider the contribution of the full cross-sectional area of the steel on lateral resistance. The total cross-sectional area of each stud

is 386 mm^2. The figure below compares the response for full area model and flange-only model.

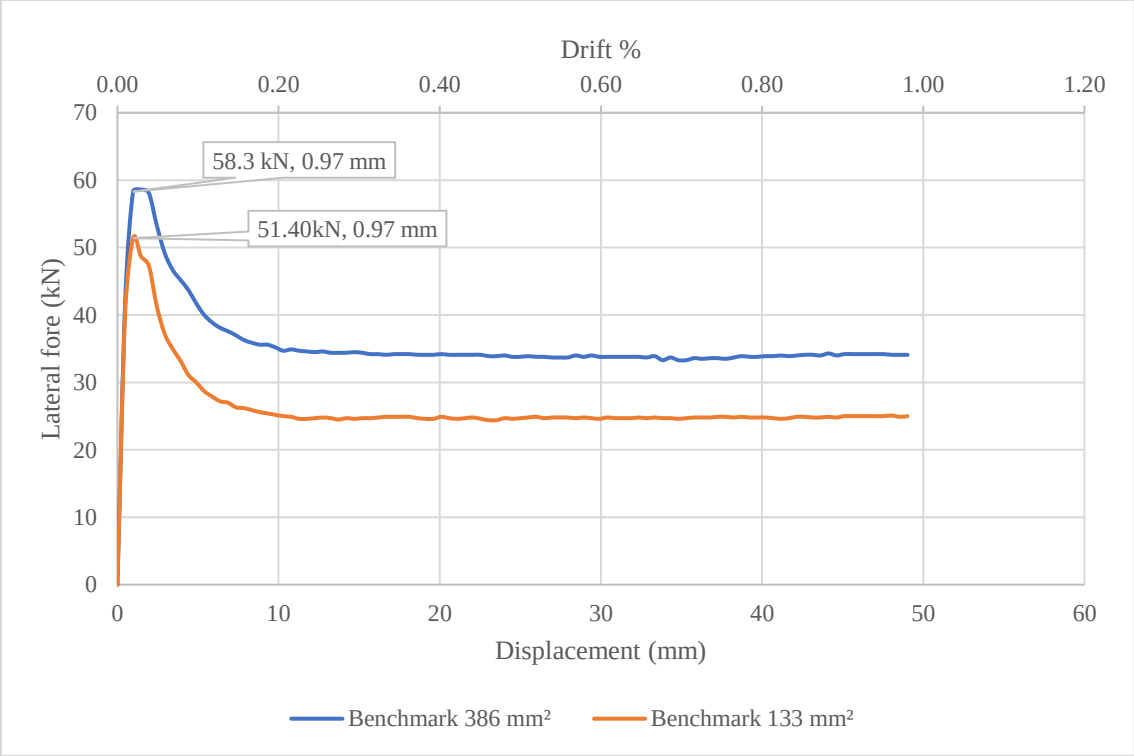

Figure 5-19 Full cross-sectional contribution and flange-only contribution for exterior steel

As illustrated in Figure 5-19 the model with the full cross-sectional area of the external light-gauge steel provides a marginally improved lateral load capacity. The analyses with the external light-gauge steel further highlight the importance of improving the bond characteristics between this reinforcement and the concrete wall panel. Recall that in the analyses the external light-gauge steel are assumed imperfectly bonded to the concrete.

5.4.7 Summary of the Parametric Analysis for Slender Wall

A review of the parametric analyses illustrates that hooking the ends of the vertical wire mesh reinforcement or assuming perfect bonding of the same bars provides the greatest improvement in the lateral performance. The use of deformed bars in place of smooth bars increased the lateral performance of the wall as well.

Table 5-11 provides a summary of the results of the parametric analyses in comparison to the benchmark model.

Table 5-11 Summary of Parametric Analyses for the Slender Wall

Model	Loading	Analysis/Parameter	Comments
SL-1	Monotonic	*Bar size*: 6 mm diameter smooth wire-mesh compared to 10 mm diameter smooth wire-mesh	Increasing the wire mesh size does not have a significant effect.
SL-2	Monotonic	*Bar type*: 6 mm diameter smooth wire-mesh compared with 6 mm diameter deformed wire-mesh	Deformed bars provide a significant increase in lateral response.
SL-3	Monotonic	*Embedment length*: 100 mm vertical embedment compared with 200 mm vertical embedment	Increased embedment length provides an improved lateral response.
SL-4	Monotonic	*Anchorage*: Hooked vertical 6 mm smooth bars and anchored external steel compared with no end anchorage	The hooked end bars and anchored external steel provides a substantial improvement in the lateral performance
SL-5	Monotonic	*Perfect bonding of vertical wire mesh and external light gauge steel*: 6 mm smooth wire-mesh and external steel with perfect bonding in vertical direction compared with imperfect bonding in the vertical direction	Assuming perfect bonding of the vertical wire mesh significantly improves the lateral performance. Bonding of the external light gauge steel provides additional strength enhancement.
SL-6	Monotonic	*Perfect bonding of the horizontal wire mesh*: 6 mm smooth wire-mesh with perfect bonding in	Improving the bond of the horizontal wire mesh is not sufficient in itself to

		horizontal direction compared with imperfect bonding in the horizontal direction	improve the lateral performance.
SL-7	Monotonic	*Perfect bonding of wire mesh reinforcement and external light gauge steel*: 6 mm smooth wire-mesh and external steel with perfect bonding compared with imperfect bonding	Perfect bonding of the vertical wire mesh is more critical in improving response than imposing a perfect bond in the horizontal wire mesh reinforcement.
SL-8	Monotonic	*Contribution of external light gauge steel*: Panel with exterior steel compared with a model without exterior steel	The existence of the light gauge steel marginally improves the lateral resistance of the wall.

Based on the parametric analyses, providing a mechanism to improve the bonding of the internal vertical reinforcement, such as end hooks, using deformed bars and to a lesser extent increasing the embedment length, resulting in the greatest enhancement in the lateral response of the panel. Further improvements are possible by improving the bond of the external light-gauge steel.

5.5 Finite Element Results: Squat Wall

An additional set of parametric analyses were conducted on the squat wall panel. The squat panel, as originally designed and manufactured by Burnco MFG, is 5000 mm in length and 3000 mm in height (aspect ratio of 0.6). Figure 5-20 illustrates the finite element model generated for the analyses with Program VecTor2.

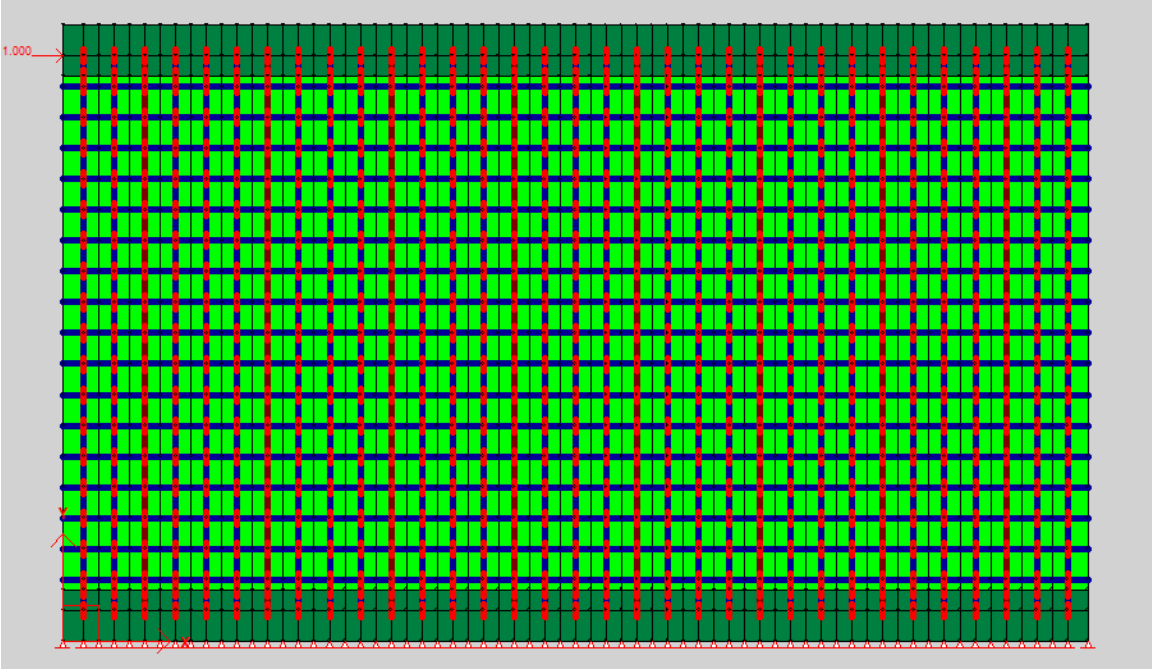

Figure 5-20 Finite element model for squat wall benchmark analysis

The material specifications and modelling procedures for the squat wall benchmark analysis was similar to the slender wall panel model. With regards to the parametric analyses that investigated the effect of bond characteristics of the vertical and horizontal wire mesh reinforcement, only the vertical reinforcement was considered. This was the result of the limitation in the number of elements permitted in VecTor2. Note that explicitly modelling bond requires bond link elements between the truss elements and the concrete rectangular elements, resulting in an increase in the number of elements. The horizontal wire mesh reinforcement is modelled with truss bar elements attached directly to the concrete without the inclusion of bond-link elements. This modeling approach leads to perfect bonding of the horizontal reinforcement. In addition, the length of the wall

increased relative to the slender wall, resulting in an increase in elements. The choice to investigate the effect of bond on the vertical wire mesh reinforcement stems for the results of the parametric analysis of the slender wall model that demonstrated a greater influence of the vertical reinforcement on the lateral performance.

In Table 5-11, it is noted that the performance of the panel when both the vertical and horizontal directions of the wire are perfectly bonded is similar to the response when the vertical reinforcement only is assumed perfectly bonded.

In the initial suggested design, the embedment length for the exterior steel was 100 mm into the cap and base beams. There was no interaction between this steel and either the longitudinal and transverse reinforcement in cap and base beams. As previously stated, the flange portion of the external light gauge steel are embedded into the concrete wall panel, an area of approximately 133 mm^2. This area is considered in the model and contributes to the lateral performance. The following sections provide the results from the parametric analyses for the squat wall panel. For each of the results, the benchmark model results are superimposed to provide a comparison.

5.5.1 Bar Type

The first parameter investigated was the bar type used as internal reinforcement for the wall panel. The finite element model has been generated based on the benchmark model previously explained. All characteristics and material specifications remain the same as those highlighted and discussed in the slender panel model. The current analysis considers the wire-mesh reinforcement to be deformed rather than smooth, which is the condition of

the wire-mesh in the original design state. Recall that the wire mesh has a diameter of 6 mm. Figure 5-21 illustrates the monotonic lateral load-lateral displacement responses of the squat wall models considering deformed and smooth wire mesh reinforcement. The performance of the wall with deformed wire mesh is significantly improved in comparison to the benchmark model with smooth wire-mesh reinforcement. This is attributed to the improved bond properties with the deformed wire mesh in the panel. The maximum lateral force increased by a factor of 2.8 and the displacement corresponding to the maximum lateral force improved by a factor of 5.4.

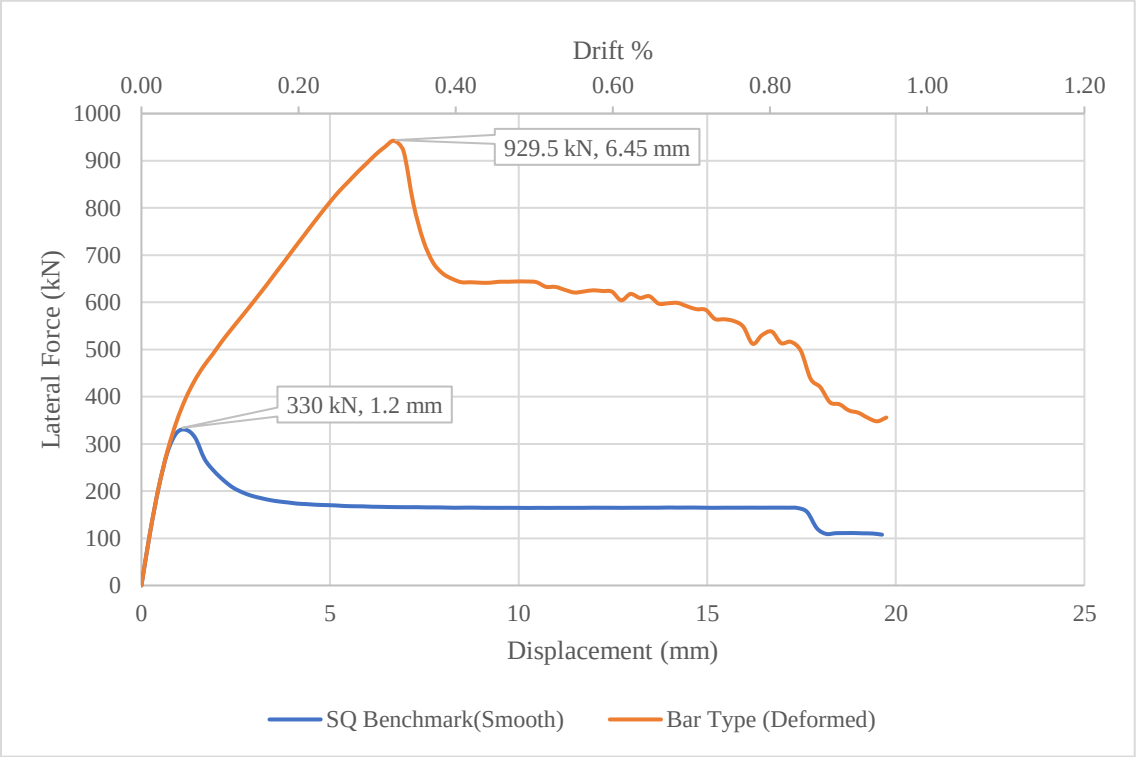

Figure 5-21 Monotonic lateral response for smooth and deformed bars with squat wall model

5.5.2 Bar Size

The benchmark model consists of 6 mm-diameter wire-mesh smooth bars in the squat wall panel. An analysis was conducted to investigate the effect of increasing the bar diameter to 10 mm. All other characteristics remain constant and similar to the benchmark model, including the exterior light gauge steel (8 across the length), anchorage of the reinforcement and the embedment length. Figure 5-22 shows the lateral response for the current and benchmark models under monotonic loading.

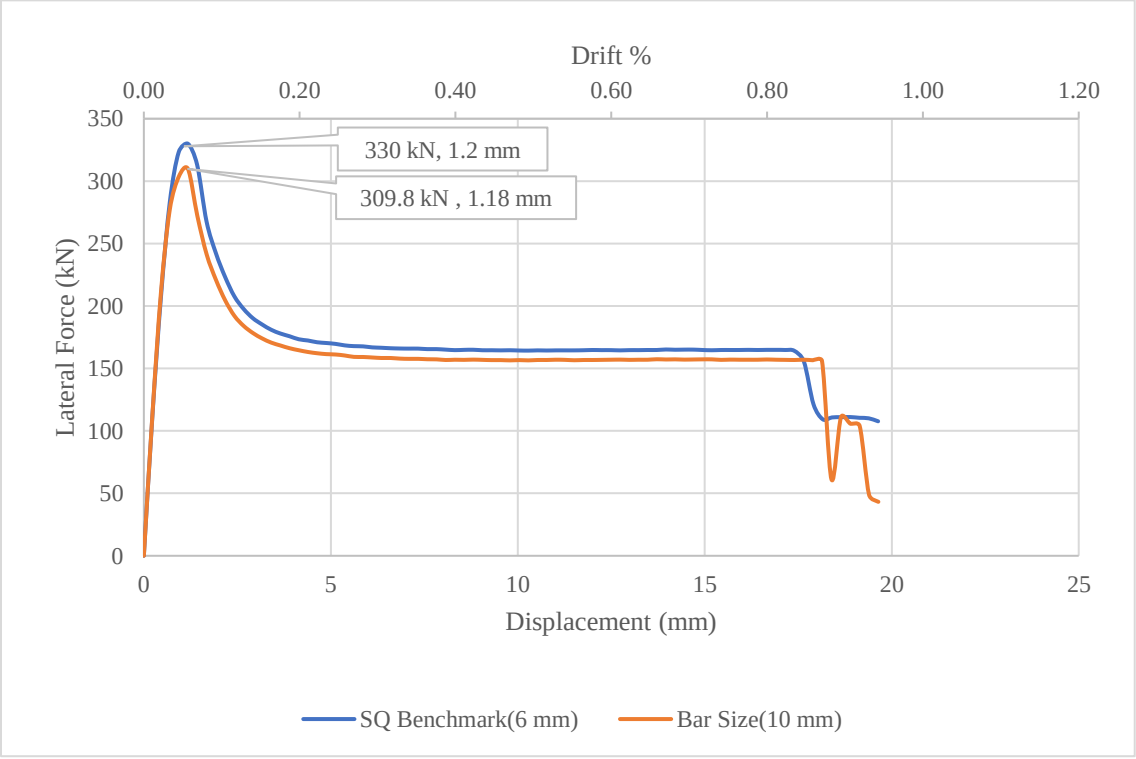

Figure 5-22 Monotonic lateral response for 6 mm and 10 mm diameters wire mesh reinforcing bars

The lateral response is similar whether a 6 mm or 10 mm diameter bar is used for the internal wire mesh in the squat wall panel. This is directly attributed to the bond properties

of the smooth bars. It is evident that the response is controlled by slip of the bars, and thus, increasing the bar size has minimal influence. The following section considers the effect of assumed bond properties for the internal wire mesh reinforcement.

5.5.3 Perfect Bonding

As discussed previously, the interaction (bond) between the concrete and reinforcements plays an essential role in the lateral resisting capacity. Due to limitations on the number of elements permitted in VecTor2, this parametric investigation considered the bond characteristics of the vertical wire mesh only. As illustrated in the analyses of the slender wall panel, assuming perfect bond of the vertical wire mesh reinforcement had a significant influence on the lateral performance of the wall, while assuming perfect bonding in the horizontal wire mesh had a negligible effect. Thus, based on the findings from the slender model analyses, the analysis in this section focused on the bond condition of the vertical wire mesh.

5.5.3.1 Perfect Bonding of Vertical Reinforcement

The parametric analysis in this section considers perfect bonding in the vertical wire mesh of the squat wall panel. The purpose of the analysis was to determine the effect of assuming a perfect bond for the internal vertical wire-mesh reinforcement. Figure 5-23 illustrates the results of the assumed bond characteristics. In addition, and for comparison, the response considering perfect bonding of both the vertical wire mesh reinforcement and the external

light gauge steel is included. For the external light gauge steel, this is based on the flange contribution solely.

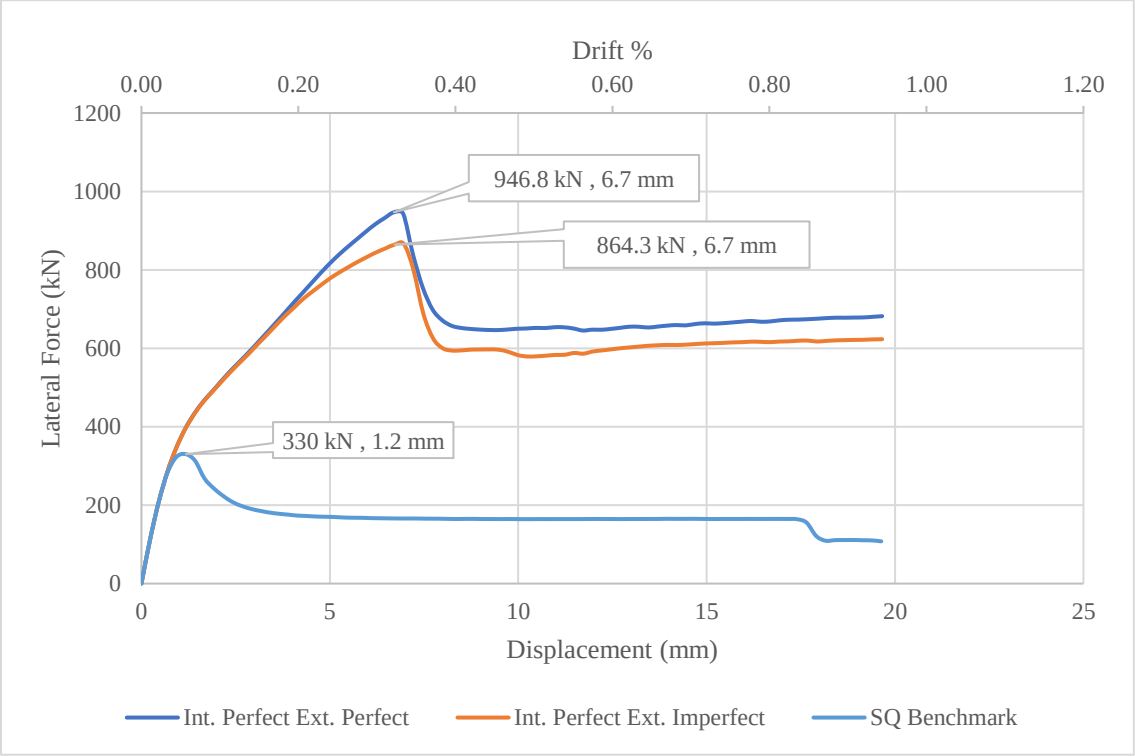

Figure 5-23 Lateral performance with the perfect bonding of vertical reinforcement in squat panel

The lateral resistance load increased by a factor of 2.62, while the corresponding displacement capacity increased by a factor of 5.58 when perfect bonding is assumed for the internal wire-mesh reinforcement. Further assuming fully bonded external light gauge steel resulted in an increase in the lateral strength by a factor of 2.87, while the displacement capacity increased remained the same. For the squat wall, the inclusion of the light gauge steel had a marginal increase in the lateral performance.

5.5.4 Embedment Length

A parametric analysis was also conducted on the embedment length of the vertical wire-mesh reinforcement and external light gauge steel into the cap and base beams in the squat wall. The embedment length increased from 100 mm (benchmark model) to 200 mm in the current model. Figure 5-24 illustrates the difference in the current and benchmark models.

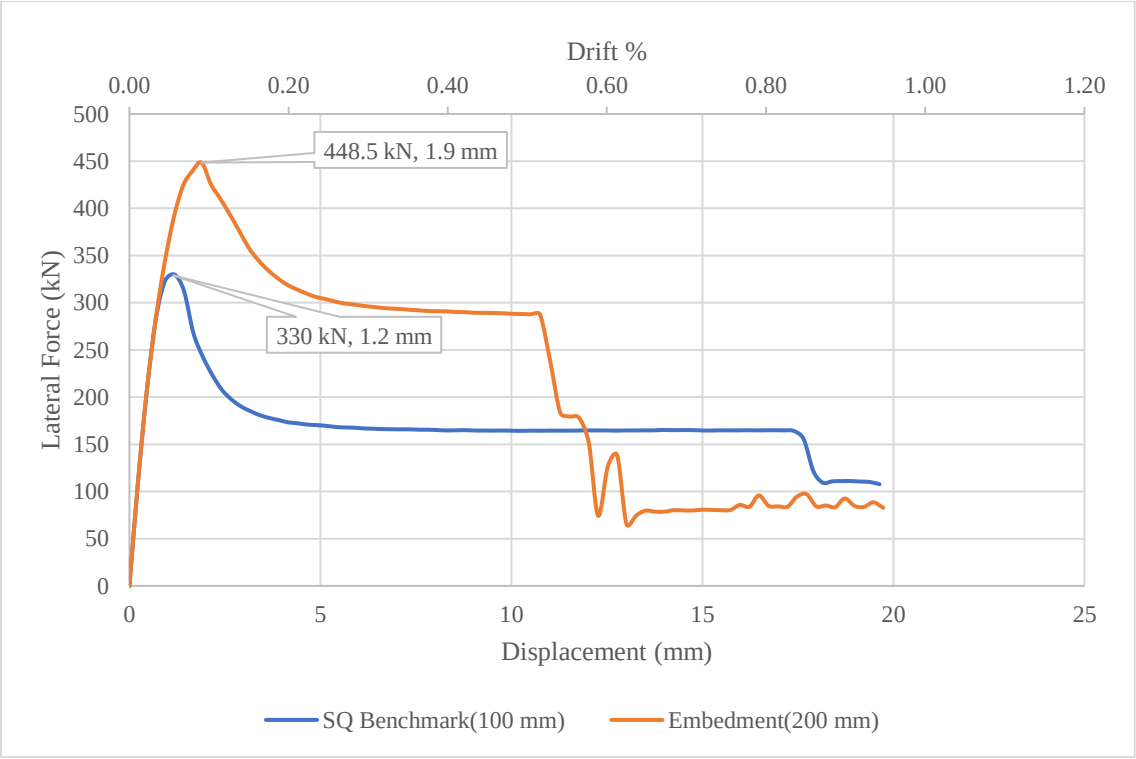

Figure 5-24 Effect of embedment length on lateral response of the squat wall

Although the displacement capacity between the two models were similar, the lateral strength capacity increased by a factor of 1.36 due to an increase in the embedment length, which resulted in an improved bond capacity for the vertical wire-mesh reinforcement and the external light gauge steel.

5.5.5 Anchorage of Internal Reinforcement

The initial design of the wall panel did not consider or include end anchorage for the internal vertical wire-mesh reinforcement or external light gauge steel into the cap and base beams. The current model considers the effect of hooked end wire mesh bars and improved end anchorage of the external light gauge steel into the cap and base beams. Figure 5-25 illustrates the performance of the squat wall upon the inclusion of improved end anchorage.

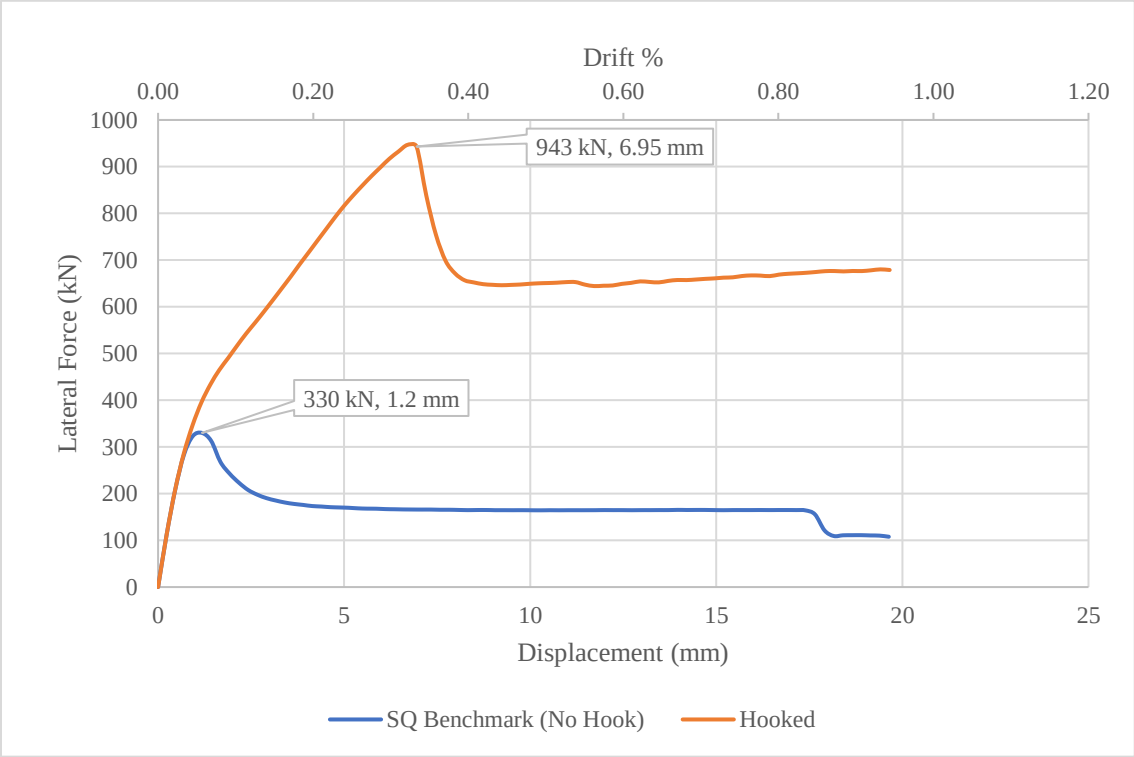

Figure 5-25 Effect of the anchored reinforcement in the vertical direction for squat panel

Comparing the end anchored vertical steel in the squat wall with an increased embedment length illustrates that the effect of anchorage in the squat wall plays a more active role than the larger embedment length. The maximum lateral force in the anchored model increased

by a factor of 2.86, whereas the maximum lateral force increased by a factor of 1.36 with an increased embedment length. Although the effect of the embedment length in the squat panel is less pronounced than the anchored vertical bars, it is not negligible.

5.5.6 Light Gauge Steel

The final parameter investigated was the contribution of the exterior light gauge steel. The performance of the squat panel was assessed with (benchmark model) and without the external light-gauge steel (current model). All other characteristics in the current model of the squat wall were consistent with the benchmark model. Figure 5-26 illustrates the difference in the lateral performance of both models.

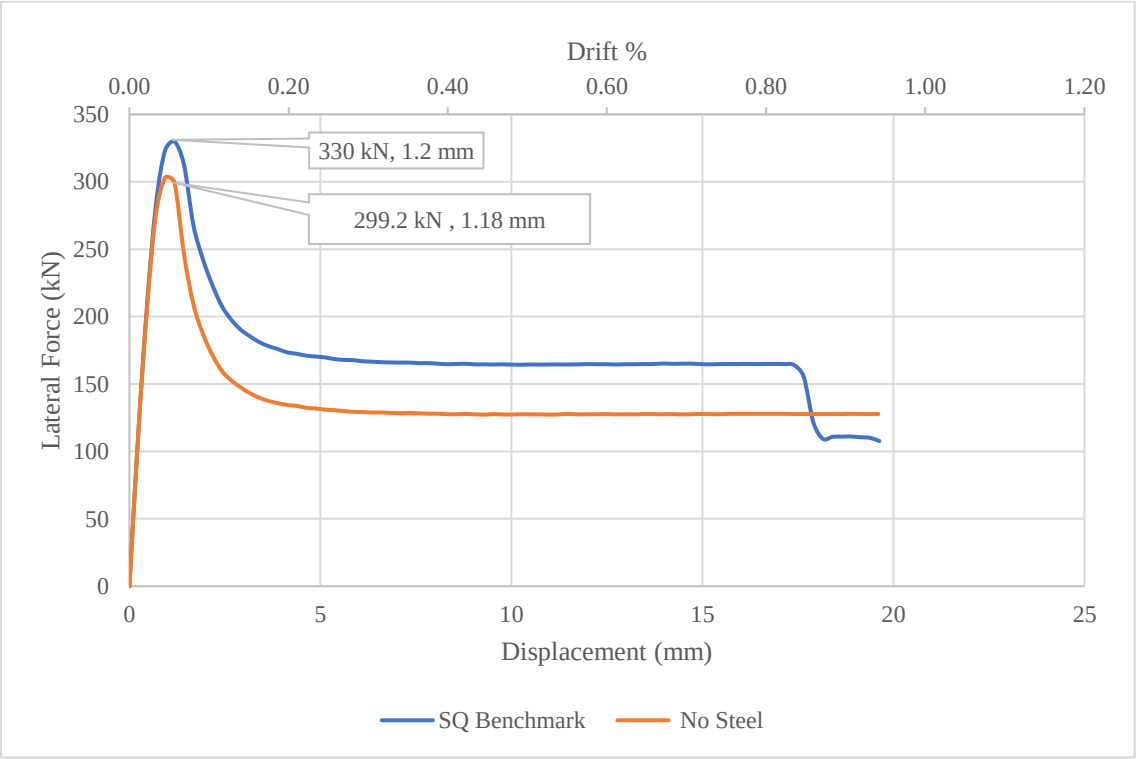

Figure 5-26 Effect of the exterior light gauge steel on the lateral performance of the squat wall

The presence of the exterior light gauge steel marginally improved the lateral resistance of the wall. This is a consequence of the assumed flange-only portion of the steel contributing to the resistance of the wall, the minimum number of steel joists across the width of the wall panel, and the assumed imperfect bond between the studs and the concrete. Note that the total area of the steel that are assumed to contribute to the lateral resistance is 1064 mm^2, compared to 2112 mm^2 provided by the internal vertical wire-mesh reinforcement. Figure 5-27 shows the comparison for the lateral response of the model with full cross-sectional contribution versus the flange-only model.

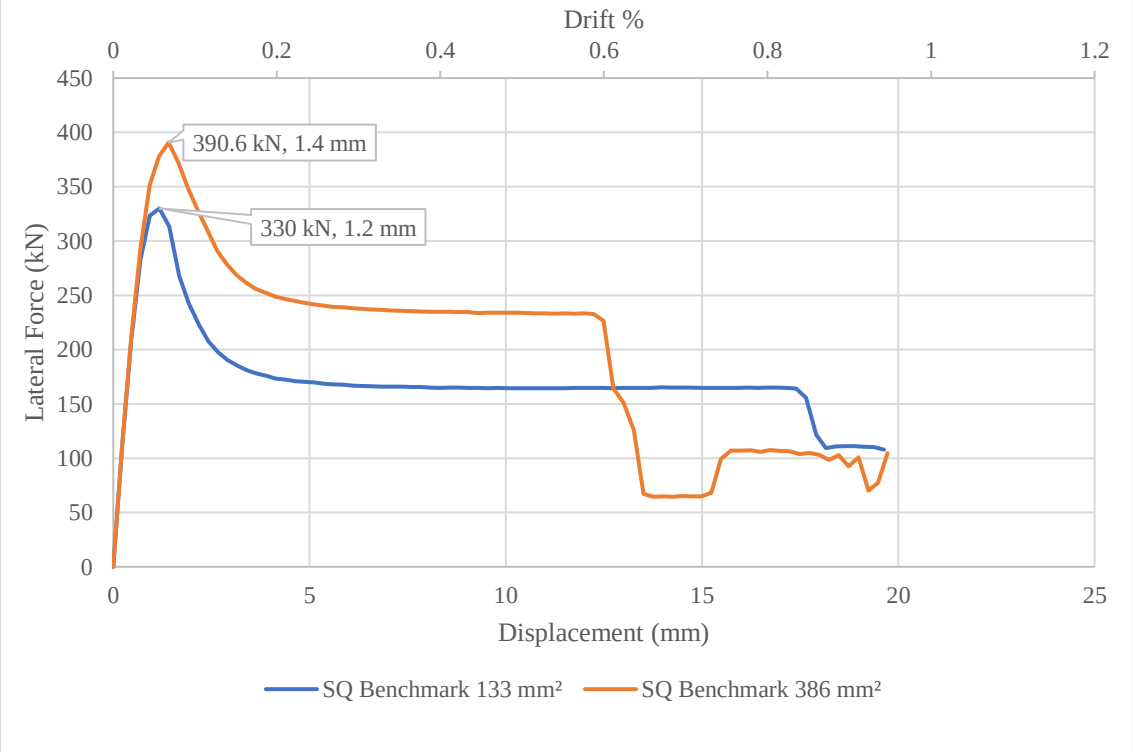

Figure 5-27 Full cross-sectional contribution and flange-only contribution of exterior studs

The response in orange in Figure 5-27 represents the lateral resistance of the model with the full contribution of the cross-sectional area of the exterior steel. The total cross-sectional area for each joist was 386 mm^2. The total area of the steel that are assumed to contribute in lateral resistance is 3088 mm^2. The maximum lateral force increased by a factor of 1.18 when the entire cross-section of the exterior steel are assumed to contribute to the lateral resistance.

5.5.7 Summary of the Parametric Analyses for Squat Wall

A review of the parameters investigated for the squat wall panel illustrates that using deformed vertical wire-mesh reinforcement, and providing improved end anchorage provide the greatest improvements in the lateral performance. Essentially, any improvement in the bond of the vertical wire-mesh reinforcement and the external light-gauge steel results in significant improvements. Table 5-12 provides a summary of parametric analyses in comparison to the benchmark model results.

Table 5-12 Summary of Parametric Analyses for the Squat Wall

Model	Loading	Analysis/Parameter	Comments
SQ-1	Monotonic	*Bar size*: 6 mm diameter smooth wire-mesh compared to 10 mm diameter smooth wire-mesh	Increasing the size of the wire mesh does not have a significant effect.
SQ-2	Monotonic	*Bar type*: 6 mm diameter smooth wire-mesh compared with 6 mm diameter deformed wire-mesh	Deformed bars provide a significant improvement in lateral response.
SQ-3	Monotonic	*Embedment*: 100 mm vertical embedment compared with 200 mm vertical embedment	Increased embedment length provides a slightly improved lateral response.
SQ-4	Monotonic	*Anchorage*: Hooked vertical 6 mm smooth bars and improved anchorage of external steel compared with straight bars without anchorage	The anchorage provides an improvement to the lateral performance.
SQ-5	Monotonic	*Perfect bonding of vertical wire mesh and light gauge steel*: 6 mm smooth wire-mesh with perfect bonding in vertical direction compared with imperfect bonding in the vertical direction	Assuming perfect bonding of the vertical wire mesh significantly improves the lateral performance. Bonding of the external light gauge steel provides additional strength enhancement.
SQ-6	Monotonic	*Contribution of external light gauge steel:* Panel with exterior steel compared with a model without exterior steel	The existence of the joists slightly improves the lateral resistance of the wall. Lateral strength improved by 10%.

5.6 Comparison Between Slender and Squat Wall Panels

ASCE41-13 specifies that the aspect ratio (height to width) of reinforced concrete walls affect the hysteresis response (Pekelnicky & Poland, 2012). The mode of failure for a thin wall with aspect ratio more than three is dominated by flexure effects; while for squat walls with an aspect ratio of less than one, it is dominated by shear-related mechanisms in the

web portion of the wall (Shin & Kim, 2014). Note that in this study, two wall types were considered: slender and squat. The squat wall has an aspect ratio of 0.6; while the so-called slender wall a ratio of 1.67, which lies between squat and slender.

The parametric analyses conducted on both walls illustrated differences in response to the same parameter. By changing the bar type from smooth to deformed, the displacement capacity increases for the slender and squat panels (Figure 5-11 and Figure 5-21). Increasing the size of the bar was not tangible in either the slender and squat wall panels. This was more the effect of the imperfect bond assumption and straight bars (Figure 5-12 and Figure 5-22). Altering the bond from imperfect to perfect should result in an increase in lateral performance for both walls. The most significant effect on the lateral performance of the wall was due to the assumption of perfect bond for the vertical components of the internal wire-mesh reinforcement. The slender wall panel experienced an increase in lateral strength by a factor of 3.07 and the squat wall 2.87 (Figure 5-13 and Figure 5-23). Increasing the embedment length of the vertical wire-mesh reinforcement from 100 mm to 200 mm into the cap and base beams lead to an increase factor of 1.32 in the lateral strength resistance in the slender wall and 1.36 in the squat wall (Figure 5-16 and Figure 5-24). The effect of the anchorage of the vertical wire-mesh reinforcement was similar for the slender and squat wall panels (Figure 5-17 and Figure 5-25). The presence of the external light gauge steel provided a marginal improvement in the lateral performance of both wall panels. The slender wall experienced an increase by a factor of 1.08 in lateral strength while the squat wall 1.1 (Figure 5-18 and Figure 5-26). It became apparent that the contribution

of the external light gauge steel could provide additional contribution provided that the entire cross section was effective and properly anchored to the wall. In the analyses, and based on the design of the wall panels, only the flange contribution of the light gauge steel could be assumed to contribute.

Figure 5-28 is a drawing of the wall panel with suggested improvements in design. Note that based on the parametric results, these changes were assumed to provide the best enhancements in the lateral response for each wall. Figure 5-29 provides pushover results for both the slender and squat walls based on incorporating the changes, which includes the following: 6 mm-diameter, perfectly bonded smooth wire-mesh in the vertical direction; hooked ends for the vertical wire mesh reinforcement into the cap and base beams with 200 mm embedment length; and hooked exterior light gauges steel with an embedment length of 200 mm. Hooking of the light gauges steel is envisioned to be accomplished by extending the ends of the steel into the cap and base beams and penetrating the longitudinal reinforcement in the beams through the light gauge steel. The change in detailing allows the full cross-section of the light gauge steel to contribute to the lateral response. In the model, the area of the truss bars representing the light gauge steel increased from 133 mm^2 to 385 mm^2. The later is based on the critical cross-section of the light gauge steel that corresponds to the opening.

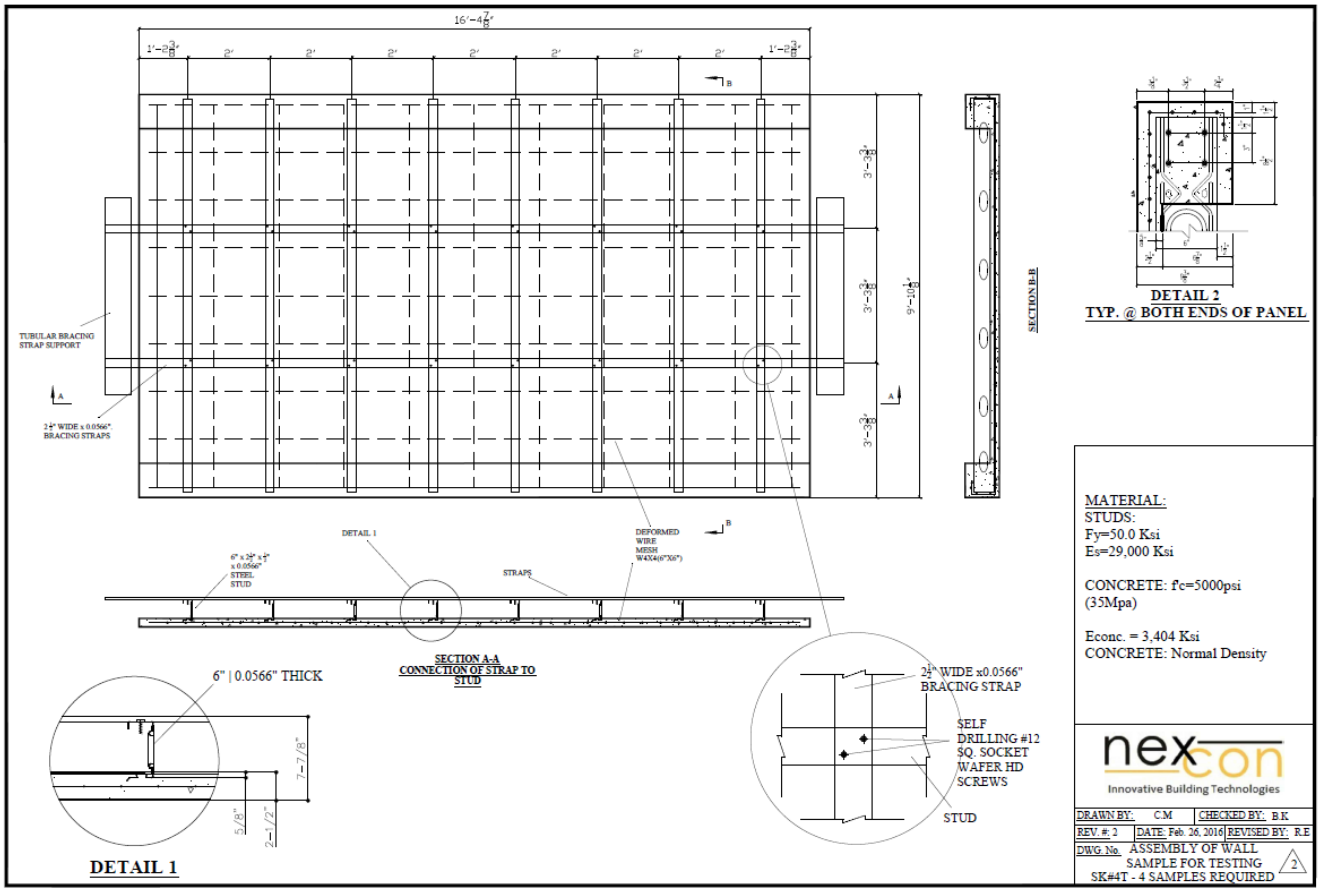

Figure 5-28 Final design drawings for the wall panel

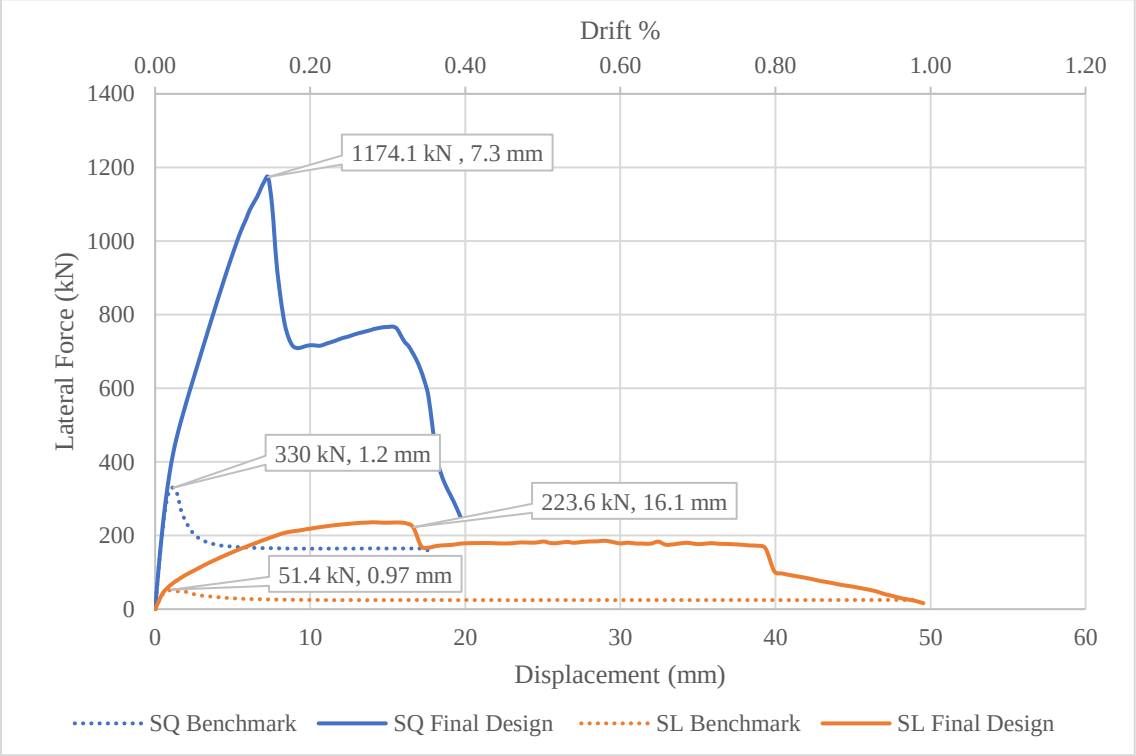

Figure 5-29 Lateral responses for slender and squat walls

The benchmark models provide a lower bound performance, while the updated models provide an upper bound provided that the required reinforcement details are implemented. The comparison confirms the fundamental difference between the squat and slender wall systems. The slender wall is more ductile than the squat wall. The maximum lateral capacity of the slender wall is significantly lower in comparison to the squat wall. The squat wall is more brittle with higher initial stiffness. The failure mode for the squat wall is dominated by sliding shear at the base of the web area of the wall, while the pattern of failure for the slender wall is controlled by flexure. The global yield displacement for the

slender and squat walls are 8.4 mm and 5.9 mm, respectively. The corresponding lateral strength at the yield displacement is 1084 kN for the squat wall and 208 kN for the slender wall. The crack pattern for the slender and squat walls are provided in Figure 5-30 and Figure 5-31, respectively. The crack patterns correspond to failure, which is defined as the displacement at which the lateral strength reduces to 80% of the maximum lateral force capacity.

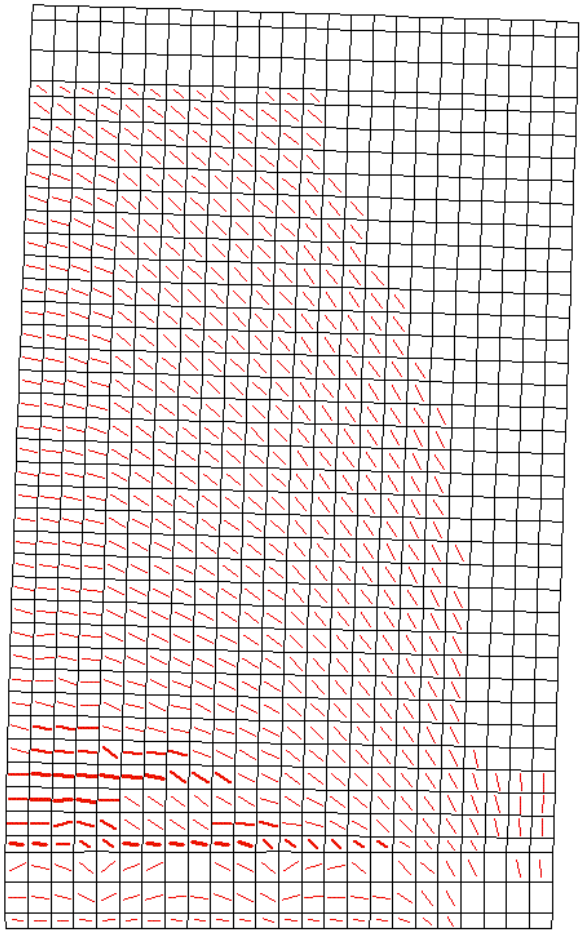

Figure 5-30 Cracking pattern for the slender wall

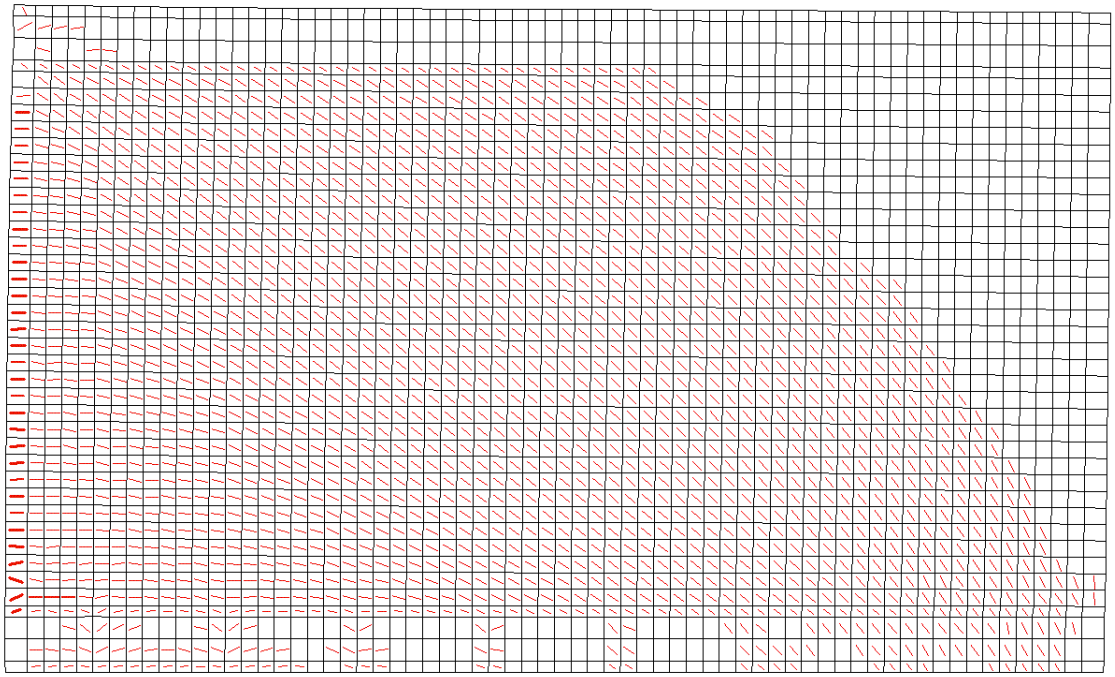

Figure 5-31 Cracking pattern for the squat wall

5.7 Final Wall Panel Design

Recommendations for final design are provided for the squat wall panel. This is based on the results of the preliminary analyses and on the direction of Burnco MFG Inc. that plans to focus on the squat wall panel for its future projects. The parametric analyses provided direction on the aspects of the wall panel that would lead to improved lateral response. Although the analyses demonstrated that deformed or fully bonded vertical wire-mesh reinforced is the most critical change in the design, Burnco has a preference for smooth wire mesh due to their availability. Furthermore, the contribution of the exterior light gauge steel was one of the main design challenges. The following provides more details regarding the internal wire mesh reinforcement and the external light gauge steel.

5.7.1 Reinforcing Bar Type

As previously discussed, smooth bars are problematic given their reduced bond to the concrete. The parametric studies demonstrated that deformed bars, which are assumed fully bonded, provide enhanced lateral performance. Fully bonded smooth bars, however, would provide a similar response. Similarly, considering the imperfect bond for deformed bars and smooth bars leads to similar results. Thus, it is critical to establish a mechanism to improve the bond of smooth bars when implemented in place of deformed bars. Figure 5-32 provides the pushover response for the squat wall with perfect and imperfect bond properties for the deformed and smooth surface options for the wire-mesh reinforcement.

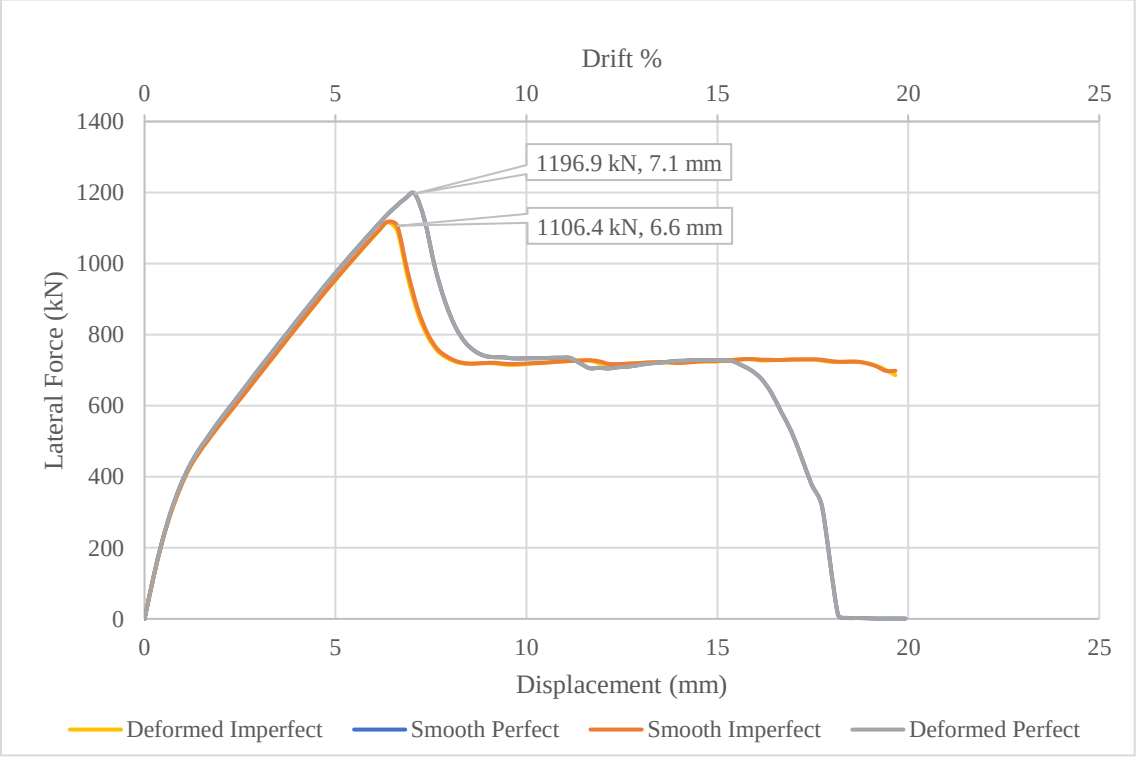

Figure 5-32 Models with smooth and deformed bars with imperfect and perfect bond

Figure 5-32 provides the results for four models. The models cover any combinations of smooth and deformed vertical wire mesh from the perfect bond to imperfect bond and with end hooks into the cap and beam beams. The response in blue (exact response to the grey curve) corresponds to smooth bars with perfect bonding. The response in orange provides the results of the model with smooth wire-mesh reinforcement with imperfect bonding known as the benchmark of the final design. The lateral response for deformed reinforcement with imperfect bonding is provided by the curve in yellow (exact response to orange curve), and the grey line represents the deformed wire-mesh reinforcing with perfect bonding between reinforcement and surrounding concrete. The walls with perfect bonding of the vertical wire mesh reinforcement provide better performance than the walls with imperfect bonding whether the bars are smooth or deformed. Note that the analyses in Figure 5-32 assume end hooks for all four models, leading to marginal differences in the responses.

The influence of ends hooks implemented in the vertical wire-mesh reinforcement in the final design is illustrated in Figure 5-33. The deformed wire-mesh option has not been considered in this analysis since Burnco MFG has a preference for smooth wire-mesh.

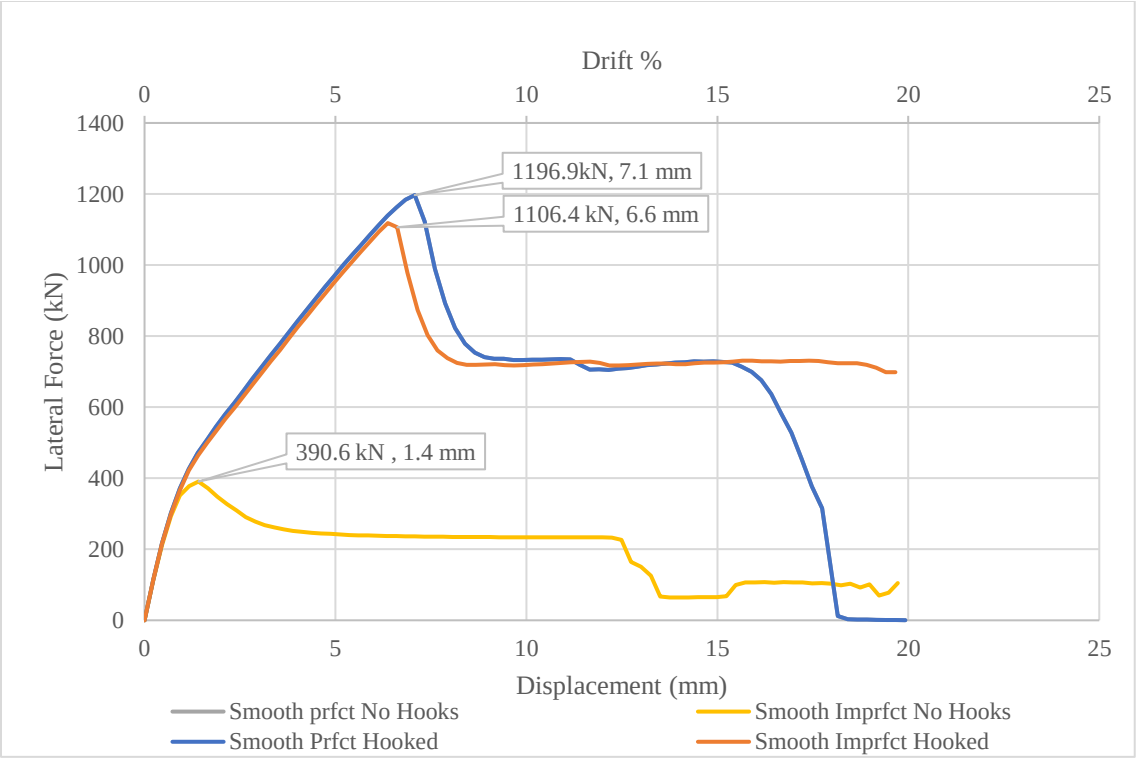

Figure 5-33 Models with and without end hooks

The response in blue corresponds to the result for the wall with the perfect bonding of the vertical smooth wire mesh with end hooks. The response in grey (identical to blue) provides the result for the wall with smooth bars that are perfectly bonded but without hooks at the ends. For comparison, the response in orange corresponds to the results for the model with imperfect smooth bars and with end hooks. The last response in yellow corresponds to imperfect bonding between the vertical wire mesh and concrete and no hooks at either of the ends. These results clearly illustrate that improving the bond, either by considering the perfect bond or providing end hooks improves the lateral response of the wall. Therefore, if the bars can be hooked into the cap and base beams, then the surface texture (smooth or

deformed) is not critical. Typically, smooth bars are reasonably assumed to be imperfectly bonded to the concrete. However, for the wall panels considered herein, the internal reinforcement is based on a mat of wire mesh reinforcement. Considering that the horizontal and vertical wire mesh is welded at their joints, and the spacing of the bars is 150 mm in both directions, an assumption can be made that the bars are being provided with sufficient restraint to achieve a fully bonded response. The only other consideration would be to ensure that the vertical wire mesh has sufficient embedment length into the cap and base beams to ensuring yielding.

5.7.2 Contribution of Light Gauge Steel

As illustrated in Figure 5-27 the wall with the full input of the light gauge steel provides better performance. The wall experienced a greater lateral load resistance at approximately the same lateral displacement in comparison to the model without the exterior steel. Also, higher lateral load resistance achieved with the full cross-sectional area of exterior steel contributing in comparison to the flange-only contribution. Based on these results, it was suggested to improve the detailing of the wall panel to engage the entire cross-sectional area of the light gauge steel. To capture the total contribution of the steel, they need to be embedded into the cap and base beams such that the longitudinal

5.8 Summary of Final Design

Based on a review of the current design and the preliminary analyses, modifications to the design of the wall panel were suggested. For the internal vertical reinforcing bars and the

external light-gauge steel, longer embedment depths into the cap and bottom beams are suggested. Also, end hooks were suggested for the internal vertical bars. The hooks are intended to improve the anchorage of the vertical bars, specifically at the base of the wall where the critical section is located.

Furthermore, the extended embedment length of the external steel was perforated to permit longitudinal reinforcing bars of the cap and base beams to pass through. This was intended to provide additional anchorage for the steel to improve the composite action between the steel and thin concrete panel. Figure 5-34 provides the modified design, illustrating the extension of the exterior steel into the cap and base beams. The cap and base beams remained square (250 mm wide and 250 mm high). The longitudinal reinforcement in the beams did not change and consisted of 4-15M bars with 75 mm of concrete cover from both edges of the beams. The cover for the external steel to the top of the beam is 50 mm based on the preliminary suggested design by Burnco. 10M stirrups were used in the beams at a spacing of 300 mm. All reinforcing steel is compatible with Canadian Standard CSA-G30.18-09. Based on material testing conducted by Burnco, the ultimate strength of the 15M reinforcing steel is approximately 525 MPa and the yield strength is 400MPa. The internally welded wire-mesh used to reinforce the thin concrete panel consists of a 6” x 6” (150 mm x 150 mm). The wires used to fabricate the wire-mesh is compatible with Canadian Standard CSA-G30.18-09. The diameter of the wires is 6 mm, and the surface is smooth. A single layer of meshing has been used for this system and is placed at the middle

of the wall. The wires are welded to each other at each intersectional node. The smooth surface of the wires may affect the bonding to the surrounding concrete.

Given that the horizontal and vertical wires are welded to each other at 150 mm intervals, the bond length is assumed to correspond to this length. Thus, the wire mesh, for analysis purposes, is assumed to be fully bonded to the concrete. In other words, the intersection and welding of the wires promote an anchorage, which improves the bond to the concrete. The final size of the wall system panel is 5000 mm in length by 3000 mm in height.

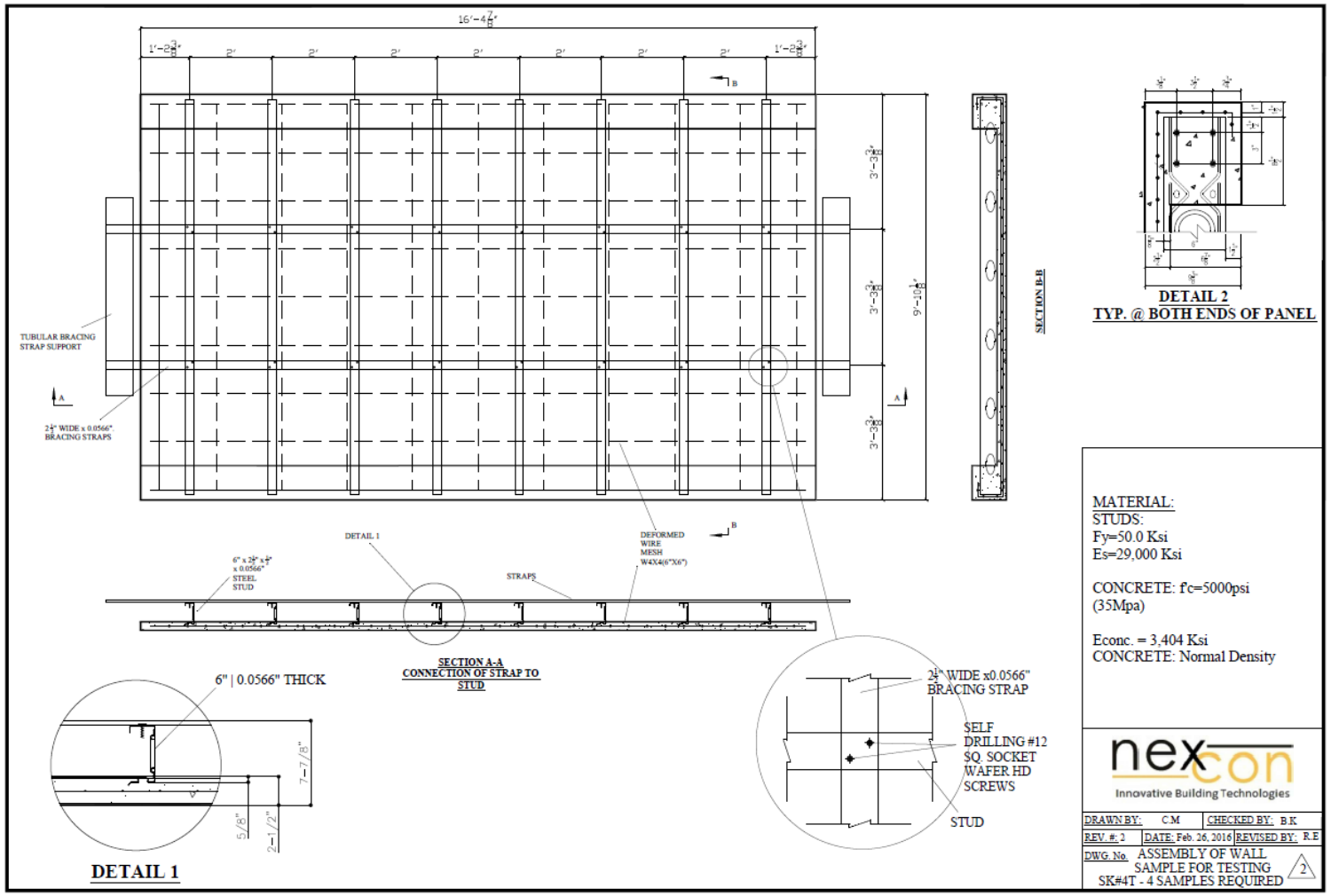

Figure 5-34 Final design drawing based on parametric analyses (Karimi, 2016)

As illustrated in Figure 5-34, the external steel were embedded 200 mm into the cap and base beams. The thickness of the concrete section is 65 mm, and the compressive strength of the concrete is reported to be approximately 25 MPa of normal density concrete. A 0.5 water-cement ratio is specified with an air content of 5-6%. Super-plasticizer is used to improve the flow of the concrete in the thin section. The same concrete is used for the cap and base beams.

Chapter 6 Detailed Numerical Analysis

Chapter 5 provided comprehensive parametric analyses of the proposed Thin Shell Panel (TSP). Based on those analyses, suggestions were provided to improve the wall system with regards to lateral performance. The most significant improvement is based on improving the bond between the vertical component of the internal wire-mesh reinforcement and the external light-gauge steel to the thin concrete panel. In addition, continuity of the vertical wire mesh bars into the cap and base beams were suggested. The contribution of the exterior light gauge steel was determined to be beneficial to the lateral performance of the wall system, specifically when the full contribution of the cross-section is engaged. By extending the light gauge steel into the cap and base beams and having the longitudinal reinforcing steel in the beams penetrate through the light gauge steel was deemed to provide the proper anchorage to engage the full contribution of the cross-sectional area of the light gauge steel.

6.1 Final Wall Design

Figure 6-1 illustrates the final design of the squat wall panel.

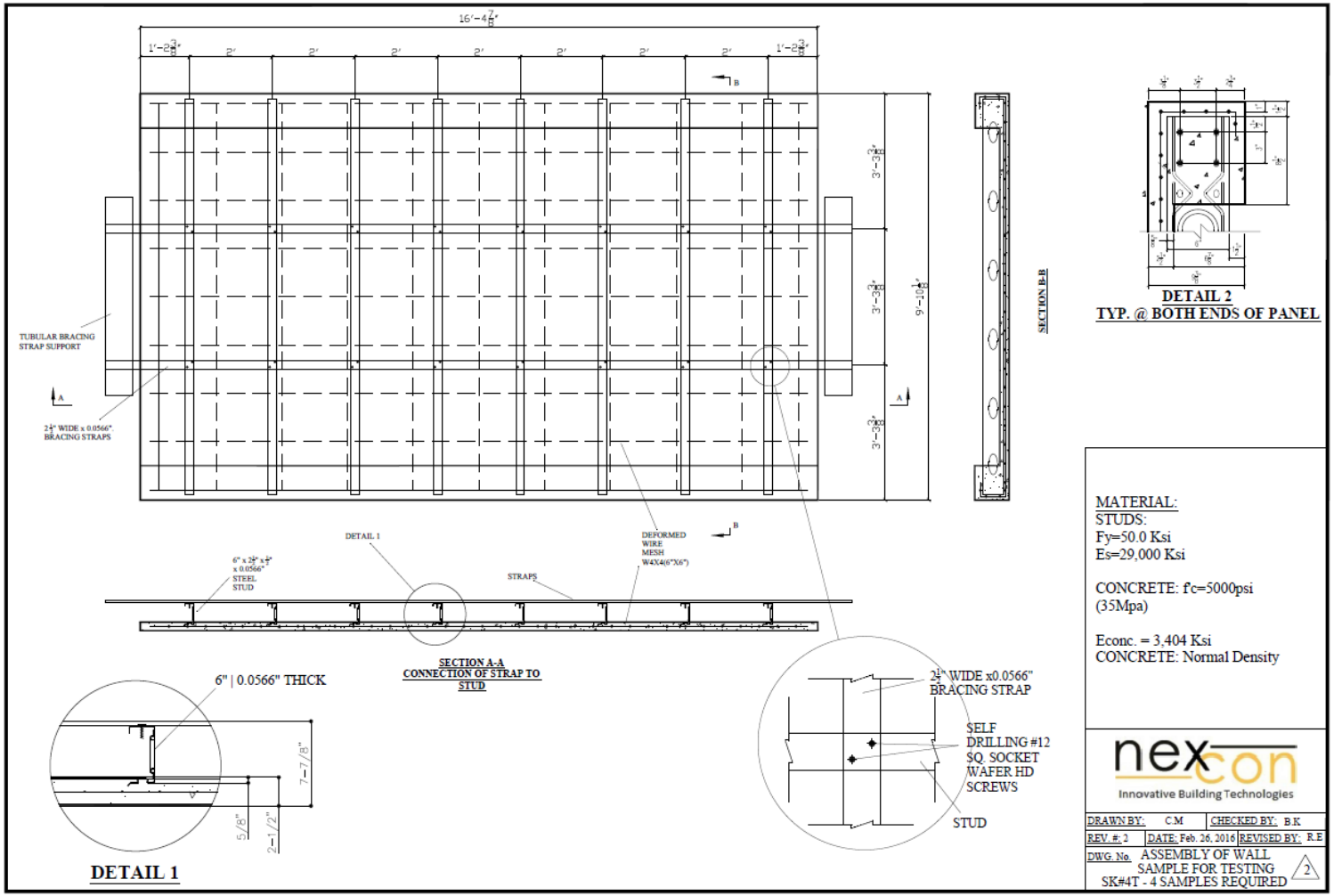

Figure 6-1 Final squat wall panel design (Karimi, 2016)

Figure 6-2 shows a vertical section of the wall panel with the suggested changes implemented. The sectional drawing is an enlarged view of Section B-B provided in Figure 6-1.

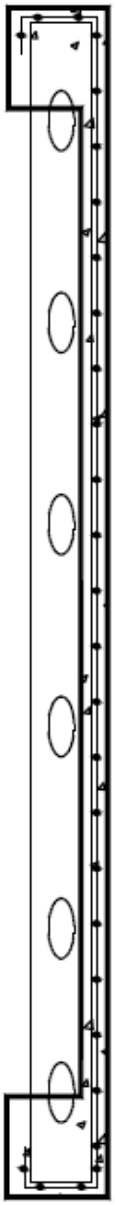

Figure 6-2 Cross-section of the final wall panel design (Karimi, 2016)

As depicted in Figure 6-3, the vertical components of the internal wire-mesh reinforcement are extended in the beams up to the concrete cover. In addition, the bars are hooked within

both the cap and base beams. The exterior light gauge steel studs are also extended into the beams such that the longitudinal reinforcement of the beams can penetrate through. Recall that this is implemented in an attempt to fully engage the entire section of the light gauge steel during in-plane lateral loading.

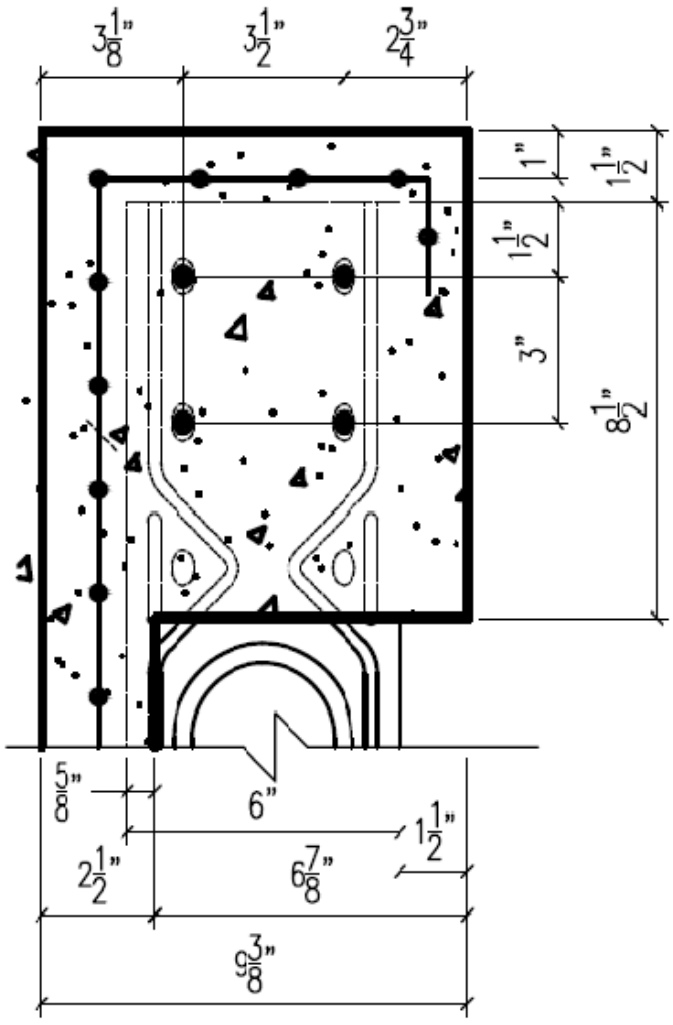

Figure 6-3 Typical beam details for final wall design (Karimi, 2016)

The finite element model representing the final squat wall design for analysis in VecTor2 is illustrated in Figure 6-4. The panel is 5000 mm long and 3000 mm high with an aspect ratio of 0.6. The smooth 6 mm-diameter internal wire-mesh reinforcement are denoted by the blue truss bars. The spacing between the horizontal and vertical components is 150 mm. The vertical components of the wire mesh are embedded 200 mm into the cap and base beams. The concrete cover in the beams is 50 mm.

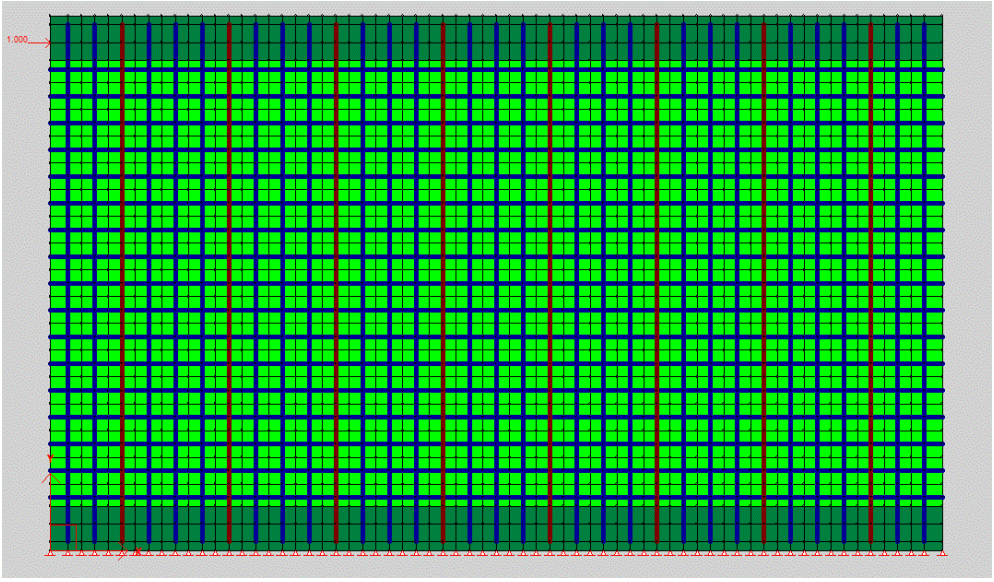

Figure 6-4 Finite element model for final squat wall design

The horizontal components of the wire-mesh are extended to the edges of the panel. The concrete cover is 100 mm which is the distance between the edge of the wall to the first vertical reinforcement. The spacing of the external light gauge steel studs (depicted by the red truss bars) is 600 mm. The depth of the cap and base beams are 250 mm, with cross-section dimensions of 250 mm by 250 mm. The external studs are embedded approximately 200 mm into the beams. The light gauge studs are penetrated by the 4-15M longitudinal

reinforcing bars in the cap and base beams. Note that the vertical and horizontal bars of the wire mesh are welded at their intersection. Given this and the 150 mm spacing of the mesh, it was reasonably assumed that the bars are fully bonded to the concrete. The thickness of the wall panel is 65 mm and is denoted by the light green rectangular concrete elements in Figure 6-4. The models consist of 5320 total elements. Of this, 2680 are truss bar elements, while the concrete rectangular element accounts for the remaining 2640 elements. The total number of nodes is 2747. The location of the truss bar elements has been modified to eliminate the requirement of concrete triangular elements. Figure 6-5 illustrates the model without any modifications. The generated elements between the vertical wire mesh reinforcement and the exterior steel studs are small and do not represent the real performance of the material at those locations.

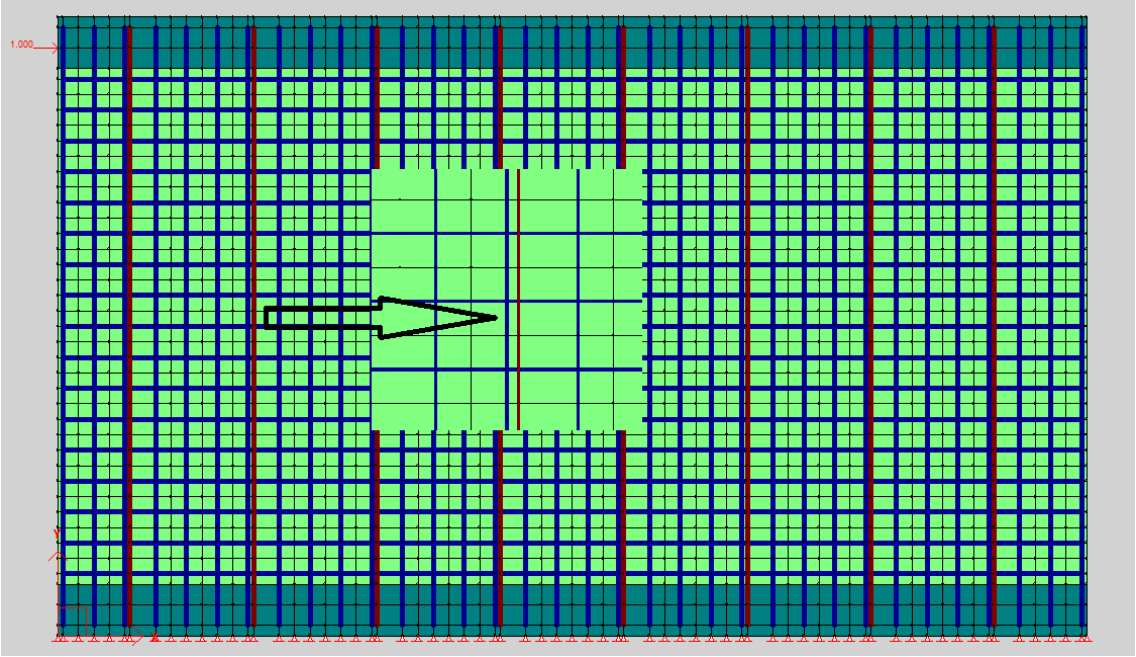

Figure 6-5 Squat panel model without size modifications

6.2 Material Properties

The material properties were provided by Burnco MFG. The compressive strength of the concrete was 25 MPa. The water-cement ratio is 0.5 and the specified content specified is 5% to 6%. The initial tangent elastic modulus is reported as 23470 MPa. The tensile strength of the 6 mm-diameter welded wire-mesh, 15M longitudinal bars in the beams and external light gauge steel are provided in Table 6-1.

Table 6-1 Reinforcing material properties for Thin Shell Panel (TSP)

Reinforcing	Cross-Sectional Area (mm^2)	Yield Strength (MPa)	Ultimate Strength (MPa)	Elastic Modulus (MPa)	Strain Hardening Strain (me)
15M bars	200	400	600	200000	10
6 mm bars	64	485	600	200000	10
Light gauge steel	386	358	448	200000	10
10 M Stirrups	100	400	600	200000	10

6.3 Finite Element Model

The finite element model developed for analysis with VecTor2 is provided in Figure 6-4. The element size for the web is 100 mm in the horizontal direction (horizontal) and 75 mm in the vertical direction. The element size for the cap and base beams is 100 mm in the horizontal direction and 100 mm in the vertical direction. Vertical and horizontal restraints are specified along all the nodes at the bottom of the base beam to develop fixity. The applied support displacement (lateral load) is placed near the mid-height of the cap beam at the left edge. The finite element model was subjected to both monotonic (pushover) loading and reverse cyclic loading. For concrete modelling, the Hognestad compression pre-peak model was selected; this model is suitable for normal strength concrete with a strength of less than 40 MPa. The Modified Park-Kent model was chosen for the compression post-peak model. This model is ideal for a structure with any amount of confinement. The Compression softening was captured by the Vecchio 1992 model. This

model considers the compression softening due to co-existing tensile straining based on statistical analysis of numerous panels tested at the University of Toronto. The tension stiffening and tension softening phenomenon are modeled by the 2003 Bentz and bilinear models, respectively. These models consider the influences of reinforcement ratio and bond characteristics in establishing the tensile stress in the concrete post-cracking. Other models for the reinforcement and bond are discussed in detail in Chapter 5. The complete list of the concrete models is provided in Table 5-7 and Table 5-8, while Table 5-9 provides a list of the models for the reinforcement.

6.4 Monotonic Analysis Results

The results from a VecTor2 analysis can be retrieved from Augustus, the post-processing software for Vector2. Augustus is an advanced graphical-based post-processor. It offers comprehensive post-analysis visualizations of global and local load-deformation responses, element stresses and strains, and deflection and crack patterns. The load stage-load factor relationship for the monotonic analysis is depicted in Figure 6-6. The load case is utilized to impose a lateral support displacement of 1 mm, which was placed at a specified node near the mid-height of the cap beam. The load factor is increased incrementally to the end of the analysis or the final factor that is specified. For the monotonic analysis, an increment factor of 0.25 is selected. The increment factor is applied to the specified lateral displacement. Thus, the displacements increase by 0.25 mm at each load stage. Figure 6-6 illustrates the loading protocol for the monotonic analysis.

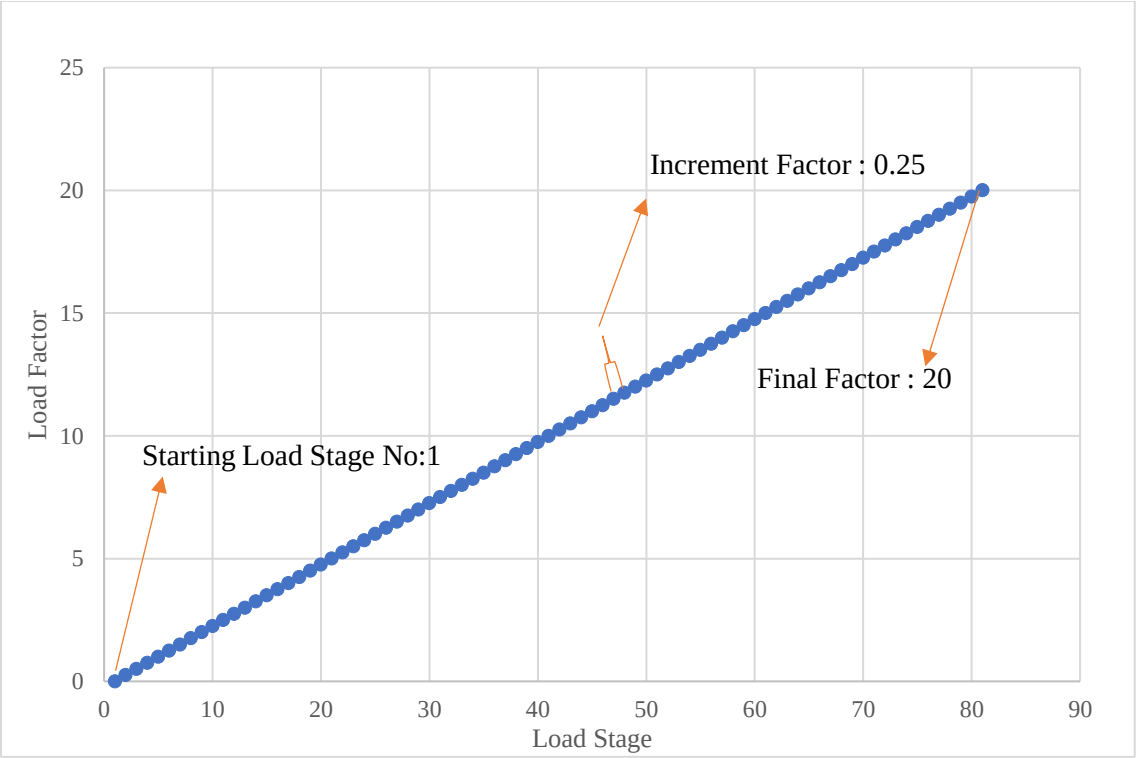

Figure 6-6 Monotonic loading protocol

As illustrated in Figure 6-6 the initial factor for the analysis is 0, and the total number of load stages is 81 if the increment factor is 0.25 and the final factor is 20.

The intent of the analysis is to determine the load-displacement response under lateral loading and to establish important response parameters. One of those performances is the ductility of the panel. Ductility is a measure of the ability of a structure to undergo deformations in the inelastic range without failure (R.Park, 1989). Ductility can be based on displacement, rotation and curvature. The displacement ductility (μ) is often selected to evaluate response as it is related to the ductility-related force reduction factor used in seismic design. The displacement ductility is calculated as follows:

$$\mu = \frac{\Delta_{max}}{\Delta_Y} \quad \textbf{(6-1)}$$

Where Δ_{max} is maximum displacement and Δ_Y is the displacement at yield. The ductility-related force reduction factor in Canadian seismic design practice ranges from 1-5, where 1 assumed fully elastic response.

When calculating the displacement ductility, establishing the yield displacement can be challenging since the yield point may not be well defined for systems that deviate from the ideal elastic-perfectly plastic behaviour. In addition, for systems such as the Thin Shell Panel with a composite section of different materials, establishing the yield point is more challenging. This is due to the nonlinear behaviour and the onset of yielding at different displacement for the different component materials. To address this, Figure 6-7 shows is used to select a definition for yield displacement. Four options are possible:

Figure 6-7 (a): The displacement corresponding to first yielding of the reinforcement.Figure 6-7 (b): The yield displacement based on the equivalent elasto-plastic system with the same elastic stiffness and ultimate load

Figure 6-7 (c): The yield displacement of the equivalent elasto-plastic system with the same energy absorption

Figure 6-7 (d): The displacement of the equivalent elasto-plastic system with reduced stiffness based on the secant stiffness at either first yield or at 75% of the ultimate lateral load, whichever is less

For this study, the definition provided in Figure 6-7 (d) is selected.

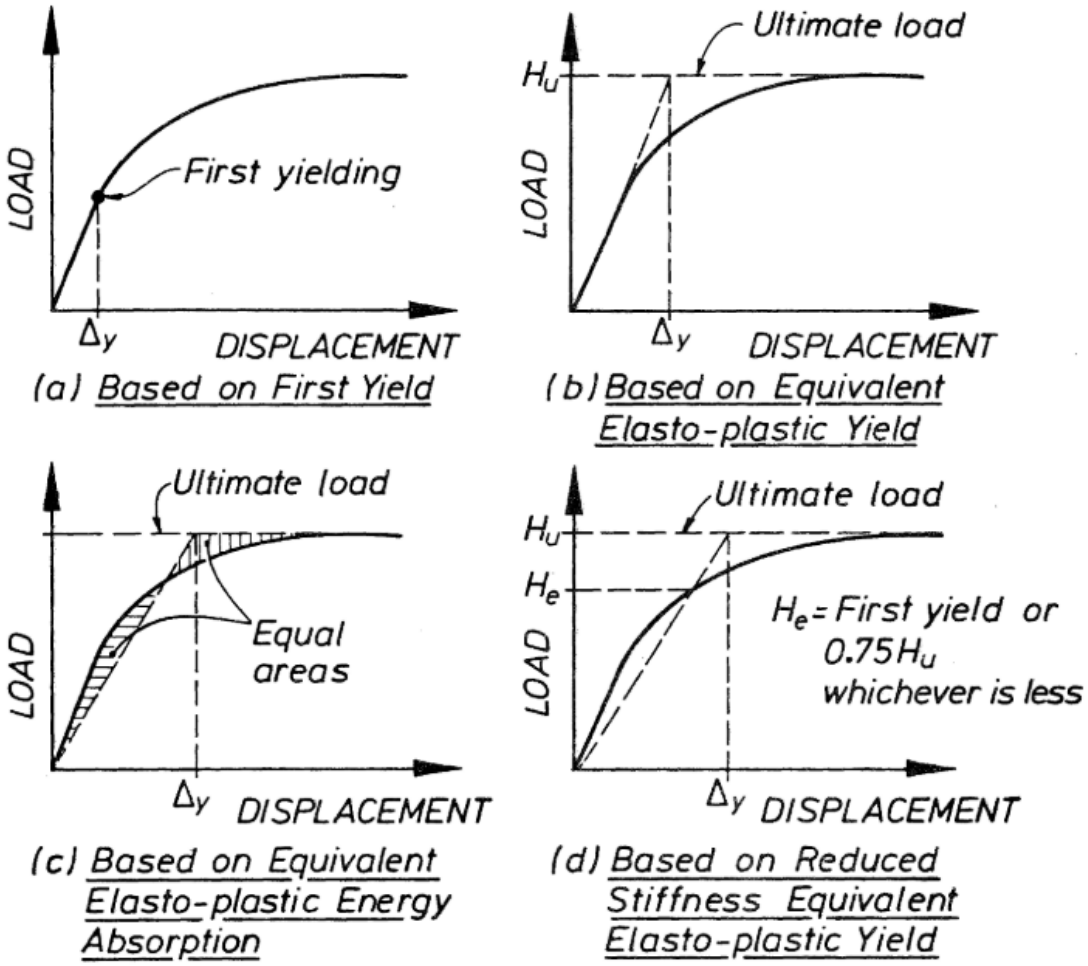

Figure 6-7 Definitions for yield displacement (R.Park, 1989)

Equation (6-1) also requires the maximum (ultimate) displacement to calculate the ductility of the system. Due to the nonlinear behaviour of structural systems, a number of definitions can be reasonably used to establish the maximum displacement as illustrated in Figure 6-8.

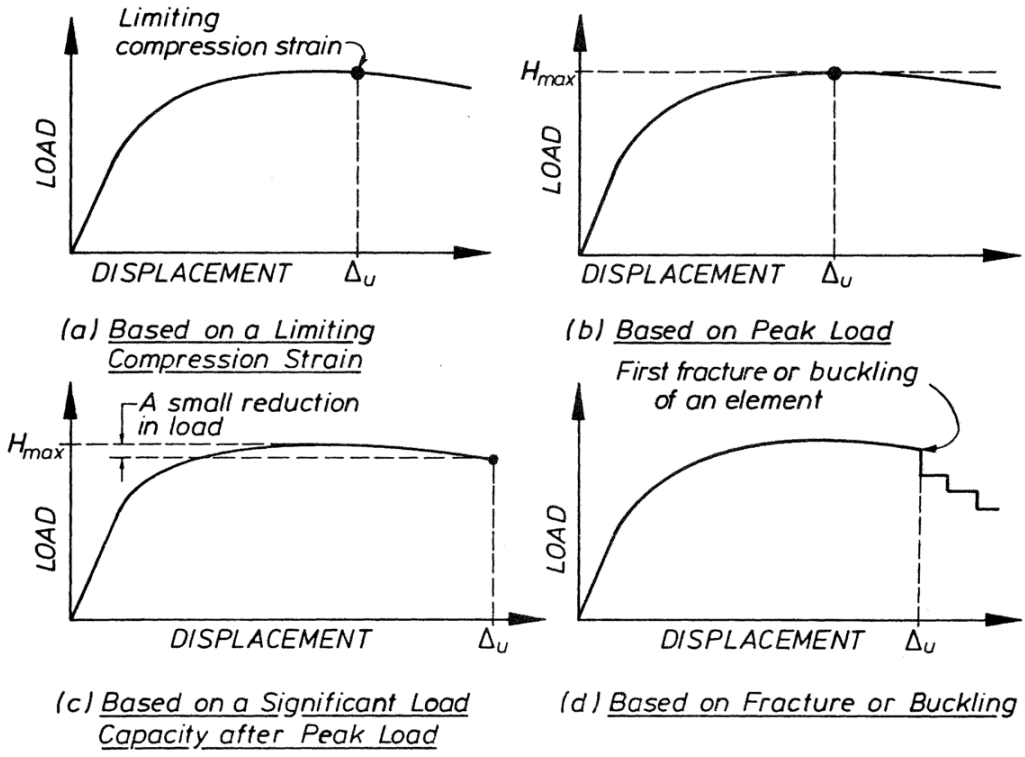

Figure 6-8 Definitions for ultimate displacement (R.Park, 1989)

Four definitions are suggested in Figure 6-8:

Figure 6-8 (a): The displacement corresponding to the limiting compressive strain

Figure 6-8 (b): The displacement corresponding to the peak lateral load.

Figure 6-7 (c): The displacement corresponding to a 20% reduction in the lateral load capacity in the post-peak response

Figure 6-8 (d): The displacement corresponding to buckling or fracture.

For this study, the definitions related to Figure 6-8 (c) or Figure 6-8 (d) were used, whichever occurs first.

The lateral load-displacement response for the final design is provided in Figure 6-9. Noted are response parameters based on Equation 6-1 and the definitions selected for the yield and ultimate displacements.

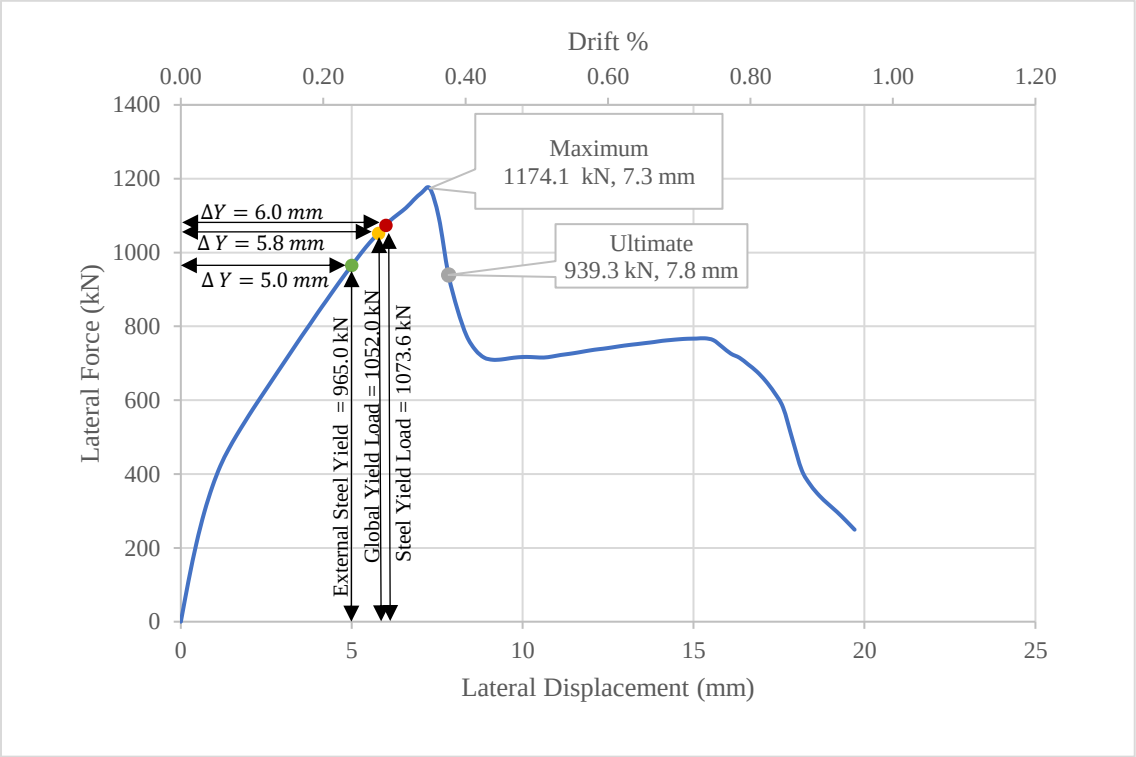

Figure 6-9 Lateral load-displacement response for final squat wall design

Additional data and calculations are available in Appendix A and Appendix B. Based on the calculation, yield points, maximum lateral load, and the ultimate displacement are provided on the graph. The first yield of the reinforcement is also noted on the response. Recall that the yield strength for the welded wire-mesh is 485 MPa. The first yield of the external light gauge steel was captured at 5.0 mm of displacement and corresponding lateral load of 965 kN. The first yield of the internal vertical bars of the wire-mesh

reinforcement was recorded at 6.0 mm of lateral displacement and a corresponding lateral load of 1073.6 kN. The calculated global yield was 5.8 mm displacement with 1052.0 kN of lateral force. In this study, the global yield point is chosen to determine the displacement ductility. This is based on the global yield point lying between first yielding of the external light gauge steel and internal wire-mesh reinforcement. Furthermore, it is very similar to the first yielding of the internal wire-mesh reinforcement. Figure 6-10 shows the average stresses the reinforcement modelled with truss bars (wire-mesh and light gauge steel). The vertical bar of the internal wire-mesh-reinforcement near the edge of the wall on the left side and at the base of the wall panel reached the yield strength capacity of 485 MPa.

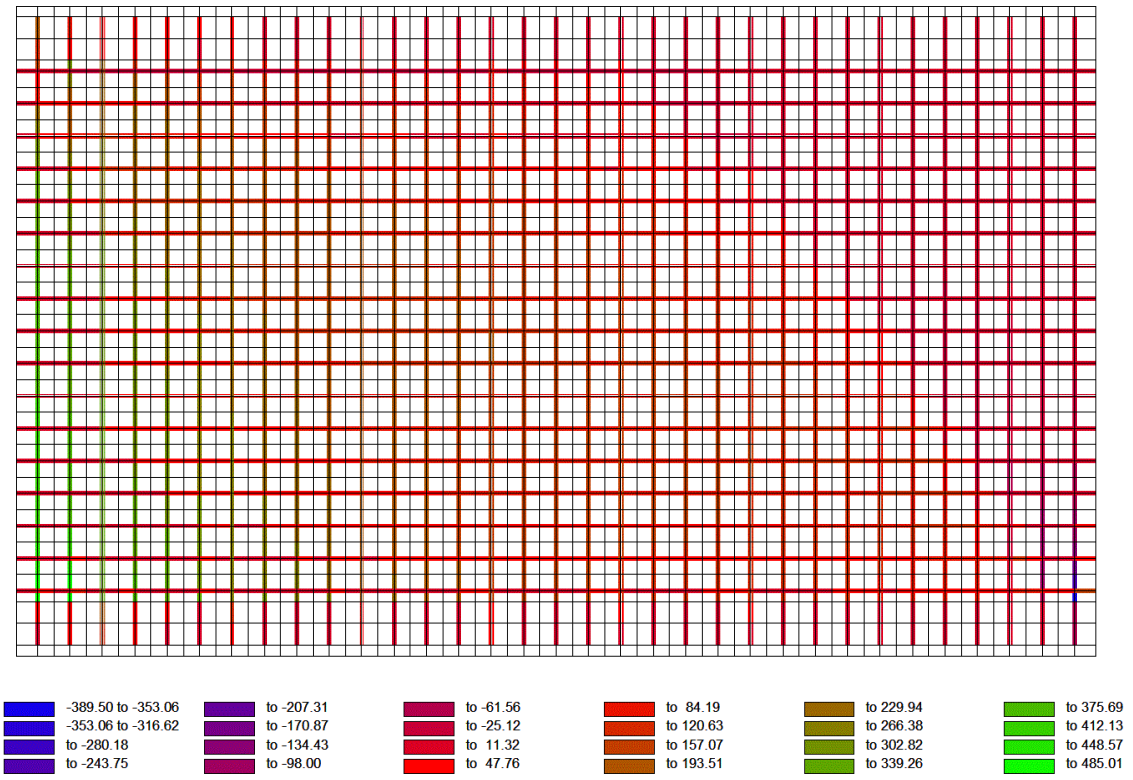

Figure 6-10 Average truss bars stress at first reinforcement yielding

Figure 6-11 provides the average truss stresses at the maximum lateral load capacity. The green colouring of each reinforcement indicates that reinforcement has neither yield or is close to yielding. The vertical reinforcement at the left edge of the panel and towards the bottom of the panel have reached the yield stress at the peak lateral load. This includes the two vertical wire-mesh bars and one external light gauge steel.

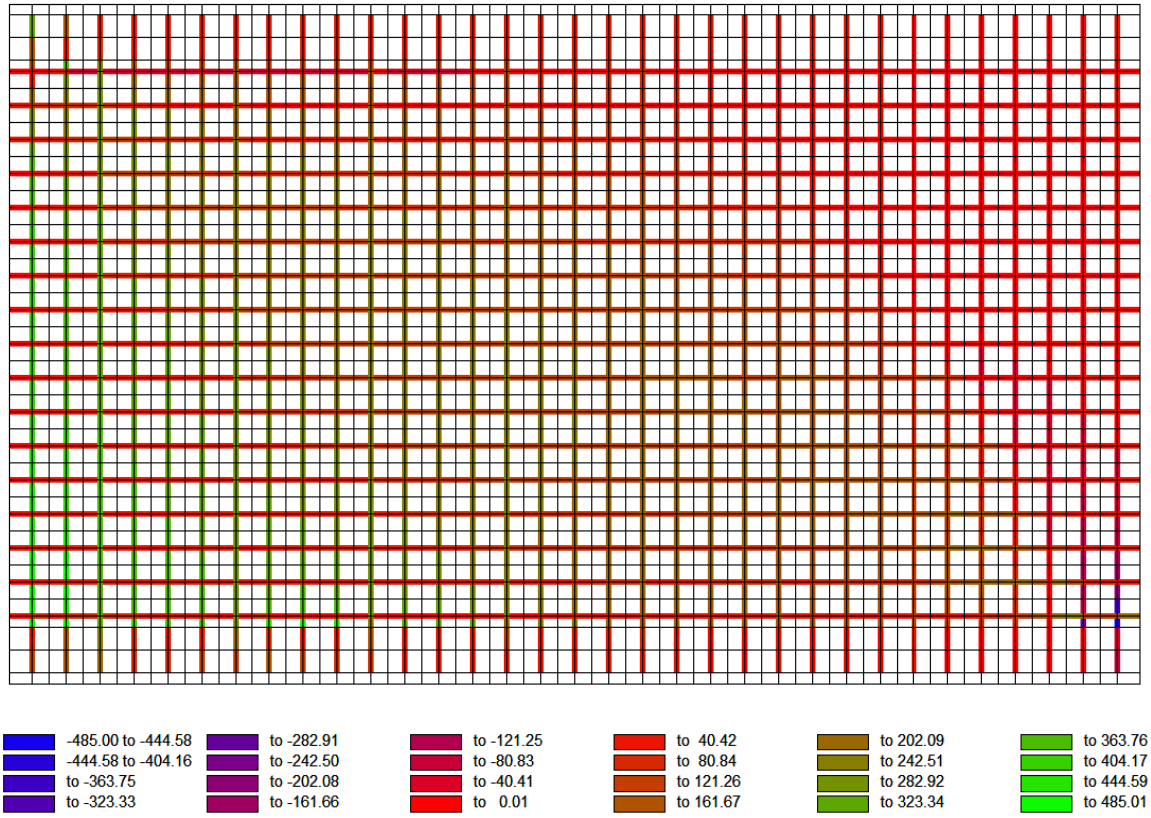

Figure 6-11 Average truss bar stress at the maximum lateral load capacity

At the maximum lateral load, a number of vertical mesh bars and light gauge steel reached their reported yield strength, while the horizontal reinforcement remained in the elastic range. In addition, a small segment of a vertical wire mesh bar at the bottom of the wall panel at the right edge reached the compression yield capacity. While it is reasonable to assume that the vertical wire mesh bars would be able to sustain yielding in compression, given the lack of confining reinforcing, only a small bar segment had yielded. Thus, the lateral load response from the analysis is reasonable.

Figure 6-12 provides the average truss bar stresses at the point of failure, which is assumed to coincide with a 20% drop in the lateral load capacity from the maximum as suggested by Park (1988). Three vertical wire mesh bars and two light gauge steel studs were yielding at this stage in the response. In addition, one of the horizontal wire-mesh bars near the right edge of the wall panel adjacent to the base beam also attained its yield capacity. Sliding of the wall panel surfaced at the location where the horizontal wire-mesh bars were yielding.

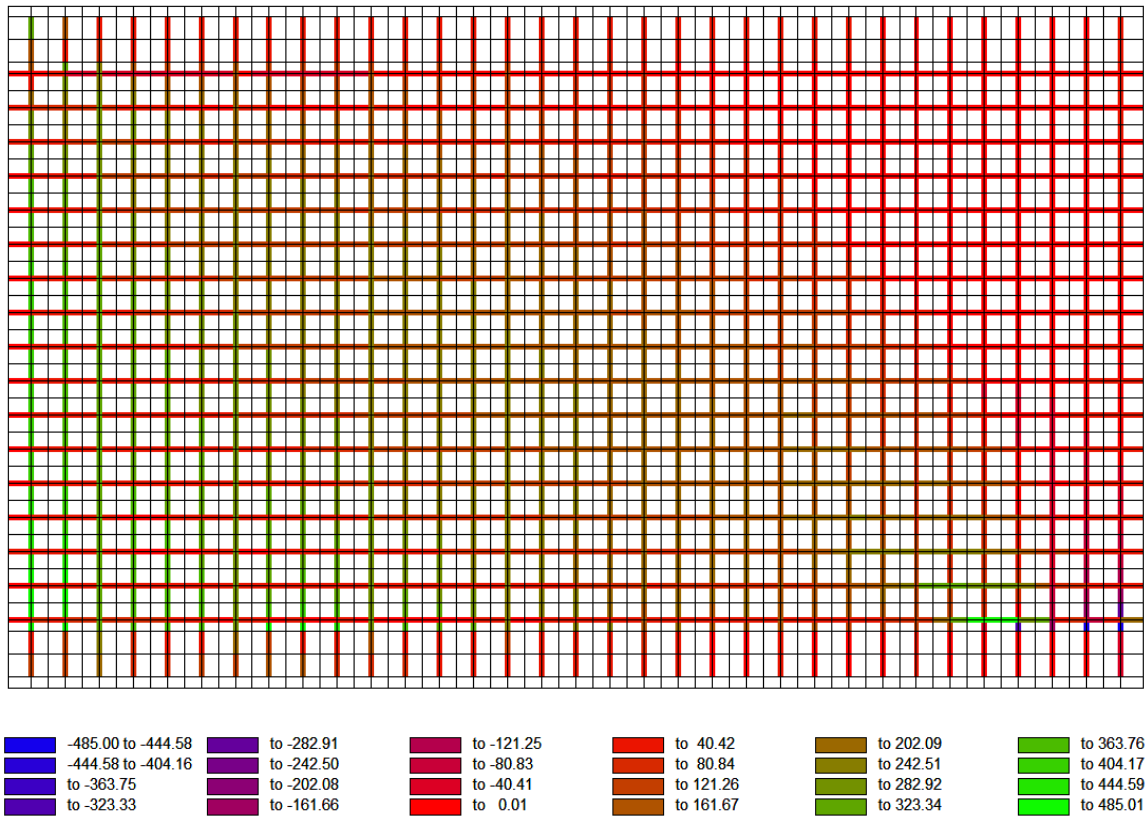

Figure 6-12 Average truss bar stress at failure

As noted in Figure 6-9, the first yield of the reinforcement was captured at 6.0 mm of displacement and 1073.6 kN of lateral force. The calculated global yield corresponds to 5.8 mm of displacement and 1052.0 kN of lateral force. The 20% reduction from the maximum lateral load is considered as the ultimate strength, which occurred at 7.8 mm of displacement and 939.3 kN.

The ductility capacity as defined in Equation 6-1 provides the following displacement ductility for the wall panel:

$$\frac{\Delta Ultimate}{\Delta Y} = \frac{7.8\ mm}{5.8\ mm} = 1.34$$

The first yield was captured in the internal wire-mesh reinforcement at the first vertical reinforcement 100 mm from the left edge of the wall and the second vertical reinforcement located 250 mm from the left edge of the wall. The light gauge steel yielded prior to the vertical reinforcement at the location of the first light gauge steel from the left edge of the wall (400 mm into the wall) at a displacement of 5 mm. The compression stress in the concrete exceeded the 25 MPa specified strength of the concrete at the right toe of the wall. The overstrength of the panel system is another important response parameter. The

overstrength is defined as the maximum lateral load capacity to the yield capacity. The yield and maximum lateral load capacities are illustrated in Figure 6-13.

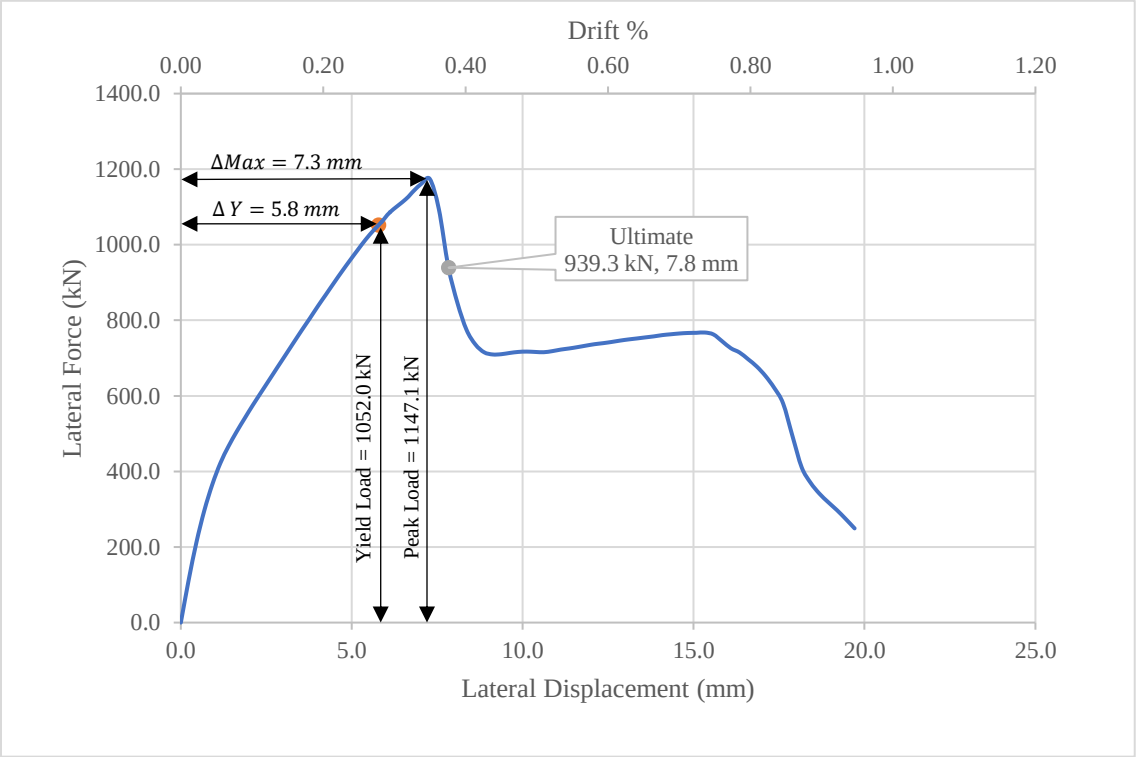

Figure 6-13 Lateral loads and displacement corresponding to yield and peak response

The drift capacity is typically used is provide a measure of the displacement capacity of a structural system. Equation 6-2 illustrates how the drift is determined.

$$Drift\ \% = \frac{\Delta}{h_w} \times 100 \qquad \textbf{(6-2)}$$

Where Δ is the displacement at the top of the wall panel and *hw* is the height of the wall. Drift corresponding to the global yield point, maximum lateral load capacity and ultimate point are 0.20, 0.26, and 0.27, respectively.

The cracking pattern in the panel at different stages in the loading provides a visual representation of the prevailing behaviour and controlling mechanisms. The post-processor Augustus that was specifically formulated to use with VecTor2 provides the full range of information for cracking in each element. This includes the crack width. In addition, the strains and nodal displacements for each element can be retrieved. The figures that follow illustrate the combined view of the cracking pattern and the displaced shape of the panel corresponding to the first yield of the reinforcement, the maximum lateral load, and the ultimate point. The ultimate point coincides with shear sliding of the wall panel.

Figure 6-14 provides the cracking pattern and displaced shape at first yield.

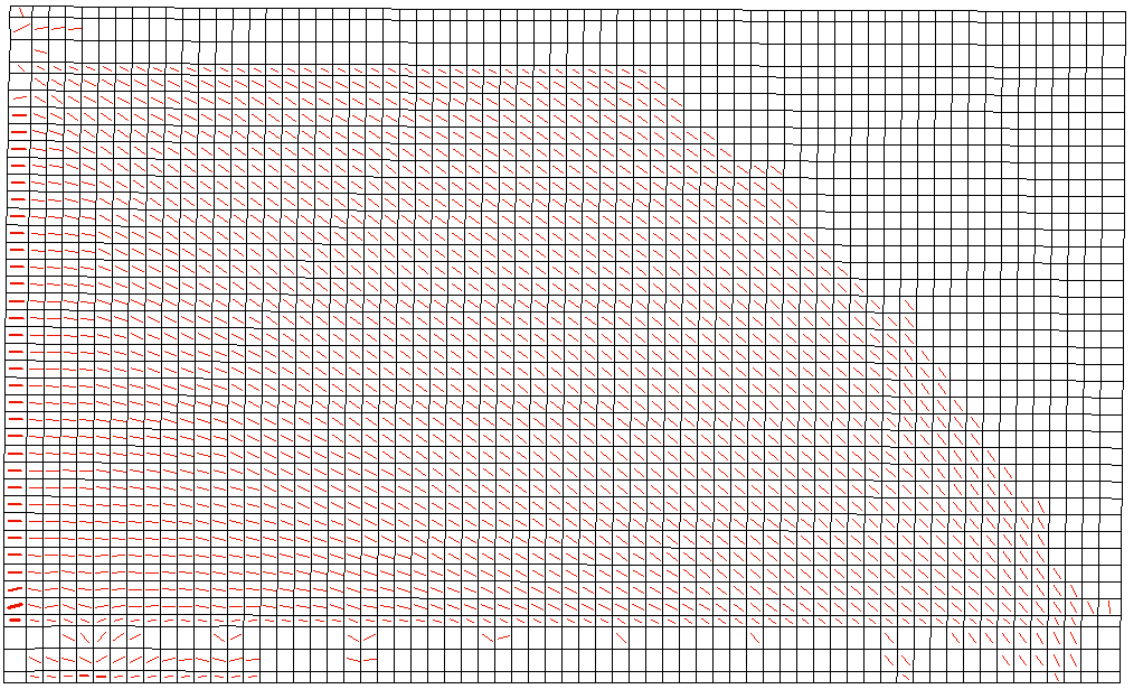

Figure 6-14 Cracking patterns and displaced shape at first yield

The more prominent cracks surfaced at the left edge of the panel due to the tensile stresses that exist from the lateral loading. The larger cracks are mainly concentrated towards the bottom of the panel. The crack width, at this stage in the loading, was 2.6 mm just above the base beam. At 2555 mm above the base of the wall, the crack width was 1.57 mm. These larger crack widths surfaced at the edge of the wall within the 100 mm concrete cover. The average width of the cracks within the concrete cover was 2.36 mm. The concrete cover exceeded the minimum normally prescribed by code and permitted easily alignment with the vertical wire-mesh reinforcement in the model. The width of the cracks adjacent to the first internal vertical reinforcement is less substantially smaller than that within the concrete cover. The crack widths near the first vertical reinforcement varied from 0.1 mm to 0.8 mm from the height of 2555 mm from the base of the beam to just above the base beam (300 mm from bottom), respectively. Although cracking is shown at the location of the lateral load in the cap beam, the widths were negligible. Minor cracking surfaced within the base beam adjacent to the location of the external light gauge steel. The maximum crack width captured was 1.2 mm at the height of 50 mm from the bottom of the beam, corresponding to the concrete cover area. As this loading stage, a number of elements indicate cracking; however, for the majority of these elements, the crack width was less than 0.2 mm.

Figure 6-15 illustrates the cracking pattern at the peak lateral load capacity. The pattern is similar to that captured at first yield. The maximum crack width of 7.2 mm was noted at the left edge of the panel adjacent to the base beam (450 mm from the bottom of the beam)

and within the concrete cover. The average crack width for the panel at the peak was 3.52 mm. The majority of crack widths varied from 2.8 mm to 4.8 mm. The crack size at the maximum lateral load increased by 49% in comparison to the average crack width at first yield.

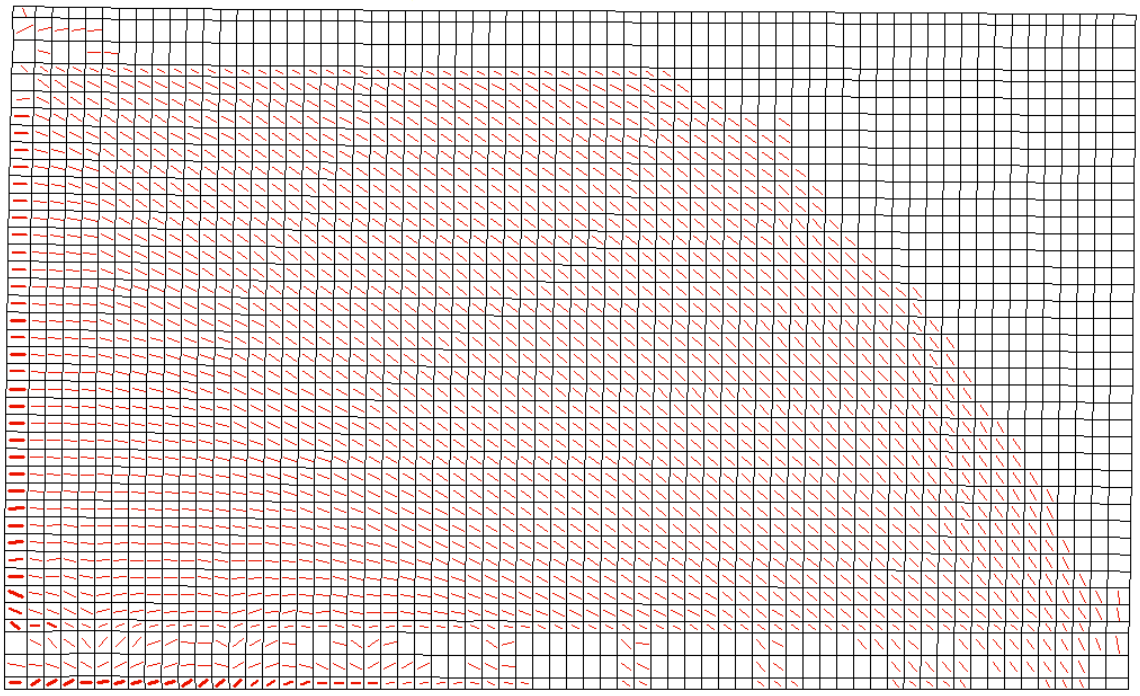

Figure 6-15 Cracking patterns and displaced shape at the maximum lateral load

The crack pattern at ultimate is shown in Figure 6-16. The average crack width is approximately the same as that recorded at the peak lateral load capacity. The maximum crack width of 12.2 mm is wider than the crack width at the peak. It was noted at 400 mm from the bottom of the base beam on the left edge of the wall panel within the concrete cover. The average crack width of the first six elements starting from 250 mm from the base to 675 mm above the base is 2.5 mm. The average crack width of the six elements

starting from the base edge of the panel to a height of 475 mm is 10.47 mm. Also, the average crack width of the first six elements (horizontally) from the left edge of the wall 250 mm above the base to 475 mm into the wall is 1.28 mm. Shear sliding is captured at ultimate at the base of the panel adjacent to the base beam.

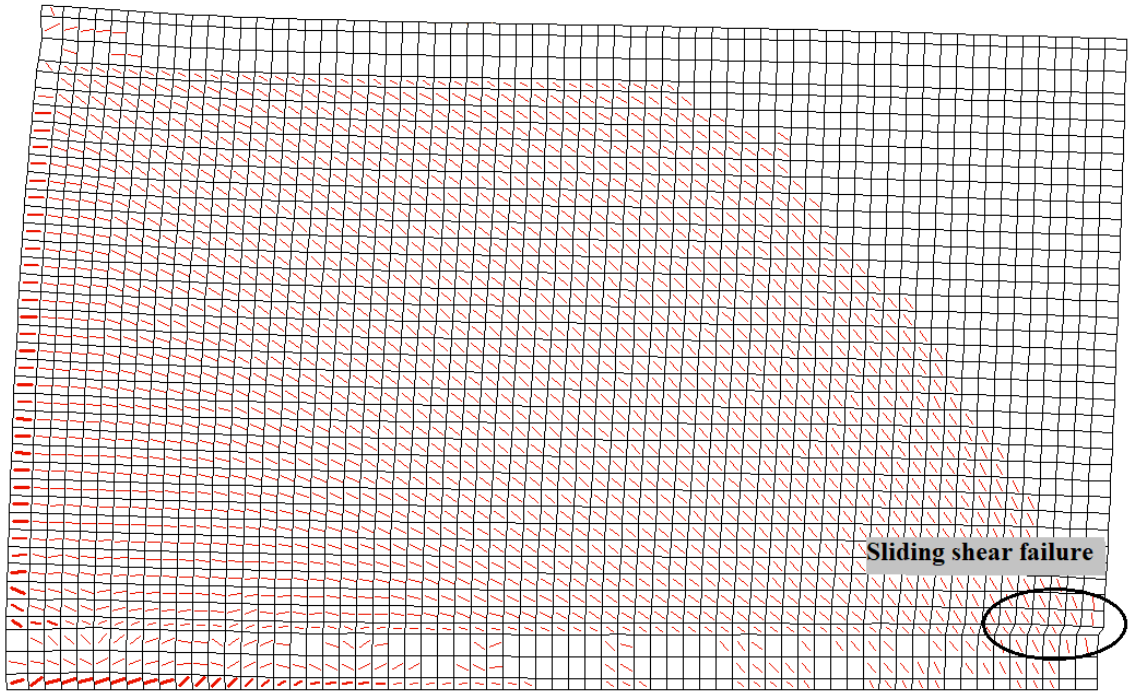

Figure 6-16 Cracking patterns and displaced shape at ultimate

The extent of compressive damage to the concrete material at the location of the failure is measured in the analysis through the ratio of the concrete strain recorded at the load stage to the maximum permissible concrete compressive strain $\left(\varepsilon cm = \frac{\varepsilon_c}{\varepsilon_{cmx}}\right)$. A value exceeding one indicates post-peak response and initiation of concrete crushing. A ratio less than one indicates that the concrete is responding in the pre-peak range. A similar response parameter based on stress can also be evaluated; however, this does not provide a direct

understanding of pre- or post-peak response. The more appropriate measure of damage is through the strain demands.

Figure 6-17 provides the normalized strain at the peak lateral load capacity. The strain profile clearly follows one main diagonal compressive strut from the loading point at the top left edge to the bottom right corner in the wall panel. The initiation of failure due to shear sliding is captured at the right bottom edge of the compression strut where the normalized strain is the highest. A number of elements at the right toe experienced normalized compressive strain higher than one. This indicates the crushing of the concrete in this zone. The concrete elements from the right edge to 475 mm along the base of the wall panel were crushing.

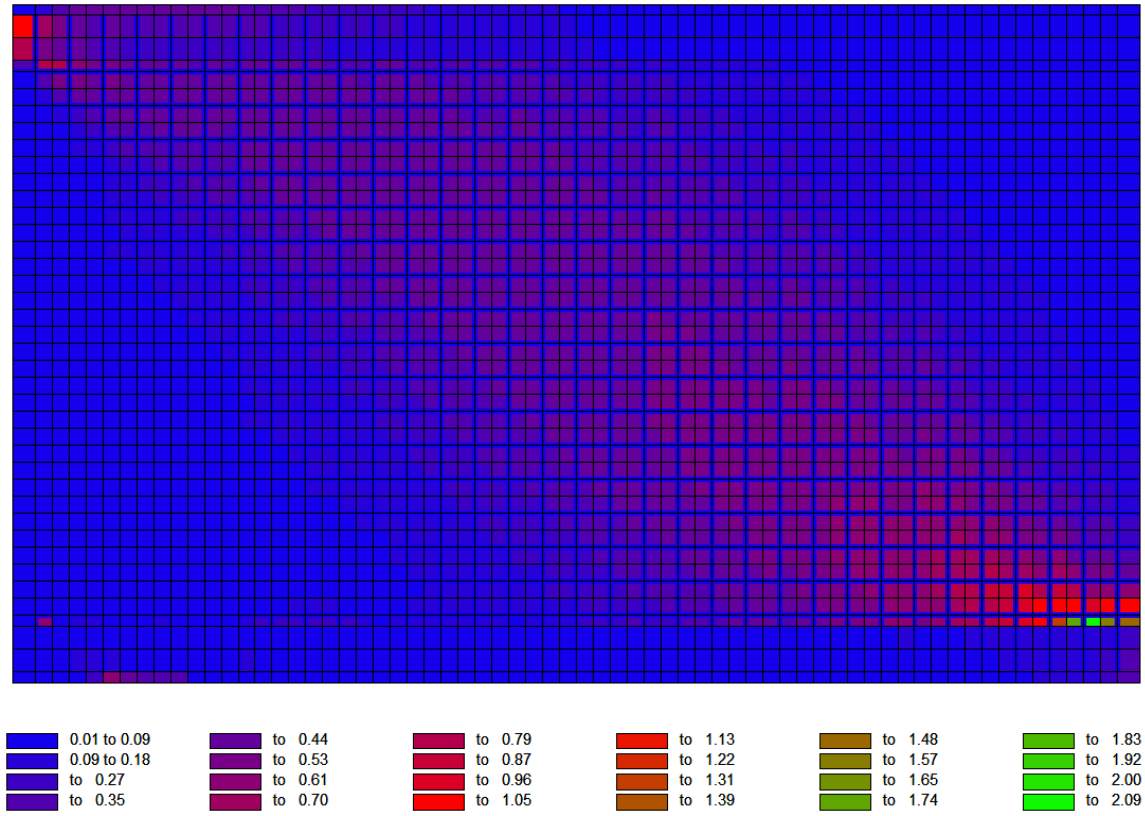

Figure 6-17 Concrete strains at the peak lateral load capacity

Figure 6-18 provides the normalized concrete compressive strain at ultimate. At this stage in the response, the concrete elements at the right toe experienced higher normalized strain, indicating that the concrete had crushed over a widespread area. The highest normalized strains surfaced in the elements adjacent to the base beam, which points towards a shear sliding failure.

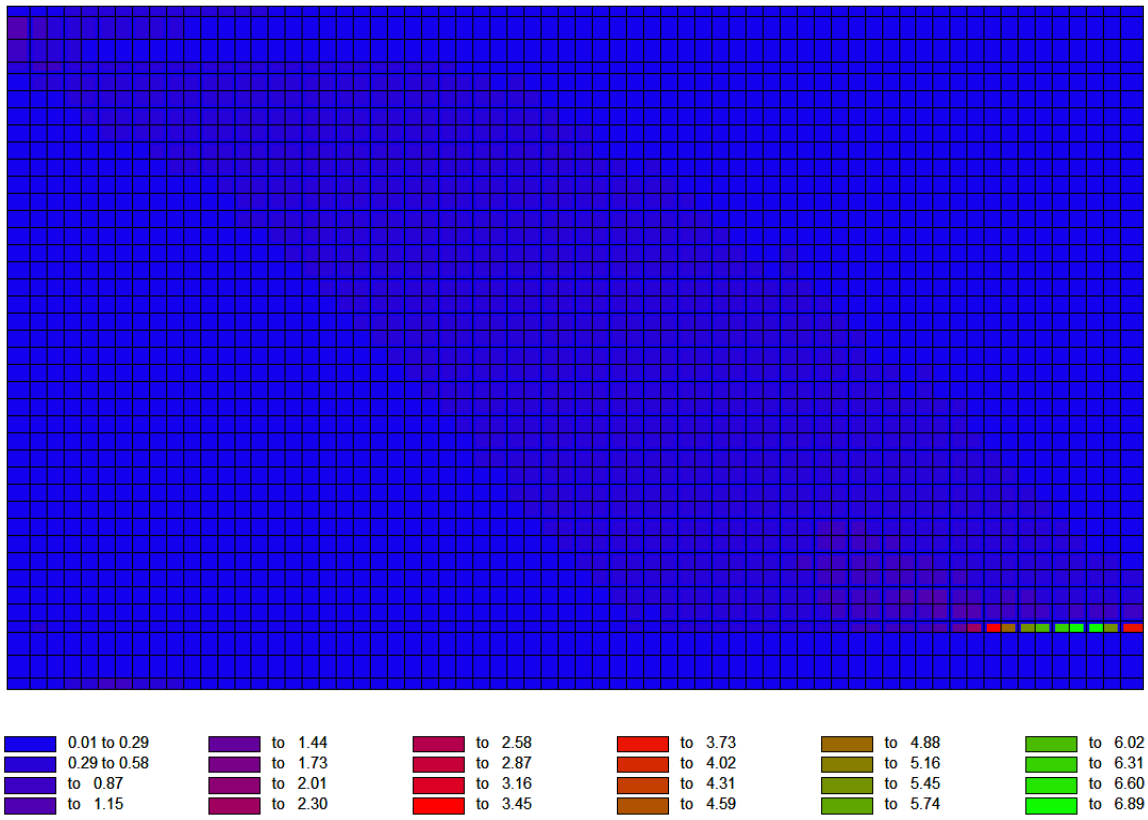

Figure 6-18 Concrete strains at ultimate

The monotonic response of the panel provided a number of global response parameters, including the yield point, the peak lateral loading capacity, the ultimate point, the displacement ductility, the overstrength, and the mode and location of failure. The following section extends the analysis to include the response of the panel to reverse cyclic displacements to investigate the response to a more demanding load condition. In addition, a comparison between the monotonic and reverse cyclic analyses conducted.

6.5 Reverse Cyclic Analysis Results

The reverse cyclic analysis is intended to impart a loading that is more representative of earthquake excitation. Under this loading, alternating excursions of loading and unloading are imposed on the structures. Thus the consequences of loading cycling is captured. In addition to imposing increasing amplitudes of reverse cyclic loading, the number of repetitions at each amplitude should be specified. For this study, three repetitions were selected initially. Initially, the increment in the displacement amplitude is set at 0.1 up to a lateral displacement of 3.5 mm. Thereafter, the increment is gradually increased to 1 until the ultimate condition is reached. The increase in the displacement amplitude increment is to ensure a reasonable number of data points while considering computational time. Figure 6-19 provides the loading protocol for the reverse cyclic analysis.

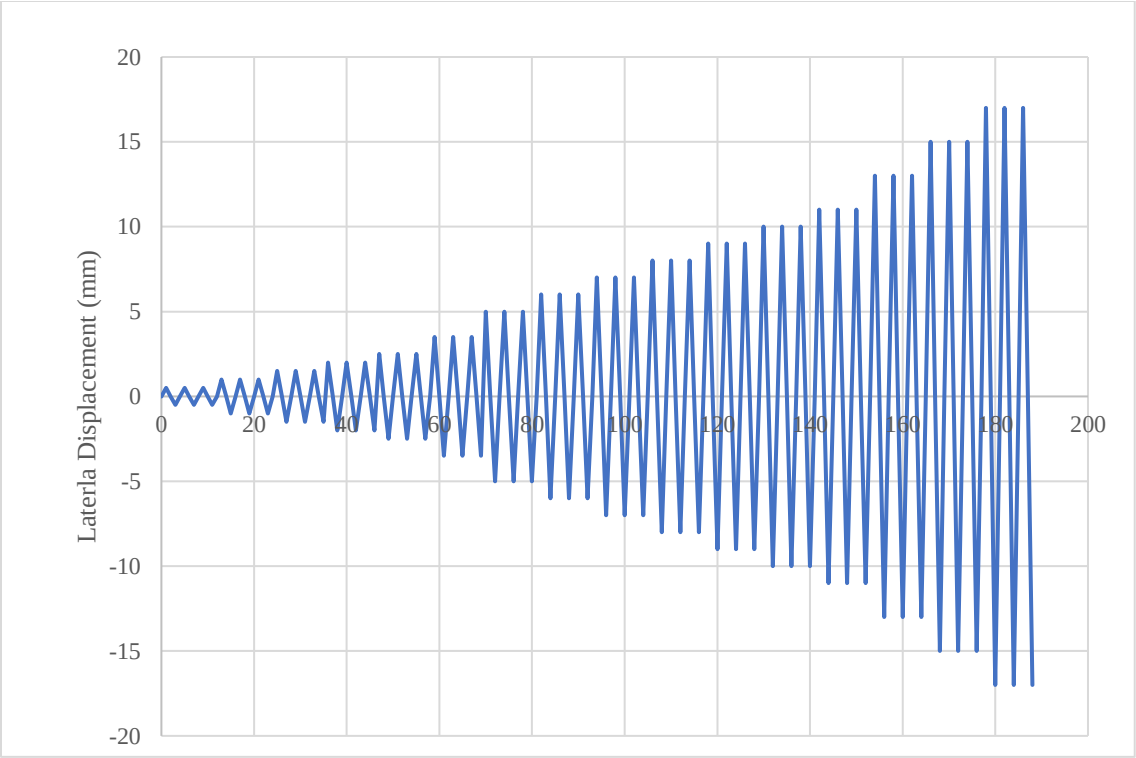

Figure 6-19 Reverse cyclic loading protocol

Recall that for the monotonic loading, a support displacement was specified near the mid-height of the cap beam at the left edge of the panel. The location of this loading is not appropriate for reverse cyclic loading. During a reversal in load, while the wall panel is being pulled at the loading point, local damage arises. This is due to pulling at a concrete at a single node. Therefore, an asymmetric hysteretic response is experienced. Figure 6-20 illustrates the response for the panel due to loading at the left edge of the wall.

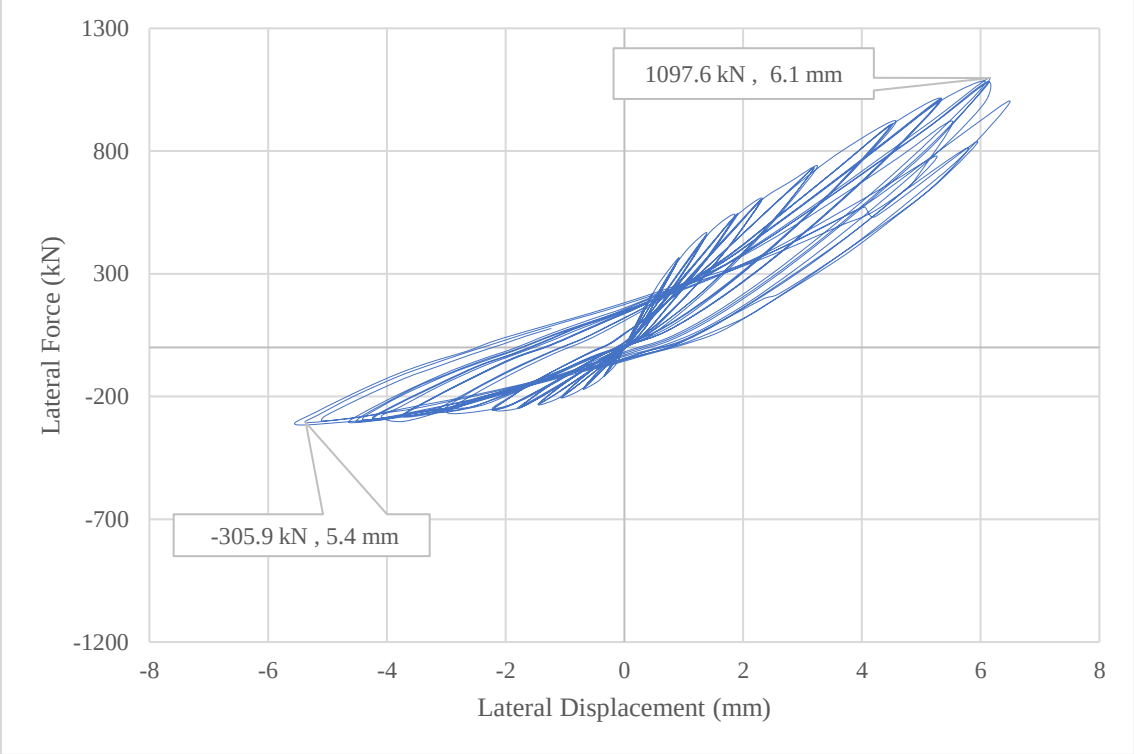

Figure 6-20 Reverse Cyclic response for the panel with the loading from the top left

The response in the pushing motion is different from the pulling motion. The response does not represent the actual behaviour of the wall panel. Under this loading condition, the peak lateral load capacity is captured at 6.1 mm in the pushing direction and 5.4 mm in the pulling direction. The corresponding loads were 1097.6 kN and 305.9 kN, respectively. To further illustrate the inappropriate application of the loading, Figure 6-21 provides the cracking pattern and displaced shape at the peak lateral load capacity during the pulling motion. The damage and local deformation of the concrete elements adjacent to the loading point are not compatible with the realistic response.

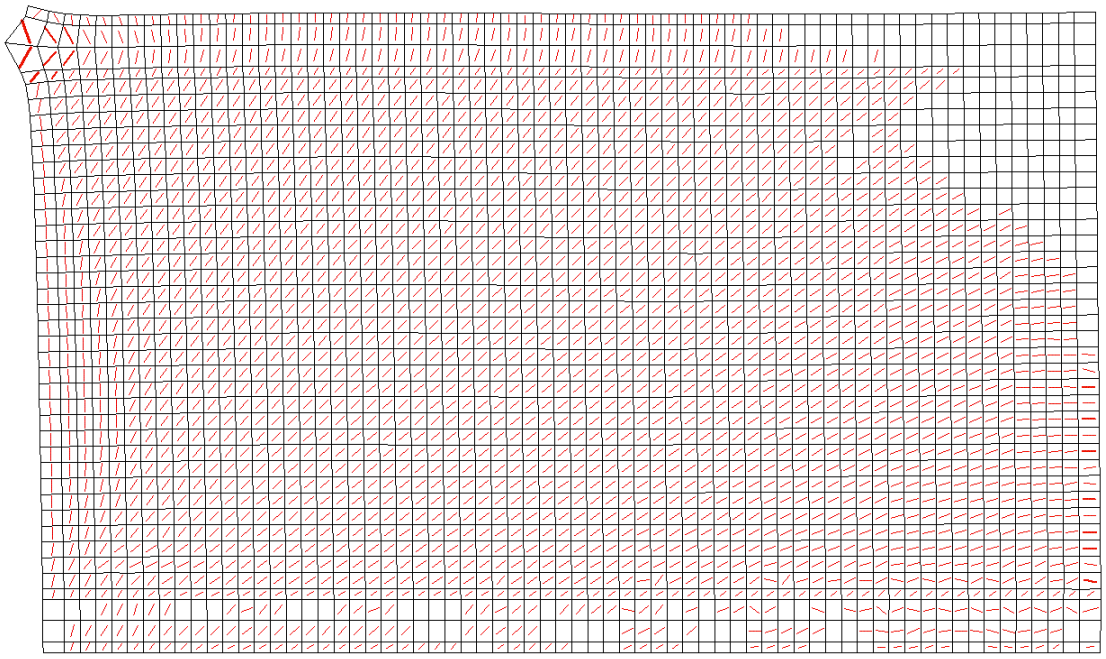

Figure 6-21 Cracking patterns and displaced shape for left edge loading at the maximum point

To provide a more realistic response, the support displacement representing the loading application was placed at the middle of the cap beam as depicted in Figure 6-22.

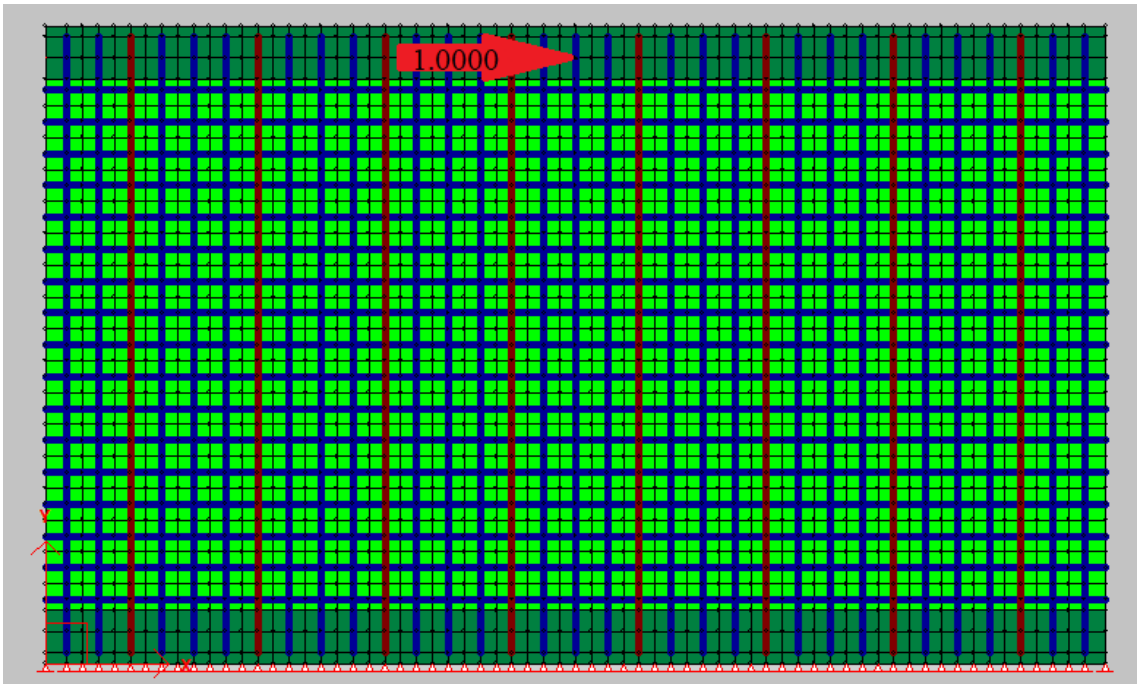

Figure 6-22 Finite element model for reverse cyclic analysis

The final loading protocol for the reverse cyclic analysis was based on suggestions from FEMA 461 ("Interim Testing Protocols for Determining the Seismic Performance Characteristics of Structural and Nonstructural Components," 2007). It suggests imposing a number of loading stages prior to attaining the first or global yield. In addition, FEMA recommends increasing the amplitude by at least 40% from the previous amplitude. Furthermore, if the structure has not reached the final damage state at the peak lateral load capacity, subsequent amplitudes should be increased further by a constant 30%. Table 6-2 provides the loading protocol imposed on the wall panel.

Table 6-2 Loading protocol for reverse cyclic analysis

Repetition	Displacement (mm)
3	0.5
3	1
3	1.5
3	2
3	2.5
3	3.5
3	5
3	6
3	7
3	8
3	9
3	10
3	11
3	13
3	15
3	17

One difference between the loading protocol imposed and the suggestions of FEMA are the number of repetitions. In this study, it was increased from 2 to 3. This is to ensure a sufficient number of cycles are imposed on the wall given the low displacement capacity, and to expose the wall to a more demanding loading. Figure 6-23 provides the lateral load-displacement response for the panel with the updated location for the loading.

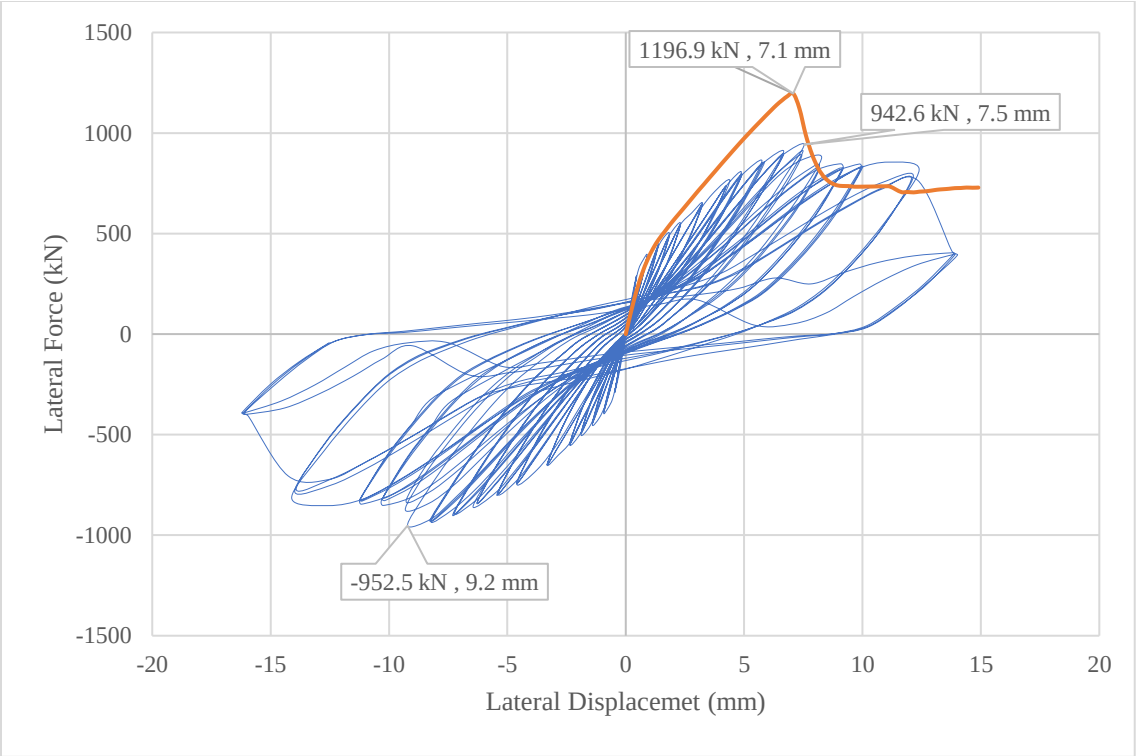

Figure 6-23 Reverse cyclic response with updated loading application

The hysteretic response of the panel is rounded in shape, which indicates a behaviour that is dominated by the response of the concrete with limited yielding. In addition, the pinching of the response is characteristic of shear-dominated behaviour. The relocation of the loading resulted in a symmetrical response, with small differences in the peak lateral load capacity and corresponding displacement. The response in the pulling direction is slightly softened due to the cyclic loading. This led to reduced load capacity and increased displacement. Note that the first load is imposed in the push direction. Furthermore, the post-peak response is also similar for both directions of loading. For comparison, the monotonic response is superimposed on the hysteretic response of the wall. Subtle

differences are evident. The stiffness up to the peak lateral load capacity continuously degrades relative to the monotonic response. Due to this softening, the wall experiences a slightly lower peak lateral load capacity, but a slightly higher displacement capacity at the peak. This translates to a higher displacement ductility under reversed cyclic loading. These differences are the result of the cycling loading, which causes additional damage relative to a monotonic response. In addition, the location of the load at the mid-point of the cap beam results in some local damage causing a further softening. The post-peak response is similar for the two analyses, indicating a similar failure mode.

The maximum lateral force is 942.6 kN in the reverse cyclic response which is slightly less than the monotonic response. Table 6-3 provides a comparison of the results between the reverse cyclic and monotonic analyses.

Table 6-3 Comparison of the results for reverse cyclic and monotonic analyses

Response Parameter	Measure	Reverse Cyclic Positive	Reverse Cyclic Negative	Monotonic
Global Yield	Force (kN)	802.2	-797.89	1052.0
	Displacement (mm)	5.03	-5.63	5.80
Maximum Lateral Load	Force (kN)	942.6	-952.50	1174.1
	Displacement (mm)	7.50	-9.22	7.30
Ultimate Load	Force (kN)	754.1	-762.00	939.30
	Displacement (mm)	11.98	-13.62	7.80
Ductility	Ult. Dis./Yield Dis.	2.38	2.42	1.34
Drift% at Maximum Load	Max Dis/Height	0.26	-0.32	0.25
Over strength	Max. Load/Yield Load	1.17	1.19	1.12

The displaced shape and cracking pattern for the push direction of the reverse cyclic loading is provided in Figure 6-24.

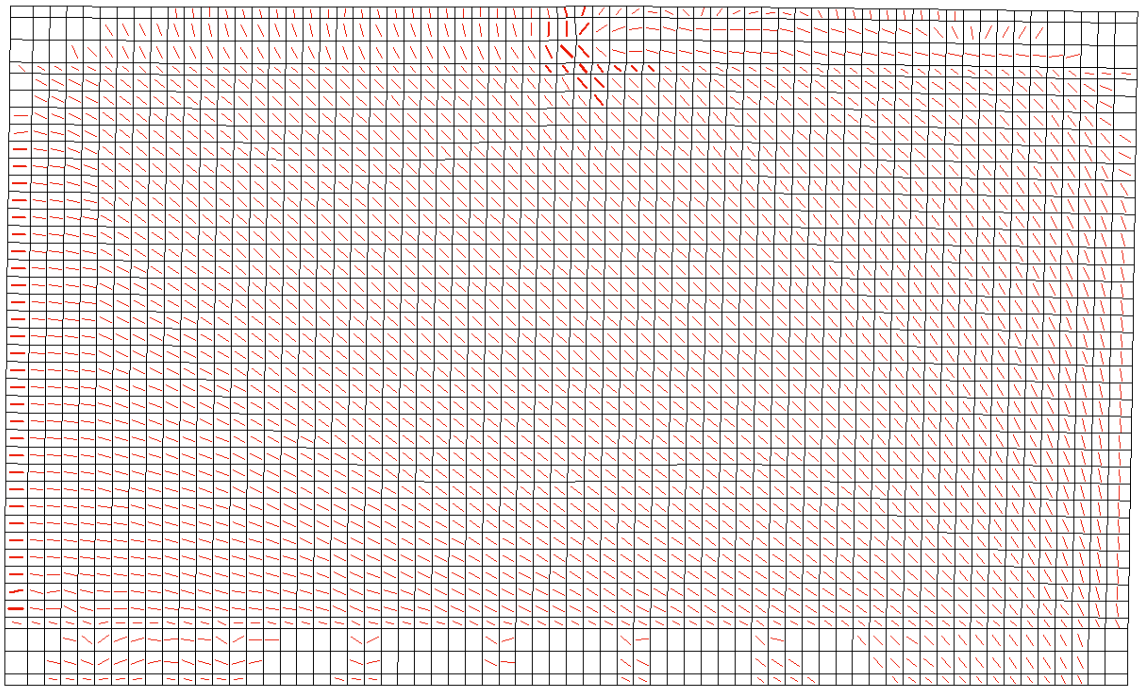

Figure 6-24 Cracking patterns and displaced shape at peak lateral load in the push direction

The horizontal cracks along the concrete cover at the left edge of the wall indicate an area of high tensile stresses. The width of cracks at the middle of the cap beam are not negligible. These cracks coincide with the location of the loading in the analysis. In reality, such cracking should not be expected as loading from an earthquake would be distributed along the length of the wall. To correct this in the analysis would require the wall to be pushed from either end of the wall. This requires stopping and restarting the analysis after each half cycle and was deemed to be not necessary given the satisfactory results given by the analysis with the loading at the middle of the cap beam.

The displaced shape and crack patterns for the pull direction at the peak lateral load capacity is provided in Figure 6-25.

Figure 6-25 Cracking patterns and displaced shape at peak lateral load in the pull direction

The displaced shaped and cracking patterns are symmetrical. The width of the cracks along the concrete cover at the left edge of the panel during pushing varies between 6.1 mm to 0.1 mm. For the pull direction, the crack widths range from 4.4 mm to 0.08 mm at the right edge of the wall.

Figure 6-26 illustrates the displaced shape and cracking of the wall at ultimate. The larger cracks in the wall adjacent to the base beam indicate shear sliding failure.

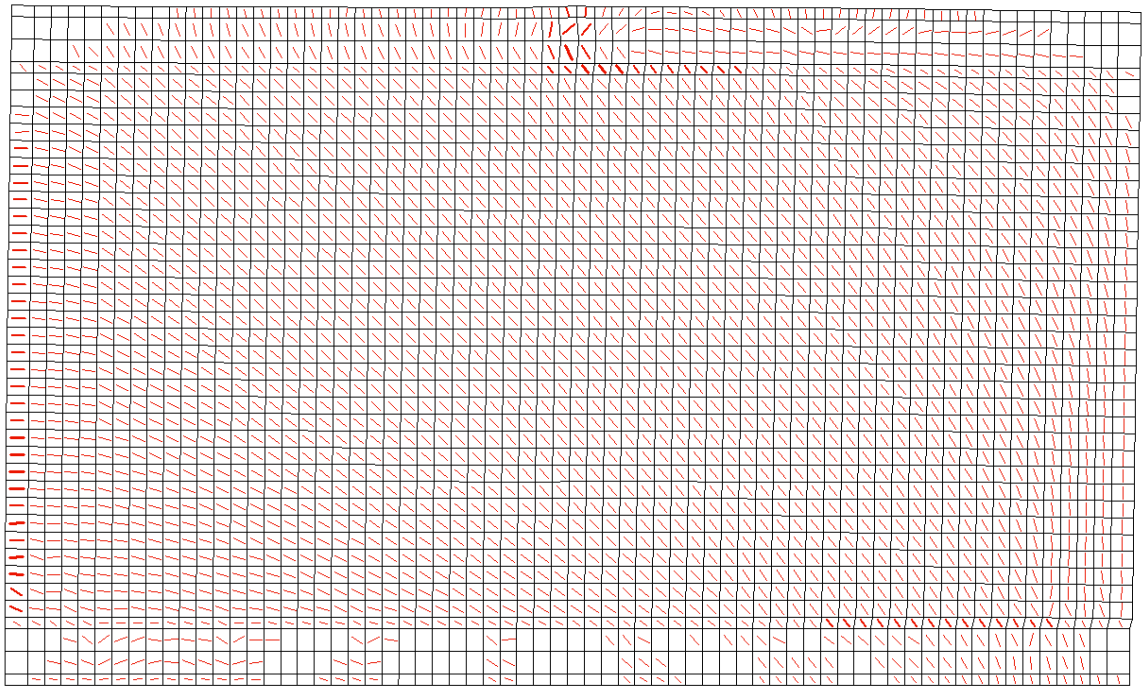

Figure 6-26 Cracking patterns and displaced shape at ultimate in the push direction

Similarly, the cracking pattern and displaced shape in the pull direction point to shear sliding at the right toe of the wall Figure 6-27.

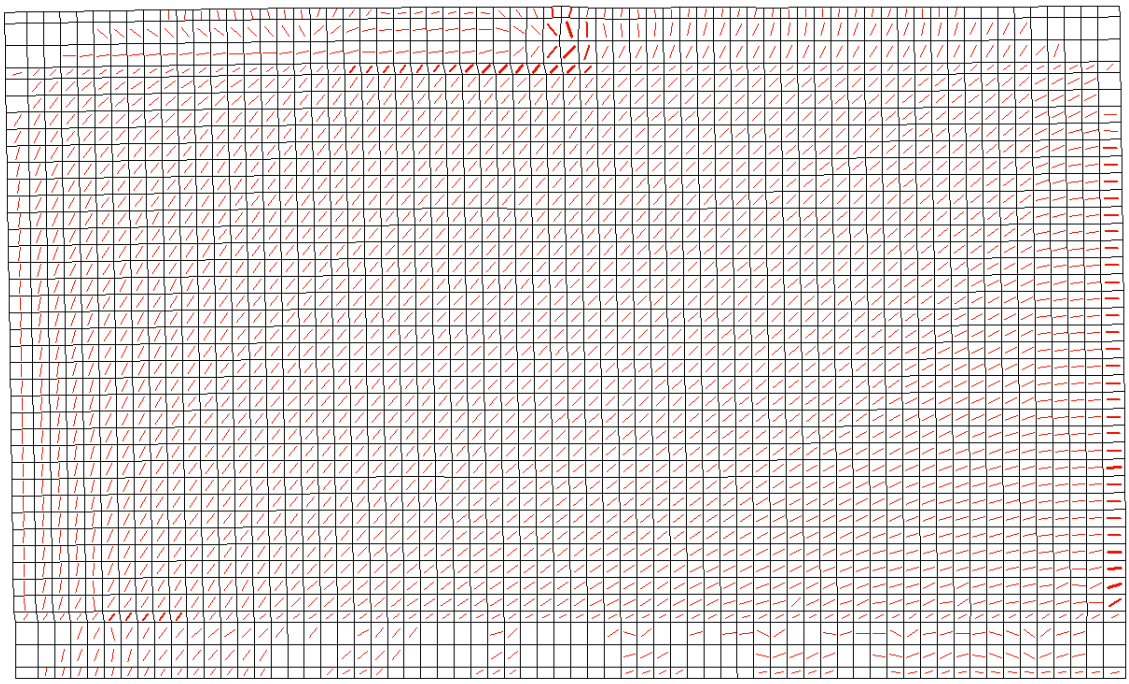

Figure 6-27 Cracking patterns and displaced shape at ultimate in the pull direction

Chapter 7 Conclusions and Future Work

7.1 Summary

The in-plane lateral performance of the TSP wall system demonstrated that proper modifications to the design and fabrication of the wall could lead to improved lateral performance of the system. The primary technical challenge was to determine the contribution of the partially embedded external light gauge steel. In addition, understanding the bond characteristics between the internal smooth wire-mesh reinforcement placed within the concrete panel was vital to establishing a reliable estimate of the lateral strength and displacement capacities. These two issues cannot be routinely evaluated using current design standards. To address this, sensitivity analysis was performed using nonlinear finite element analysis in place of experimental testing to better understand the parameters that are critical for the lateral performance of the thin shell wall panel fabricated by Burnco Manufacturing. The study considered the effects of the embedment length and bond characteristics of the external light gauge steel and internal wire-mesh reinforcement separately, the type of internal reinforcement (smooth or deformed), the size of the internal reinforcement, and the contribution of the effective area of the external light gauge steel. Based on sensitivity analyses, design and fabrication suggestions were proposed to Burnco MFG. The suggested improvements to the wall system were considered in detailed analyses of the wall under monotonic and reverse cyclic displacements. The final assessment provided information of the yield, maximum, and ultimate loads and displacements, in

addition to the displacement ductility and system over strength. Furthermore, the analyses shed light on the cracking patterns, displaced shape and expected failure mode.

7.2 Conclusions

The finite element analyses demonstrated that the contribution of the external light gauge steel to the lateral load resistance of the wall panel is less than 10% in comparison to the benchmark model. Each of the parameters investigated in the analyses were evaluated separately and compared to the benchmark model, which was based on the original design of the walls as provided by Burnco Manufacturing. The following conclusions are based on numerical analyses:

Finite Element Sensitivity Analysis for Slender Wall Panel

a) Increasing the bar size from 6 mm diameter to 10 mm diameter for the internal wire-mesh reinforcement did not increase the lateral performance, in this specific wall panel. It illustrated that the bond characteristic controlled the lateral response.

b) The type of reinforcement (smooth or deformed) had a considerable effect on the lateral resistance of the wall. The strength increased by a factor of 3.5 and the displacement increased by a factor of 23. This further illustrated that the bond characteristic is the main factor for the lateral response of the panel.

c) Providing end hooks in the vertical wire-mesh reinforcement and end anchorage for the external light gauge steel into the cap and beam beams resulted in an improvement of the lateral force capacity by a factor of 3.4 and the lateral displacement by a factor 20. This provided additional evidence regarding the

importance of the bond of the internal wire-mesh reinforcements to the lateral performance.

d) Increasing the embedment length of the internal wire-mesh reinforcement and the external light gauge steel from 100 mm to 200 mm into the cap and base beams slightly improved the lateral performance. The maximum lateral force capacity increased by a factor of 1.32 with the longer embedment length compared to the benchmark model with the smaller embedment.

e) The close spacing (150 mm by 150 mm) and the welded intersections of the vertical and horizontal components of the internal wire-mesh reinforcement can be assumed to provide a perfect bond with the concrete, which leads to a substantial improvement in the lateral performance of the wall.

f) The presence of the exterior light gauge steel with the full contribution marginally enhances the lateral resistance of the wall. The displacement capacity remains the same whereas the maximum lateral force increased by 8%.

Finite Element Sensitivity Analysis for Squat Wall Panel

a) Increasing bar size from 6 mm diameter to 10 mm diameter for the internal wire-mesh reinforcement did not increase the lateral performance; the strength decreased by a factor of 0.9 and the displacement remained the same. This shed light on the bond characteristics of the internal wire-mesh reinforcement controlling the lateral response of the wall.

b) The type of reinforcement had a considerable effect on the lateral capacity of the wall. The deformed bar option provided substantially improved ductility and lateral strength capacities relative to smooth bars for the internal wire-mesh reinforcement. The lateral strength increased by a factor of 2.8 for the model with deformed reinforcement. In addition, the displacement capacity increased by a factor of 5.4. Similar to the slender wall model, the deformed bar drastically improves the bond of the wire mesh to the concrete in the squat wall.

c) Assuming end hooks on the vertical wire-mesh reinforcement and improved end anchorage of the external light gauge steel resulted in improved lateral performance. The maximum lateral load increased by a factor of 2.86 in comparison to straight bars. End anchorage of the vertical reinforcement improved the bond characteristics between the reinforcement and concrete.

d) Increasing the embedment length of the wire-mesh reinforcement and the external light gauge steel from 100 mm to 200 mm in the cap and bases beams slightly improved the lateral performance. The maximum lateral load capacity increased by a factor of 1.36 with the longer embedment length while the displacement increased by a factor of 1.6.

e) The welding of the wire-mesh reinforcement at the intersections of the vertical and horizontal components, combined with the tight spacing, lead to the assumption of perfect bonding between concrete and reinforcement. Perfect bonding of the

vertical wire-mesh reinforcement resulted in an increase of the lateral strength capacity of the squat wall by a factor of 2.62.

f) The presence of the exterior light gauge steel slightly improves the lateral resistance of the wall when it is considered as fully contributing. The lateral strength improved by 10%. However, the displacement capacity remained similar to the benchmark.

The lateral performance of the wall panel systems could be substantially improved based on implementing modifications to the design and fabrication as illustrated by the finite element analyses. These modifications include: an increase in the length of embedment accompanied with end hooks on the vertical components of the internal wire-mesh reinforcement into the cap and beams; and extending the exterior light gauge steel in the cap and base beams with additional end anchorage. Note that although deformed bars are generally preferred in concrete construction, the increase in embedment length with end hooks for the wire mesh provides improved bonding characteristics. In addition, the close spacing of the welded mesh further enhances the bond to the concrete. Therefore, deformed wire-mesh reinforcement was deemed not necessary.

Based on the final design of the wall panel, and taking into account the changes noted above, the following conclusions are drawn for the squat wall option subjected to monotonic loading. [Recall that the final design was implemented for the squat wall given that this is the preferred wall assembly.]:

Monotonic Analysis

a) The vertical component of the internal wire-mesh reinforcement located at 100 mm from the left edge of the wall first yielded at 6.0 mm of lateral displacement at a corresponding lateral load of 1073.6 kN.

b) Based on established principles and the pushover response curve, the global yield of the wall panel system was estimated to be 5.8 mm of displacement at the corresponding lateral load of 1052.0 kN.

c) At the global yield point, two vertical wire mesh and one exterior light gauge steel yielded, whereas at ultimate (80% of the maximum lateral load), three vertical wire mesh and two exterior light gauge steel had yielded.

d) The analysis captured failure due to shear sliding at the base of the wall adjacent to the base beam.

e) The drifts corresponding to the global yield point, the first yield point, the maximum lateral force capacity, and ultimate were 0.20, 0.21, 0.26, and 0.27, respectively.

f) The ductility and over strength capacities were 1.34 and 1.12, respectively.

The final model had a sliding shear failure at ultimate which was expected. Regarding the ductility calculation for the final design, the wall system provides a ductility level of 1.34 which is less than 2, that is typical for a well-designed reinforced concrete squat shear wall following detailing for seismic effects. The following conclusions are drawn from the reverse cyclic displacement loading protocol.

Reverse Cyclic Analysis

a) The response of the wall in the pushing motion differed from the pulling motion when the loading was imposed at one the edge of the wall. This behaviour is not representative of the actual behaviour and is due to localized damaged of the elements during the pulling excursions.

b) The relocation of loading to the midpoint of the cap beam resulted in a symmetrical response, with negligible differences in the peak lateral load capacities and corresponding displacements.

c) The cracking that was captured at the updated location of the loading also does not represent fully the application of seismic loading. The solution would be to push the panel from either side during the analysis. This would require stopping and restarting the analysis at the end of each unloading cycle.

d) The hysteretic response of the panel is rounded in shape, which indicates a behaviour that is dominated by the response of the concrete with limited yielding.

e) The response in the pulling direction is slightly softened due to the cyclic loading. This led to increased displacements.

f) Due to this softening, the wall experienced lower peak lateral load capacity, but higher displacement capacity at the peak in comparison to the monotonic analysis.

g) The pinching of the hysteretic response indicates behaviour that is shear dominant.

h) The ductility capacities for the push and the pull excursions of loading sides were 2.38 and 2.42, respectively. The ductility capacities are less than 2.5 which is expected for welded wire mesh squat walls that lack sufficient seismic detailing.

i) The overstrength capacities for the push and pull motions of loading were 1.17 and 1.19, respectively.

j) The drifts corresponding to the maximum lateral load capacities during the push and pull cycles were 0.26 and 0.32, respectively.

7.3 Future Work

The lateral performance of slender and squat wall panels have been evaluated as part of this study based on two-dimensional finite element models. Future studies should consider experimental testing of both the slender and squat wall panels at full scale to corroborate the two-dimensional models and to better understand the actual behaviour of the panels and all components. In addition, three-dimensional nonlinear finite element models should be developed to determine whether two-dimensional models are capable of capturing the salient features of response.

References

About @ www.nexcon.ca. (2011). Retrieved from http://www.nexcon.ca/index.php?action=benifits

Allam, S. M., Shoukry, M. S., Rashad, G. E., & Hassan, A. S. (2013). Evaluation of tension stiffening effect on the crack width calculation of flexural RC members. *Alexandria Engineering Journal*, *52*(2), 163–173. https://doi.org/10.1016/j.aej.2012.12.005

Angle, B. (2015). Double dovetail extended lip Inside Corner radius R =.125" u/n 3/4 1.

Bamonte, P., Coronelli, D., & Gambarova, P. G. (2003). Smooth Anchored Bars in NSC and HPC: a Study on Size Effect. *Journal of Advanced Concrete Technology, 1*(1), 42–53. https://doi.org/10.3151/jact.1.42

Bamonte, P., Coronelli, D., & Gambarova, P. G. (2006). Size Effect in the Bonding of Smooth and Deformed Bars : Nsc versus HPC. *Fracture of Nano and Engineering Materials and Structures*, 1371–1372. https://doi.org/10.1007/1-4020-4972-2_681

Bamonte, P. F., & Gambarova, P. G. (2007). High-Bond Bars in NSC and HPC: Study on Size Effect and on the Local Bond Stress-Slip Law. *Journal of Structural Engineering*, *133*(2), 225–234. https://doi.org/10.1061/(ASCE)0733-9445(2007)133:2(225)

Bažant, Z. P., Li, Z., & Thoma, M. (1995). Identification of Stress-Slip Law for Bar or Fiber Pullout by Size Effect Tests. *Journal of Engineering Mechanics*, *121*, 620–

625. https://doi.org/10.1061/(ASCE)0733-9399(1995)121:5(620)

Bousias, S. N., Spathis, A.-L., & Fardis, M. N. (2007). Seismic Retrofitting of Columns with Lap Spliced Smooth Bars Through FRP or Concrete Jackets. *Journal of Earthquake Engineering*, *11*(5), 653–674. https://doi.org/10.1080/13632460601125714

Braga, F., Gigliotti, R., Laterza, M., D'Amato, M., & Kunnath, S. (2012). Modified steel bar model incorporating bond-slip for seismic assessment of concrete structures. *Journal of Structural Engineering*, *138*(November), 1342–1350. https://doi.org/10.1061/(ASCE)ST.1943-541X.0000587.

Cement Association of Canada., & Canadian Standards Association. (2010). *Concrete design handbook.* Retrieved from https://books.google.ca/books/about/Concrete_Design_Handbook_CSA_group_stand.html?id=ARKPAQAACAAJ&redir_esc=y

Fabbrocino, G., Verderame, G. M., & Manfredi, G. (2005). Experimental behaviour of anchored smooth rebars in old type reinforced concrete buildings. *Engineering Structures*, *27*(10), 1575–1585. https://doi.org/10.1016/j.engstruct.2005.05.002

Fabbrocino, G., Verderame, G. M., Manfredi, G., & Cosenza, E. (2004). Structural models of critical regions in old-type r.c. frames with smooth rebars. *Engineering Structures*, *26*(14), 2137–2148. https://doi.org/10.1016/j.engstruct.2004.07.018

Fabbrocino, G., Verderame, G. M., & Polese, M. (2007). Probabilistic steel stress-crack width relationship in R.C. frames with smooth rebars. *Engineering Structures*, *29*(1),

1–10. https://doi.org/10.1016/j.engstruct.2006.04.002

Fang, C., Lundgren, K., Chen, L., & Zhu, C. (2004). Corrosion influence on bond in reinforced concrete. *Cement and Concrete Research*, *34*(11), 2159–2167. https://doi.org/10.1016/j.cemconres.2004.04.006

Fernandes, C., Varum, H., & Costa, A. (2013). Importance of the bond-slip mechanism in the numerical simulation of the cyclic response of RC elements with plain reinforcing bars. *Engineering Structures*, *56*, 396–406. https://doi.org/10.1016/j.engstruct.2013.05.013

Interim Testing Protocols for Determining the Seismic Performance Characteristics of Structural and Nonstructural Components. (2007). *Federal Emergency Management Agency*, *461*(June), 20–27.

Karimi, B. (2015a). Assembly of wall sample for testing, *1*, 1.

Karimi, B. (2015b). Burnco 6 in Stud x. 0566 Section Properties, 1.

Karimi, B. (2016). Assembly of wall sample for testing SK#4T-4 samples require. *Burnco MFG*, (2), 2016.

Muttoni, A., and Ruiz, M. F. (2008). Shear strength of members without transverse reinforcement. *ACI Structural Journal*, *105*(2), 163–172. https://doi.org/10.1139/l96-004

Park, H., & Kim, J.-Y. (2005). Plasticity model using multiple failure criteria for concrete in compression. *International Journal of Solids and Structures*, *42*(8), 2303–2322. https://doi.org/10.1016/j.ijsolstr.2004.09.029

Park, R. (1988). Ductility evaluation from laboratory and analytical testing. *Proceedings of the 9th World Conference on Earthquake Engineering, 2-9 August*. https://doi.org/1

Pekelnicky, R., & Poland, C. (2012). ASCE 41-13: Seismic Evaluation and Retrofit Rehabilitation of Existing Buildings. *Citeseer*, 1–12. https://doi.org/10.1016/j.aqpro.2013.07.003

Priestley, M. J. N., Verma, R., & Xiao, Y. (1994). Seismic shear strength of reinforced concrete columns. *Journal of Bridge Engineering*, *120*(8), 2310–2329.

Products @www.nexcon.ca. (2011). Retrieved from http://www.nexcon.ca/index.php?action=products

R.Park. (1989). Evaluation of ductility of structures and structural assemblages from laboratory testing. NZSEE Quarterly Bulletin.

Shin, J., & Kim, J. H. (2014). Different macroscopic models for slender and squat reinforced concrete walls subjected to cyclic loads. *Earthquake and Structures*, *7*(5), 877–892. https://doi.org/10.12989/eas.2014.7.5.877

Stang, H., Li, Z., & Shah, S. P. (1990). Pullout problem : stress versus fracture mechanical approach, *116*(10), 2136–2150.

Tilly, G. P. (1979). Fatigue of Steel Reinforcement Bars in Concrete: a Review. *Fatigue & Fracture of Engineering Materials & Structures*, *2*(3), 251–268. https://doi.org/10.1111/j.1460-2695.1979.tb01084.x

Tuck, B. (2014). Typical Wall Anchorage, (Burnco).

Vecchio, B. F. J. (1993). Finite element modeling of concrete expansion and confinement. *Journal of Structural Engineering*, *118*(9), 2390–2406.

Vecchio, F. J. (2000). Disturbed Stress Field Model For Reinforced Concrete: Formulation. *Journal of Structural Engineering*, (September), 1070–1077.

Vecchio, F. J., & Collins, M. P. (1986). The Modified Compression-Field Theory for Reinforced Concrete Elements Subjected to Shear. *ACI Journal Proceedings*. https://doi.org/10.14359/10416

Verderame, G. M., Fabbrocino, G., & Manfredi, G. (2008a). Seismic response of r.c. columns with smooth reinforcement. Part I: Monotonic tests. *Engineering Structures*, *30*(9), 2277–2288. https://doi.org/10.1016/j.engstruct.2008.01.025

Verderame, G. M., Fabbrocino, G., & Manfredi, G. (2008b). Seismic response of r.c. columns with smooth reinforcement. Part II: Cyclic tests. *Engineering Structures*, *30*(9), 2289–2300. https://doi.org/10.1016/j.engstruct.2008.01.024

Wong, P. S., Vecchio, F. J., & Trommels, H. (2000). *VecTor2 & FormWorks User's Manual*. *Notes* (Second Edi). https://doi.org/10.1037/023990

Appendices

Appendix A: Files corresponding to Finite Element Sensitivity Analyses

Table A-1 Files Corresponding to Finite Element Analyses: Pushover Loading

#	File Name	Stud	Panel Size	Bar Size	Bar Type	Hook Bar	Perfect Bonding X-Axis	Perfect Bonding Y-Axis	No Perfect Bonding	Perfec Bonding	Embedment Length	Used
1	1-27	386	1800x3000	10	S	No	Y	N	N	N	100	Bar Size
2		386	1800x3000	10	S	No	N	Y	N	N	100	Bar Size
3		386	1800x3000	10	S	No	N	N	Y	N	100	Bar Size
4		386	1800x3000	10	S	No	N	N	N	Y	100	Bar Size
5	1-31	386	1800x3000	10	D	No	Y	N	N	N	100	Bar Size
6		386	1800x3000	10	D	No	N	Y	N	N	100	Bar Size
7		386	1800x3000	10	D	No	N	N	Y	N	100	Bar Size
8		386	1800x3000	10	D	No	N	N	N	Y	100	Bar Size
9	1-34	No	1800x3000	6	S	No	Y	N	N	N	100	Benchmark
10		No	1800x3000	6	S	No	N	Y	N	N	100	Benchmark
11		No	1800x3000	6	S	No	N	N	Y	N	100	Benchmark
12		No	1800x3000	6	S	No	N	N	N	Y	100	Benchmark
13	1-35	386	1800x3000	6	S	No	Y	N	N	N	100	Perfect Bond
14		386	1800x3000	6	S	No	N	Y	N	N	100	Perfect Bond
15		386	1800x3000	6	S	No	N	N	Y	N	100	Perfect Bond
16		386	1800x3000	6	S	No	N	N	N	Y	100	Perfect Bond
17	1-35-H	133	1800x3000	6	S	No	Y	N	N	N	100	Stud Existance
18		133	1800x3000	6	S	No	N	Y	N	N	100	Stud Existance
19		133	1800x3000	6	S	No	N	N	Y	N	100	Stud Existance
20		133	1800x3000	6	S	No	N	N	N	Y	100	Stud Existance
21	1-36	No	1800x3000	6	S	Yes	Y	N	N	N	100	Hooked
22		No	1800x3000	6	S	Yes	N	Y	N	N	100	Hooked
23		No	1800x3000	6	S	Yes	N	N	Y	N	100	Hooked
24		No	1800x3000	6	S	Yes	N	N	N	Y	100	Hooked
25	1-38	No	1800x3000	6	D	No	Y	N	N	N	100	Bar Type
26		No	1800x3000	6	D	No	N	Y	N	N	100	Bar Type
27		No	1800x3000	6	D	No	N	N	Y	N	100	Bar Type
28		No	1800x3000	6	D	No	N	N	N	Y	100	Bar Type
29	1-39	386	1800x3000	6	D	No	Y	N	N	N	100	Bar Size
30		386	1800x3000	6	D	No	N	Y	N	N	100	Bar Size
31		386	1800x3000	6	D	No	N	N	Y	N	100	Bar Size
32		386	1800x3000	6	D	No	N	N	N	Y	100	Bar Size
33	5-34	No	5000x3000	6	S	No	Y	N	N	N	100	Benchmark

#	File Name	Stud	Panel Size	Bar Size	Bar Type	Hook Bar	Perfect Bonding X-Axis	Perfect Bonding Y-Axis	No Perfect Bonding	Perfec Bonding	Embedment Length	Used
34		No	5000x3000	6	S	No	N	Y	N	N	100	Benchmark
35		No	5000x3000	6	S	No	N	N	Y	N	100	Benchmark
36		No	5000x3000	6	S	No	N	N	N	Y	100	Benchmark
37	5-35	386	5000x3000	6	S	No	Y	N	N	N	100	Perfect Bond
38		386	5000x3000	6	S	No	N	Y	N	N	100	Perfect Bond
39		386	5000x3000	6	S	No	N	N	Y	N	100	Perfect Bond
40		386	5000x3000	6	S	No	N	N	N	Y	100	Perfect Bond
41	5-35-H	133	5000x3000	6	S	No	Y	N	N	N	100	Stud Existance
42		133	5000x3000	6	S	No	N	Y	N	N	100	Stud Existance
43		133	5000x3000	6	S	No	N	N	Y	N	100	Stud Existance
44		133	5000x3000	6	S	No	N	N	N	Y	100	Stud Existance
45	5-36	No	5000x3000	6	S	Yes	Y	N	N	N	100	Hooked
46		No	5000x3000	6	S	Yes	N	Y	N	N	100	Hooked
47		No	5000x3000	6	S	Yes	N	N	Y	N	100	Hooked
48		No	5000x3000	6	S	Yes	N	N	N	Y	100	Hooked
49	5-38	No	5000x3000	6	D	No	Y	N	N	N	100	Bar Type
50		No	5000x3000	6	D	No	N	Y	N	N	100	Bar Type
51		No	5000x3000	6	D	No	N	N	Y	N	100	Bar Type
52		No	5000x3000	6	D	No	N	N	N	Y	100	Bar Type
53	6-27	386	1800x3000	10	S	No	Y	N	N	N	200	Bar Size
54		386	1800x3000	10	S	No	N	Y	N	N	200	Bar Size
55		386	1800x3000	10	S	No	N	N	Y	N	200	Bar Size
56		386	1800x3000	10	S	No	N	N	N	Y	200	Bar Size
57	6-31	386	1800x3000	10	D	No	Y	N	N	N	200	Bar Size
58		386	1800x3000	10	D	No	N	Y	N	N	200	Bar Size
59		386	1800x3000	10	D	No	N	N	Y	N	200	Bar Size
60		386	1800x3000	10	D	No	N	N	N	Y	200	Bar Size
61	6-34	No	1800x3000	6	S	No	Y	N	N	N	200	Embedment
62		No	1800x3000	6	S	No	N	Y	N	N	200	Embedment
63		No	1800x3000	6	S	No	N	N	Y	N	200	Embedment
64		No	1800x3000	6	S	No	N	N	N	Y	200	Embedment
65	6-35	386	1800x3000	6	S	No	Y	N	N	N	200	Perfect Bonding
66		386	1800x3000	6	S	No	N	Y	N	N	200	Perfect Bonding

#	File Name	Stud	Panel Size	Bar Size	Bar Type	Hook Bar	Perfect Bonding X-Axis	Perfect Bonding Y-Axis	No Perfect Bonding	Perfec Bonding	Embedment Length	Used
67		386	1800x3000	6	S	No	N	N	Y	N	200	Perfect Bonding
68		386	1800x3000	6	S	No	N	N	N	Y	200	Perfect Bonding
69	6-36	No	1800x3000	6	S	Yes	Y	N	N	N	200	Hooked
70		No	1800x3000	6	S	Yes	N	Y	N	N	200	Hooked
71		No	1800x3000	6	S	Yes	N	N	Y	N	200	Hooked
72		No	1800x3000	6	S	Yes	N	N	N	Y	200	Hooked
73	6-38	No	1800x3000	6	D	No	Y	N	N	N	200	Bar Type
74		No	1800x3000	6	D	No	N	Y	N	N	200	Bar Type
75		No	1800x3000	6	D	No	N	N	Y	N	200	Bar Type
76		No	1800x3000	6	D	No	N	N	N	Y	200	Bar Type
77	6-39	386	1800x3000	6	D	No	Y	N	N	N	200	Bar Size
78		386	1800x3000	6	D	No	N	Y	N	N	200	Bar Size
79		386	1800x3000	6	D	No	N	N	Y	N	200	Bar Size
80		386	1800x3000	6	D	No	N	N	N	Y	200	Bar Size
81	7-34	No	5000x3000	6	S	No	Y	N	N	N	200	Emdebment
82		No	5000x3000	6	S	No	N	Y	N	N	200	Emdebment
83		No	5000x3000	6	S	No	N	N	Y	N	200	Emdebment
84		No	5000x3000	6	S	No	N	N	N	Y	200	Emdebment
85	7-35	386	5000x3000	6	S	No	Y	N	N	N	200	Perfect Bonding
86		386	5000x3000	6	S	No	N	Y	N	N	200	Perfect Bonding
87		386	5000x3000	6	S	No	N	N	Y	N	200	Perfect Bonding
88		386	5000x3000	6	S	No	N	N	N	Y	200	Perfect Bonding
89	7-36	No	5000x3000	6	S	Yes	Y	N	N	N	200	Hooked
90		No	5000x3000	6	S	Yes	N	Y	N	N	200	Hooked
91		No	5000x3000	6	S	Yes	N	N	Y	N	200	Hooked
92		No	5000x3000	6	S	Yes	N	N	N	Y	200	Hooked
93	7-38	No	5000x3000	6	D	No	Y	N	N	N	200	Bar Type
94		No	5000x3000	6	D	No	N	Y	N	N	200	Bar Type
95		No	5000x3000	6	D	No	N	N	Y	N	200	Bar Type
96		No	5000x3000	6	D	No	N	N	N	Y	200	Bar Type

Appendix B: Additional Analysis Results: Pushover Loading

B.1 Concrete compression strength comparison for the squat wall.

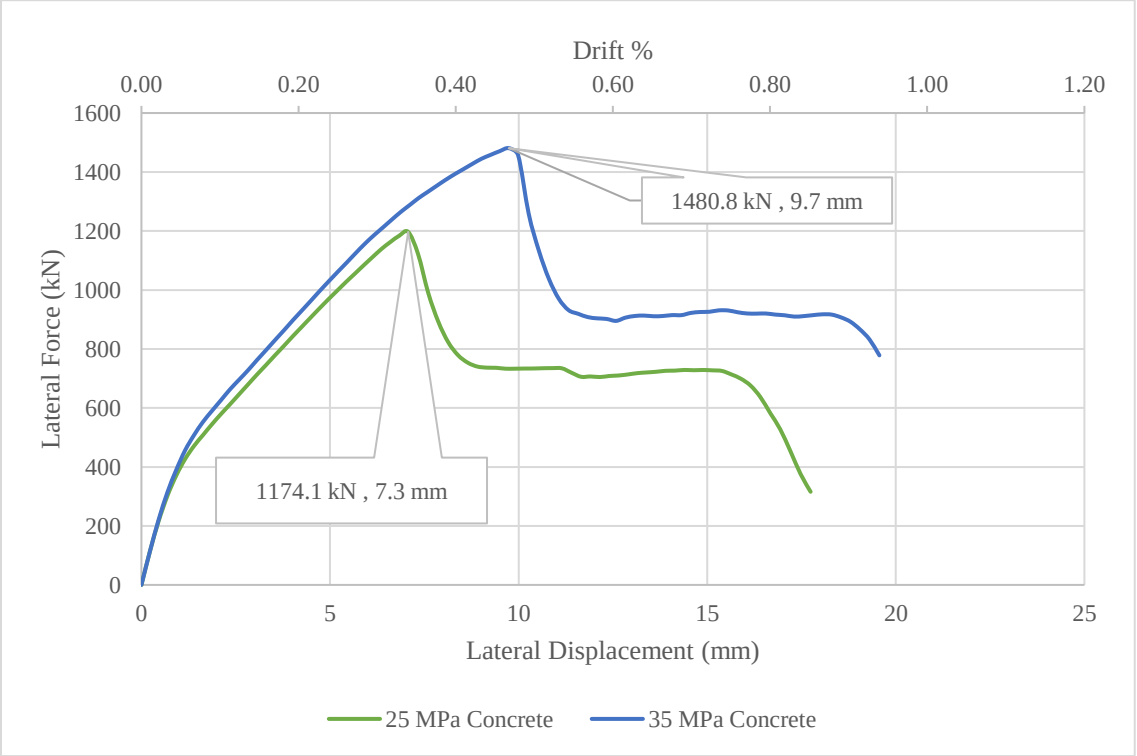

Figure B.1-1 Lateral performance of squat wall with 25 MPa vs. 35 MPa concrete strength

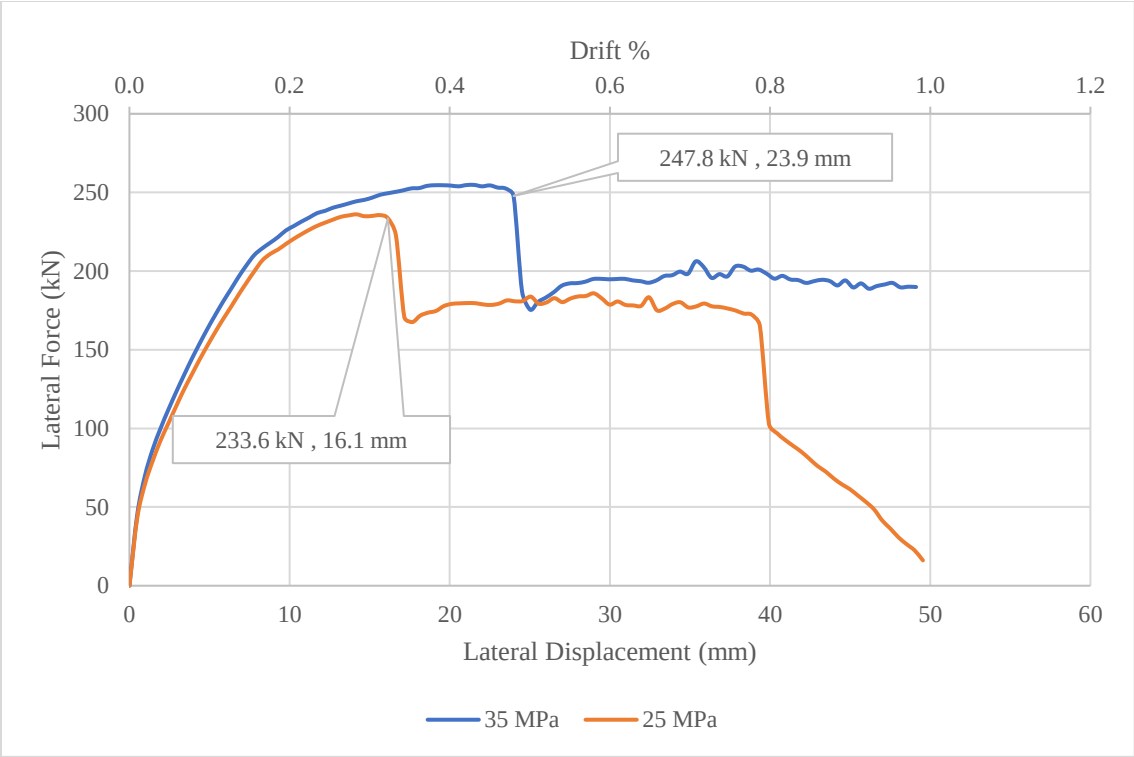

Figure B.1-2 Lateral performance of slender wall with 25 MPa vs. 35 MPa concrete strength

B.2 Comparison of assumed external light gauge steel contribution.

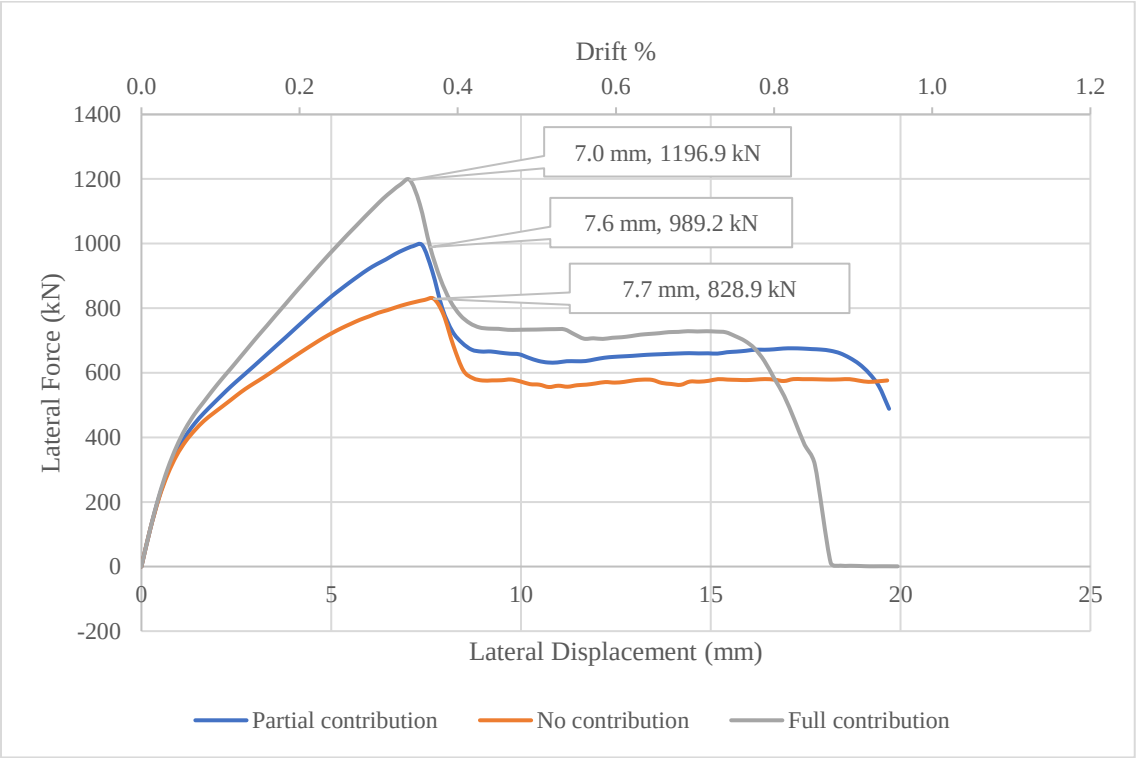

Figure B.2-1 Different contributions of the exterior light gauge steel to the squat wall

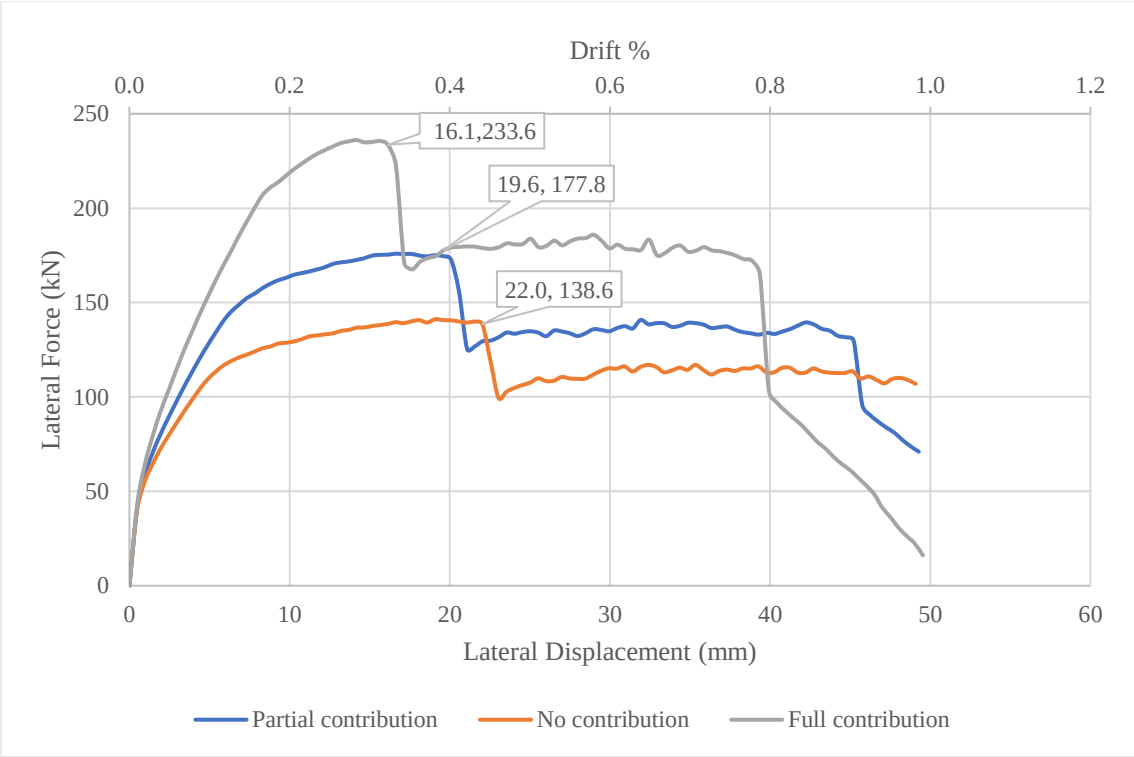

Figure B.2-2 Different contributions of the exterior light gauge steel to the slender wall

B.3 Comparison of the embedment length of the exterior light gauge steel.

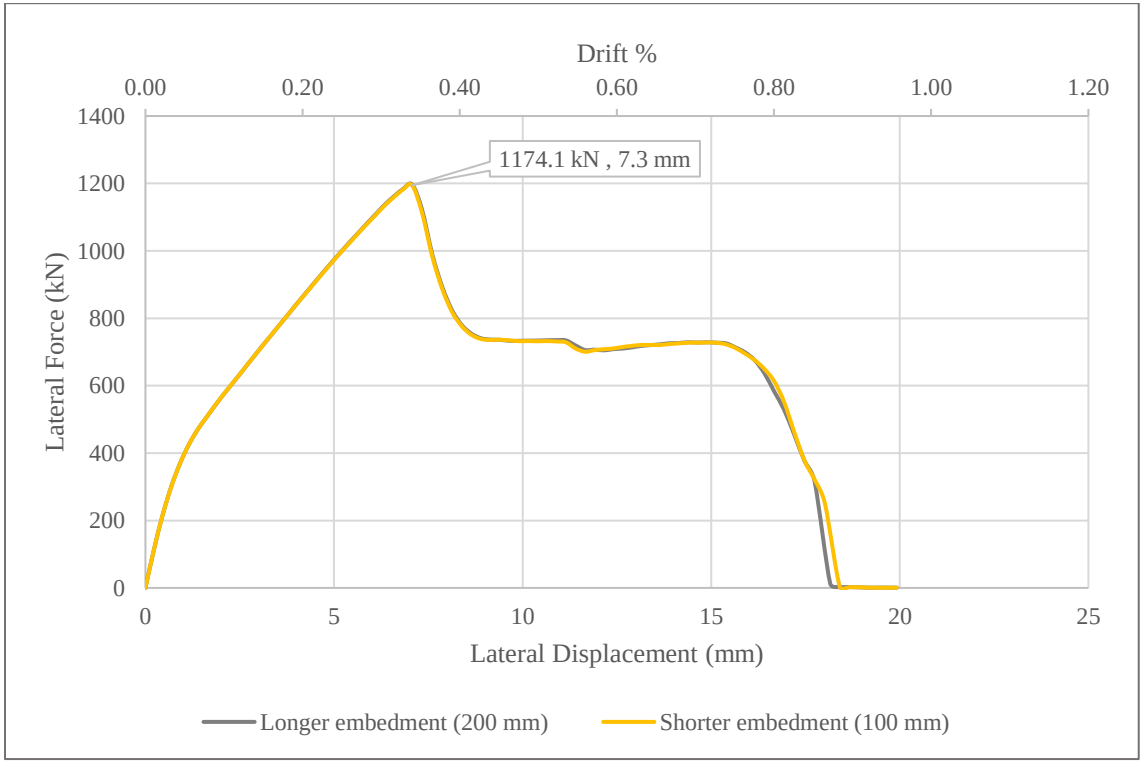

Figure B.3-1 Effect of embedment length of light gauge steel on squat wall lateral performance

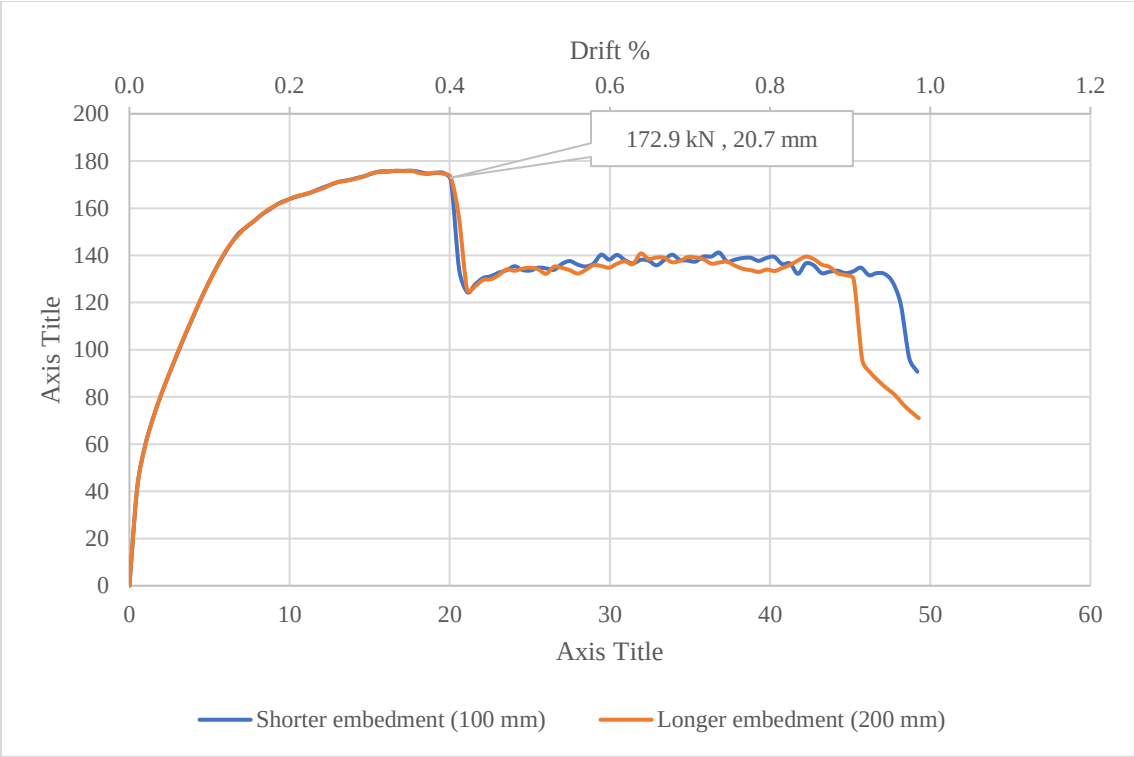

Figure B.3-2 Effect of the embedment length of the light gauge steel on slender wall lateral performance